CHALMERS
UNIVERSITY OF TECHNOLOGY

Stability-Preserving Slip Control of Articulated Heavy Vehicles Using Adaptive Longitudinal Slip Limits Derived from Phase Portraits

Master's Thesis in Systems, Control and Mechatronics

MATHANESH VELLINGIRI RAMASAMY

DEPARTMENT OF MECHANICS AND MARITIME SCIENCES

CHALMERS UNIVERSITY OF TECHNOLOGY
Gothenburg, Sweden 2025
www.chalmers.se

Master's Thesis in Systems, Control and Mechatronics

Stability-Preserving Slip Control of Articulated Heavy Vehicles Using Adaptive Longitudinal Slip Limits Derived from Phase Portraits

Mathanesh Vellingiri Ramasamy

CHALMERS
UNIVERSITY OF TECHNOLOGY

Department of Mechanics and Maritime Sciences
Division of Vehicle Engineering and Autonomous Systems
Chalmers University of Technology
Gothenburg, Sweden 2025

Stability-Preserving Slip Control of Articulated Heavy Vehicles Using Adaptive Longitudinal Slip Limits Derived from Phase Portraits.
Master's Thesis in Systems, Control and Mechatronics.
MATHANESH VELLINGIRI RAMASAMY.

Supervisor: Umur Erdinc, Volvo Group Trucks Technology, Sweden
Examiner: Mats Jonasson, Mechanics and Maritime Sciences

Master's Thesis 2025
Department of Mechanics and Maritime Sciences
Chalmers University of Technology
SE-412 96 Gothenburg
Sweden
Telephone +46 31 772 1000

Cover: Illustration of a Volvo truck semi-trailer model during a turning maneuver.

Typeset in LaTeX
Department of Mechanics and Maritime Sciences
Göteborg, Sweden 2025

Stability-Preserving Slip Control of Articulated Heavy Vehicles Using Adaptive Longitudinal Slip Limits Derived from Phase Portraits.
Master's Thesis in Systems, Control and Mechatronics.
MATHANESH VELLINGIRI RAMASAMY.
Department of Mechanics and Maritime Sciences
Division of Vehicle Engineering and Autonomous Systems
Chalmers University of Technology

Abstract

Ensuring the lateral stability of articulated heavy vehicles (AHVs) is critical for road safety, as they are susceptible to dangerous instability modes like jackknifing and trailer swing. Conventional stability control systems often rely on fixed slip thresholds, which may utilize higher slip limits than the proven safe limits under certain conditions, such as dynamic maneuvers involving high lateral accelerations. This thesis proposes an adaptive framework that determines safe longitudinal slip limits using phase portrait analysis.

A computationally efficient, non-linear single-track model of a tractor-semitrailer combination was developed and validated against the high-fidelity simulation environment, Volvo Transport Model (VTM). The core of the methodology involves reducing the complex dynamics into a series of 2D phase planes for both the tractor and trailer units. Stability for each point on the phase plane is systematically classified using Largest Lyapunov Exponent (LLE), allowing for the automated generation of Safe Operating Envelopes (SOEs).

This work establishes a robust methodology for generating state-dependent stability limits, laying the foundation for advanced control allocation strategies that can enhance the safety of AHVs by dynamically constraining actuator requests to remain within a safe region.

The practical utility of this framework was demonstrated by designing and implementing two distinct control strategies in VTM. The first, an offline controller, utilizes the pre-computed SOEs as a multi-dimensional lookup table to adaptively constrain driver slip requests. The second, an online controller, was developed to generate these stability limits dynamically within the simulation, showcasing a pathway toward fully adaptive in-vehicle systems. The performance of both controllers confirms that the SOE-based approach can effectively prevent instability while maximizing the vehicle's handling limit.

Keywords: articulated heavy vehicles, jack-knifing, trailer swing, adaptive longitudinal slip, phase portrait, safe operating envelope, control allocation.

Preface

This report presents the outcome of our master's thesis project carried out at the Department of Mechanics and Maritime Sciences at Chalmers University of Technology during the spring of 2025.

Acknowledgements

Embarking on this thesis has been a journey of discovery, collaboration, and growth. Ansh's expertise in vehicle dynamics and my background in control systems shaped our work from initial concept to final implementation, guided throughout by our supervisors' insights. This report presents the technical findings alongside reflections on teamwork, perseverance, and balancing theoretical depth with practical relevance. I hope the methods presented here provide a solid foundation for future work and that the account of collaboration offers value to those who follow. Ultimately, this thesis stands as a testament to the power of partnership and support, and I trust the reader will gain both concrete knowledge and an appreciation for the shared effort behind these pages.

I am profoundly grateful to Umur Erdinc from Volvo Group Trucks Technology for his invaluable guidance and real-world perspective. Your willingness to share deep technical insights and challenge me to bridge the gap between theory and practice enriched this research and kept me focused on delivering practical, impactful results.

My sincere thanks also go to Mats Jonasson at Chalmers, whose scholarly rigor and attention to detail have been instrumental in refining the methodology and strengthening the arguments. Your thoughtful critiques and encouragement pushed me to continually elevate the academic quality of this work.

I am equally grateful to Esteban Gelso and Maliheh Sadeghi Kati for ensuring a smooth on-boarding into the thesis internship and hosting us so effectively. By offering clear, constructive review suggestions, you helped me maintain momentum and sharpen the quality of the results throughout the project.

I also extend my thanks to my team manager, Simon Schoutissen, for his steady support and trust. Your guidance, help in clearing roadblocks, and alignment of resources created the conditions I needed to do my best work.

Working alongside Ansh has been both a privilege and a pleasure. Your creative problem-solving, unwavering optimism, and collaborative spirit transformed challenges into opportunities. From countless brainstorming sessions to late-night debugging marathons, your partnership has been the cornerstone of this thesis. Together, we turned ideas into results and challenges into achievements.

I also wish to acknowledge my friends and colleagues, whose thoughtful feedback on early drafts, insightful questions during presentations, and moral support over coffee breaks made the journey far more enjoyable. Your camaraderie sustained us through the toughest moments.

Finally, heartfelt thanks to my family for their patience, understanding, and encouragement. Your belief in me provided the emotional foundation I needed to persevere through deadlines and long work days. I am also indebted to the technical and administrative staff whose behind-the-scenes efforts ensured seamless access to resources, from library services to IT support.

To everyone who contributed their time, expertise, and support: thank you for making this thesis possible.

Mathanesh Vellingiri Ramasamy
Gothenburg, August 2025

List of Acronyms

Below is the list of acronyms that have been used throughout this thesis listed in alphabetical order:

AD	Autonomous Driving
ADAS	Advanced Driver Assistance Systems
AHV	Articulated Heavy Vehicle
BEV	Battery Electric Vehicle
CoG	Centre of Gravity
DAE	Differential Algebraic Equation
ECU	Electronic Control Unit
E.P.	Equilibrium Point
ESC	Electronic Stability Control
FBD	Free Body Diagram
HIL	Hardware-in-the-Loop
ICR	Instantaneous Centre of Rotation
LLE	Largest Lyapunov Exponent
MF	Magic Formula
MIL	Model-in-the-Loop
ODE	Ordinary Differential Equation
RMS	Root Mean Square
RSC	Roll Stability Control
SOE	Safe Operating Envelope
SDG	Sustainable Development Goal
VTM	Volvo Transport Model

Nomenclature

Below is the nomenclature of vehicle parameters, states and inputs that have been used throughout this thesis.

Vehicle Parameters

m_i	Mass of Unit i	kg
$h_{CG,i}$	CoG height of Unit i	m
J_i	Yaw moment of inertia of Unit i	$\mathrm{kg\,m^2}$
l_1	Wheelbase of truck	m
$l_{CG,1}$	Distance between front axle and CoG of truck	m
$l_{CG,1r}$	Distance between rear axle and CoG of truck	m
$l_{CG,2}$	Distance between trailer axle and CoG of trailer	m
$l_{c,1}$	Distance between coupling point and CoG of truck	m
$l_{c,2}$	Distance between coupling point and CoG of trailer	m
$l_{1r,c}$	Distance between rear axle of truck coupling point	m
$l_{c,2r}$	Distance between trailer axle and coupling point	m
R	Radius of curvature at CoG of truck	m
g	Gravitational constant	$\mathrm{m/s^2}$
μ	Road friction coefficient	-

Vehicle States and Inputs

$v_{x,i}$	Longitudinal velocity of Unit i	m/s
$v_{y,i}$	Lateral velocity of Unit i	m/s
β_i	Sideslip angle at CoG of Unit i	°
$\omega_{z,i}$	Yaw rate of Unit i	°/s
θ	Articulation angle	°
δ	Steering angle	°
$a_{x,i}$	Longitudinal Acceleration at the CoG of Unit i	m/s^2
$a_{y,i}$	Lateral Acceleration at the CoG of Unit i	m/s^2
s_x	Longitudinal tire slip	-
s_y	Lateral tire slip angle	°
F_x	Longitudinal force	N
F_y	Lateral force	N
F_z	Normal Force	N

Subscripts

$1f$	Front axle of Unit 1
$1r$	Rear axle of Unit 1
$2r$	Rear axle of Unit 2
CF, i	Front Coupling for Unit i
CR, i	Rear Coupling for Unit i
v	Vehicle Coordinate
w	Wheel Coordinate
eq	Equilibrium

Superscripts

act	Actual Value
req	Driver Request
ref	Controller Generated Reference

Contents

List of Figures

List of Tables

1
Introduction

1.1 Background

Articulated heavy vehicles (AHVs) play a crucial role in modern logistics, being vital for meeting the demands of our society. While aviation, marine, and railway transport handle long-haul routes, they typically cannot manage the "first and last mile" of the supply chain, which relies almost exclusively on road vehicles. Consequently, ensuring that heavy vehicle transport is conducted with maximum safety is a paramount challenge.

Statistically, AHVs are involved in a disproportionate number of severe accidents. In 2018, 14% of all road fatalities in the European Union occurred in crashes involving an AHV, despite them representing a small fraction of the total vehicle fleet [1]. A critical concern in AHVs is lateral instability, which can manifest in dangerous failure modes such as jackknifing, trailer swing, or rollover. The inherent characteristics of articulated vehicles, such as a long wheelbase and high center of gravity, make them especially susceptible to these instabilities during high-speed maneuvers or on low-friction surfaces.

To mitigate these risks, the industry has developed safety systems such as Electronic Stability Control (ESC) and Roll Stability Control (RSC). These systems intervene by applying differential braking or limiting engine torque when instability is detected. While effective, they operate on fixed, pre-calibrated thresholds for parameters like longitudinal wheel slip or yaw rate. Such an approach is inherently conservative as it fails to adapt to the changes in loading, road friction, or vehicle speed. It can either trigger intrusive interventions in safe conditions or miss critical warnings in extreme scenarios. This highlights a critical gap: the need for a control framework based on adaptive, state-dependent stability limits or Safe Operating Envelopes (SOEs) [2].

1.2 Sustainable Development Goals

The research presented in this thesis aligns directly with several of the United Nations Sustainable Development Goals (SDGs):

- **SDG 3** (Good Health and Well-being): Specifically target 3.6, which aims to halve the number of global deaths and injuries from road traffic accidents. By

developing more intelligent and adaptive safety systems for AHVs, this work contributes to reducing the frequency and severity of accidents.

- **SDG 9** (Industry, Innovation and Infrastructure): By introducing advanced control strategies and phase-portrait analysis into heavy-vehicle safety systems, this research promotes innovation in industrial transport and supports the development of resilient infrastructure.
- **SDG 11** (Sustainable Cities and Communities): Safer, more efficient freight transport reduces traffic disruptions and environmental impact, contributing to the sustainability and livability of urban and suburban areas.

1.3 Motivation

Our motivation stems from the need for more responsive and reliable stability controls in heavy-duty transport. Accidents involving jackknifing or trailer fishtailing can cause severe injuries, cargo loss, and traffic disruptions. At the same time, overly cautious controllers that permanently limit tire slip can reduce vehicle efficiency, increase fuel consumption, and limit maneuverability. By adapting slip limits in real time based on the vehicle's current operating point, we aim to achieve both safety and performance, pushing the envelope of what AHV stability systems can deliver.

1.4 Objectives & Research Questions

The primary goal of this thesis is to develop and validate a state-dependent, adaptive slip-based control framework to improve the lateral stability of AHVs. Unlike traditional safety systems that rely on fixed slip or yaw-rate thresholds, our approach uses phase-portrait analysis to map the exact dynamic boundaries between stable and unstable operation.

To guide this development, we address three key research questions:

- **Visualization:** Can the AHV's complex, high-dimensional dynamics be effectively reduced and visualized through 3D and 2D phase portraits to reveal its lateral stability characteristics?
- **Boundary Identification:** How can we automatically and robustly extract SOE boundaries using quantitative metrics like eigenvalues and Lyapunov exponents, across varying vehicle parameters and road conditions?
- **Control Integration:** Can these phase portrait derived SOEs be incorporated into an 'offline' (pre-computed stability limits) or 'online' (adaptable to instantaneous operating conditions) [3] control system that prevents jackknifing and trailer swing in a high-fidelity simulation environment?

To answer these questions, we will:

- Generate three-dimensional and two-dimensional phase portraits of key state variables (side-slip angle, yaw rate and articulation angle).

- Compute local stability measures (stable equilibrium, saddle points) and global indicators (largest Lyapunov exponents) from trajectory data.
- Translate these measures into a real-time SOE in the side-slip angle vs yaw rate phase plane.
- Design and implement a real-time adaptive longitudinal slip-based controller that continuously monitors the vehicle's state and adjusts wheel-slip commands to keep the AHV within its SOE.
- Evaluate performance through high-fidelity simulations, comparing against baseline fixed-limit controllers.

The purpose of this work is to show that phase portrait analysis not only sharpens our understanding of an AHV's stability limits beyond traditional methods, but also turns those insights into a working, real-time adaptive slip control system. By integrating the theory-based dynamic analysis with hands-on controller design, we aim to bridge the gap between academic research and industry needs, delivering both a proof-of-concept simulation and clear steps toward real-world implementation.

1.5 Instability Modes

When discussing the yaw stability of articulated vehicles, there are a few characteristic instability modes to consider:

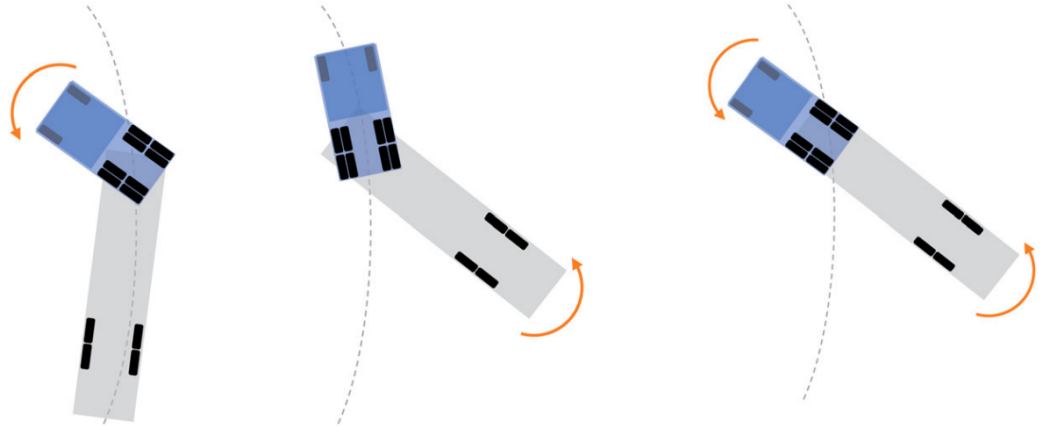

Figure 1.1: Illustrations of different yaw instabilities for a tractor (blue) and semi-trailer (grey). (a) Jackknifing. (b) Trailer swing and (c) Combination spin-out [2].

1.5.1 Jackknifing

Jackknifing is a loss of directional stability in the towing unit (the truck/tractor) that occurs while the trailing unit maintains grip as shown in Figure 1.1 (a). This often occurs when the tractor skids sideways as a result of heavy braking or acceleration

inturn, causing the articulation angle to increase rapidly. In such a scenario, the rear tires of the tractor lose lateral traction, often leading to a crash.

1.5.2 Trailer Swing

In contrast to the previous case, the trailing unit loses directional stability while the tractor remains relatively controlled, leading to trailer swing as shown in Figure 1.1 (b). This typically either occurs under excessive braking of the trailer or under trailer-powered acceleration in turn. Unlike jackknifing, a mild trailer swing may self-correct to some extent if it happens during braking (as the vehicle slows, the trailer can regain grip) [2]. However, if the swing is severe or not controlled at the right time, it might lead to a catastrophic crash. One of the other reasons for trailer swing could be improper loading of the trailing unit, which results in trailer sway during high-speed maneuvers.

1.5.3 Combination Spin-Out

In addition to the above two instability modes, there is also a possibility where both the units (the tractor and the trailer) lose lateral stability, resulting in a combination spin-out as shown in Figure 1.1 (c). In this case, both units slide in an uncontrolled manner, while still having a lower articulation angle. This usually occurs under extreme conditions, such as heavy braking or acceleration on a very steep curve, where the saturation point for both the unit's tires is reached, causing the vehicle to deviate from its intended path. Since both units are sliding, the articulation angle does not increase rapidly like the previous instability modes. The vehicle combination behaves like a single unit in a four-wheel drift and it shows that the AHVs can lose stability when all the tires lose grip together.

1.6 Current Research

The lateral stability of heavy vehicles has been a topic of significant research, with a variety of analytical methods being employed to understand and control their complex dynamics. Foundational to many modern analyses is the phase portrait method, a powerful graphical tool for studying the behavior of nonlinear systems. For single-unit vehicles, the phase portrait is typically defined in the sideslip-yaw rate (ω_z vs β) and sideslip-sideslip derivative (β vs $\dot{\beta}$) phase planes. It has been extensively used to define stability regions, identify equilibrium points, and analyze the influence of various vehicle parameters on stability [4],[5],[6]. This approach provides clear visual insight into phenomena like bifurcations, which mark the transition from stable to unstable behavior.

However, the direct application of 2D phase portrait analysis to AHVs is challenging due to their high dimensionality. The state of an AHV cannot be adequately characterized by two variables; it is inherently high-dimensional, comprising the dynamics of each unit and the articulation angles between them. To address this, Sun et al. [7] have explored three-dimensional phase portraits that incorporate variables like

articulation angle θ into a $\beta - \omega_z - \theta$ space. Other work has focused on applying phase plane analysis directly to complex, non-explicit multi-body models, such as those created in commercial simulation software, to bridge the gap between simplified analytical models and high-fidelity simulations [8].

To move beyond qualitative visual analysis and enable automated classification of stability, a quantitative measure is required. The concept of Lyapunov exponents has been successfully applied as such an indicator. Sadri et al. [9] first demonstrated the use of the Largest Lyapunov Exponent (LLE) to define the stability region of a 2-DOF vehicle model, while Meng et al. [10] further analyzed the global characteristics of Lyapunov exponents across vehicle models of varying complexity, showing they can effectively reveal system dynamics quantitatively.

The goal of these advanced analysis techniques is to generate SOEs that can be used in real-time control systems to enhance safety. The use of phase portraits to define stability boundaries for control has been demonstrated in various contexts, from coordinating multiple actuators like torque vectoring and rear-wheel steering [11] to developing envelope controllers that prevent the vehicle states from entering unstable regions [4].

This thesis builds directly upon the work of Erdinç [12], whose research established the framework for using SOEs for the safe control allocation of modern, over-actuated AHVs. Erdinç's work focused on the critical challenge of ensuring vehicle stability while optimising for secondary objectives, such as minimising power loss in electrified powertrains. Erdinç et. al [2] proposed defining SOEs in the force domain, mapping the safe limits of longitudinal force (or friction utilization) for the tractor and trailer as a function of lateral acceleration. This approach was successfully validated with high-fidelity simulations and real-world vehicle tests, proving that SOEs can effectively prevent jackknifing and trailer swing. Erdinç et al. [13] also explored alternative envelopes in the tire slip domain, proposing a "slip polytope" to adaptively limit longitudinal slip based on lateral slip.

1.7 Limitations

To ensure the feasibility of the research within the project's scope, the following limitations and assumptions have been established:

- The analysis and controller design are specific to a tractor-semitrailer combination. Other multi-trailer combinations such as A-doubles or B-doubles are left for future work.
- This work focuses exclusively on addressing divergent yaw instabilities, namely, jackknifing of the tractor and trailer swing. Roll stability and dynamic (oscillatory) yaw instabilities, such as trailer sway, are considered outside the scope of this thesis.

- The proposed control framework assumes the availability of key vehicle states and parameters. It is presumed that information such as the road friction coefficient, articulation angle, lateral acceleration, and yaw rates is accessible, either through direct sensor measurements or via a state estimator.
- Real-world factors such as sensor noise, actuator delays, and state estimation errors are not fully modeled.
- The methodology is based on instantaneous control allocation. It does not incorporate predictive control techniques that forecast future states. The controller reacts to the current state of the vehicle to ensure that the vehicle remains within the safe operating envelope.
- The control allocation strategy is designed to maintain stability by modulating the slip request for one axle at a time. The framework does not perform simultaneous, coordinated control allocation across all three axles of the combination.

In the following chapters, we provide the theoretical foundations for phase-portrait analysis, describe our computational methods, and present simulation results demonstrating the benefits of adaptive slip-based control for articulated heavy vehicles.

2
Vehicle Modeling

This chapter details the mathematical vehicle model used for the subsequent stability analysis. The use of phase portraits to define SOEs is central to the methodology of this thesis. This process requires many simulations across a wide range of conditions. To make this analysis feasible, a simplified yet reliable model is essential. This chapter describes the formulation of a non-linear single-track model, discussing its implementation using an explicit solver, and concludes by validating its accuracy against Volvo's high-fidelity simulation environment - Volvo Transport Model (VTM) [14].

2.1 Vehicle Model

The foundation of the stability analysis presented in this thesis is a mathematical model designed to accurately capture the essential yaw-plane dynamics of a truck-semitrailer combination. For this purpose, a non-linear single-track model [15] that incorporates longitudinal load transfer was developed. This model was chosen because it offers a good compromise between computational simplicity and physical fidelity. It effectively models the primary lateral instability modes of interest (jackknifing and trailer swing) while remaining computationally efficient enough for the thousands of simulations required to generate comprehensive phase portraits.

2.1.1 Simplifications

- **Lumped Axle Assumption:** The axle group of the semi-trailer are represented as a single equivalent axle.
- **No Transients:** A primary assumption is that high-frequency transient dynamics are excluded. The model does not include suspension components (springs and dampers) or tire relaxation length, which describes the lag in lateral force generation. This simplification is justified because the research focuses on quasi-steady-state stability analysis, where the vehicle's response is slower than these transient effects.

A direct consequence of the non-transient assumption is that the model can be initialized at any point in its state space without producing non-physical transient lags. This feature is fundamental to the "grid-based" simulation approach used for generating phase portraits, where thousands of simulations must be started from different initial conditions to map the system's stability.

2.1.2 Equations of Motion

The model is described by a set of coupled non-linear differential equations representing force and moment equilibrium for both the tractor (Unit 1) and the semitrailer (Unit 2) as shown in Figure 2.1.

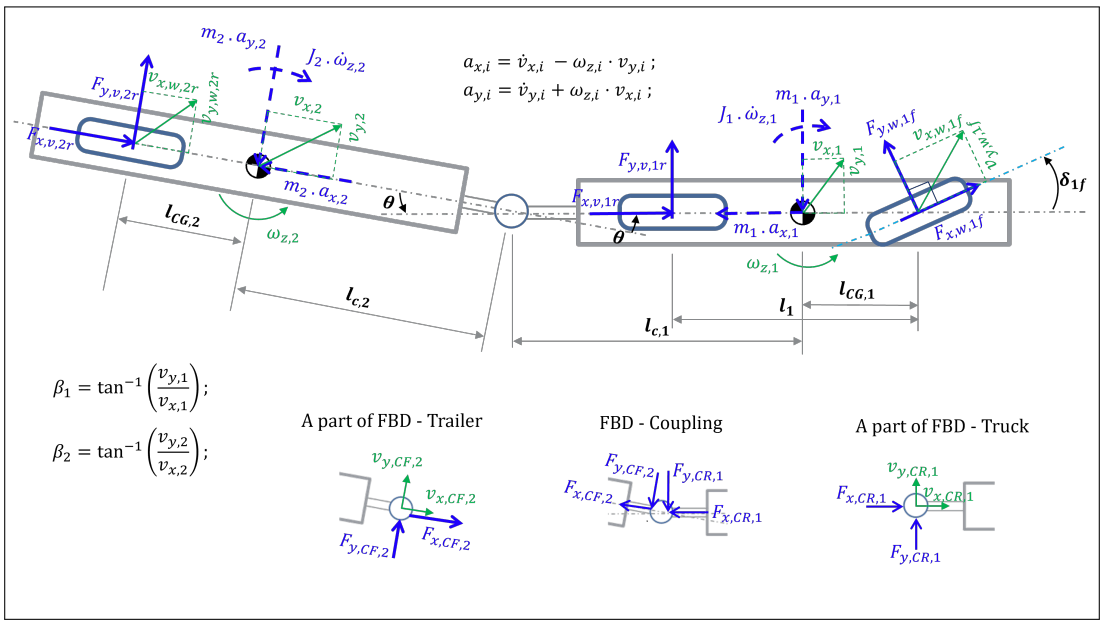

Figure 2.1: Free Body Diagram (FBD) of the truck-semitrailer (Based on [15]).

The nomenclature for all variables is detailed in the Nomenclature section.

The balance of forces along the longitudinal and lateral axes, as well as the equilibrium of yaw moments around the truck's (Unit 1) center of gravity (CoG), are expressed as follows:

$$m_1 \cdot a_{x,1} = F_{x,v,1f} + F_{x,v,1r} + F_{x,CR,1} \tag{2.1}$$

$$m_1 \cdot a_{y,1} = F_{y,v,1f} + F_{y,v,1r} + F_{y,CR,1} \tag{2.2}$$

$$J_1 \cdot \dot{\omega}_{z,1} = F_{y,v,1f} \cdot l_{CG,1} - F_{y,v,1r} \cdot (l_1 - l_{CG,1}) - F_{y,CR,1} \cdot l_{c,1} \tag{2.3}$$

The balance of forces along the longitudinal and lateral axes, as well as the equilibrium of yaw moments around the semitrailer's (Unit 2) CoG, are expressed as follows:

$$m_2 \cdot a_{x,2} = F_{x,v,2r} + F_{x,CF,2} \tag{2.4}$$

$$m_2 \cdot a_{y,2} = F_{y,v,1r} + F_{y,CF,2} \tag{2.5}$$

$$J_2 \cdot \dot{\omega}_{z,2} = -F_{y,v,1r} \cdot l_{CG,2} + F_{y,CF,2} \cdot l_{c,2} \tag{2.6}$$

where the components of the acceleration at the CoG of Unit 1 and 2 ($a_{x,1}$, $a_{y,1}$, $a_{x,2}$, and $a_{y,2}$) can be expressed as:

$$a_{x,1} = \dot{v}_{x,1} - \omega_{z,1} \cdot v_{y,1} \tag{2.7}$$

$$a_{y,1} = \dot{v}_{y,1} + \omega_{z,1} \cdot v_{x,1} \tag{2.8}$$

$$a_{x,2} = \dot{v}_{x,2} - \omega_{z,2} \cdot v_{y,2} \tag{2.9}$$

$$a_{y,2} = \dot{v}_{y,2} + \omega_{z,2} \cdot v_{x,2} \tag{2.10}$$

The components of the velocity at the rear coupling of Unit 1 ($v_{x,CR,1}$ and $v_{y,CR,1}$) are given by:

$$v_{x,CR,1} = v_{x,1} \tag{2.11}$$

$$v_{y,CR,1} = v_{y,1} - \omega_{z,1} \cdot l_{c,1} \tag{2.12}$$

The components of the velocity at the front coupling of Unit 2 ($v_{x,CF,2}$ and $v_{y,CF,2}$) are given by:

$$v_{x,CF,2} = v_{x,2} \tag{2.13}$$

$$v_{y,CF,2} = v_{y,2} + \omega_{z,2} \cdot l_{c,2} \tag{2.14}$$

The force and velocity balance for the coupling between the truck and the semi-trailer is determined by the following equations (given the articulation angle θ):

$$\dot{\theta} = \omega_{z,1} - \omega_{z,2} \tag{2.15}$$

$$F_{x,CF,2} = -\cos(\theta) \cdot F_{x,CR,1} + \sin(\theta) \cdot F_{y,CR,1} \tag{2.16}$$

$$F_{y,CF,2} = -\sin(\theta) \cdot F_{x,CR,1} - \cos(\theta) \cdot F_{y,CR,1} \tag{2.17}$$

$$v_{x,CF,2} = \cos(\theta) \cdot v_{x,CR,1} - \sin(\theta) \cdot v_{y,CR,1} \tag{2.18}$$

$$v_{y,CF,2} = \sin(\theta) \cdot v_{x,CR,1} + \cos(\theta) \cdot v_{y,CR,1} \tag{2.19}$$

The following equations convert the forces from wheel coordinates w to vehicle frame coordinate v for the steered axle.

$$F_{x,v,1f} = \cos(\delta_{1f}) \cdot F_{x,w,1f} - \sin(\delta_{1f}) \cdot F_{y,w,1f} \tag{2.20}$$

$$F_{y,v,1f} = \sin(\delta_{1f}) \cdot F_{x,w,1f} + \cos(\delta_{1f}) \cdot F_{y,w,1f} \tag{2.21}$$

To calculate the lateral tire slip s_y at each of the 3 axles (tractor front axle 1f, tractor rear axle 1r, and semi-trailer axle 2r), it is necessary to calculate the x and y components of velocity in the wheel frame for each axle respectively ($v_{x,w,1f}$, $v_{y,w,1f}$, $v_{x,w,1r}$,

$v_{y,w,1r}, v_{x,w,2r}, v_{y,w,2r}$).

$$v_{x,w,1f} = \cos(\delta_{1f}) \cdot v_{x,1} + \sin(\delta_{1f}) \cdot \Big(v_{y,1} + (\omega_{z,1} \cdot l_{CG,1})\Big) \tag{2.22}$$

$$v_{y,w,1f} = -\sin(\delta_{1f}) \cdot v_{x,1} + \cos(\delta_{1f}) \cdot \Big(v_{y,1} + (\omega_{z,1} \cdot l_{CG,1})\Big) \tag{2.23}$$

$$s_{y,1f} = \tan^{-1}\left(\frac{v_{y,w,1f}}{v_{x,w,1f}}\right) \tag{2.24}$$

$$v_{x,w,1r} = v_{x,1} \tag{2.25}$$

$$v_{y,w,1r} = v_{y,1} - \Big(\omega_{z,1} \cdot (l_1 - l_{CG,1})\Big) \tag{2.26}$$

$$s_{y,1r} = \tan^{-1}\left(\frac{v_{y,w,1r}}{v_{x,w,1r}}\right) \tag{2.27}$$

$$v_{x,w,2r} = v_{x,2} \tag{2.28}$$

$$v_{y,w,2r} = v_{y,2} - (\omega_{z,2} \cdot l_{CG,2}) \tag{2.29}$$

$$s_{y,2r} = \tan^{-1}\left(\frac{v_{y,w,2r}}{v_{x,w,2r}}\right) \tag{2.30}$$

The model also accounts for longitudinal load transfer. This is modeled by considering the pitching moments induced. The vertical forces on the Unit 1 front axle $F_{z,1f}$, rear axle $F_{z,1r}$ and Unit 2 axle $F_{z,2r}$ are determined by the following equations where $h_{CG,1}$ and $h_{CG,2}$ are the CoG height of the two units respectively.

The force and moment equilibrium about the CoG of Unit 1 in the $x - z$ plane to compute the longitudinal load transfer are expressed as:

$$F_{z,1f} + F_{z,1r} + F_{z,CR,1} = m_1 \cdot g \tag{2.31}$$

$$(m_1 \cdot a_{x,1} \cdot h_{CG,1}) + (m_1 \cdot g \cdot l_{CG,1}) - (F_{z,1r} \cdot l_1) - \Big(F_{z,CR,1} \cdot (l_{CG,1} + l_{c,1})\Big) = 0 \tag{2.32}$$

The force and moment equilibrium about the CoG of Unit 2 in the $x - z$ plane to compute the longitudinal load transfer are expressed as:

$$F_{z,CF,2} + F_{z,2r} = m_2 \cdot g \tag{2.33}$$

$$\Big(F_{z,CF,2} \cdot (l_{c,2} + l_{CG,2})\Big) + (m_2 \cdot h_{CG,2} \cdot a_{x,2}) - (m_2 \cdot g \cdot l_{CG,2}) = 0 \tag{2.34}$$

The force equilibrium across Unit 1 and Unit 2 in the $x - z$ plane leads to:

$$F_{z,CR,1} = F_{z,CF,2} \tag{2.35}$$

2.1.3 Tire Model

The tire model incorporated is the industry standard Pacejka Magic Formula 6.2 [16] to accurately calculate longitudinal and lateral tire forces based on longitudinal slip s_x, slip angle s_y, and vertical tire load F_z. The parameters for the Magic Formula (MF) were sourced directly from VTM simulation environment to ensure the tire behavior aligns with the reference model.

As stated in Section 2.1.1, tire relaxation effects were intentionally excluded from the tire model. This decision is fundamental to the phase portrait methodology, which requires initializing simulations from a wide array of states across a grid without introducing transient behavior. Including relaxation effects would introduce initialization-dependent transients, which would violate the quasi-steady-state analysis.

The equations for the tire model are referenced from [16].

Given the single-track nature of our model and the exclusion of roll dynamics (and thus camber angle), the tire model for each axle can be visualized as:

$$\begin{bmatrix} F_{x,w,1f} \\ F_{y,w,1f} \end{bmatrix} = 2 \cdot \text{MF}\left(s_{x,1f},\, s_{y,1f},\, \frac{F_{z,1f}}{2},\, v_{x,1}\right) \tag{2.36}$$

$$\begin{bmatrix} F_{x,v,1r} \\ F_{y,v,1r} \end{bmatrix} = 2 \cdot \text{MF}\left(s_{x,1r},\, s_{y,1r},\, \frac{F_{z,1r}}{2},\, v_{x,1}\right) \tag{2.37}$$

$$\begin{bmatrix} F_{x,v,2r} \\ F_{y,v,2r} \end{bmatrix} = 6 \cdot \text{MF}\left(s_{x,2r},\, s_{y,2r},\, \frac{F_{z,2r}}{6},\, v_{x,2}\right) \tag{2.38}$$

Assuming uniform load sharing, the normal load on each axle is distributed equally among the tires mounted on that axle. Accordingly, in (2.38), the multiplicative factor 6 equals the number of trailer tires (i.e., three axles with two tires per axle), so the per-tire normal load is $F_{z,2r}/6$. Likewise, in (2.36) and (2.37), the factor 2 equals the number of tractor tires considered, yielding per-tire normal loads $F_{z,1f}/2$ and $F_{z,1r}/2$, respectively. The total force for an axle is then obtained by multiplying the single-tire force by the number of tires on that axle.

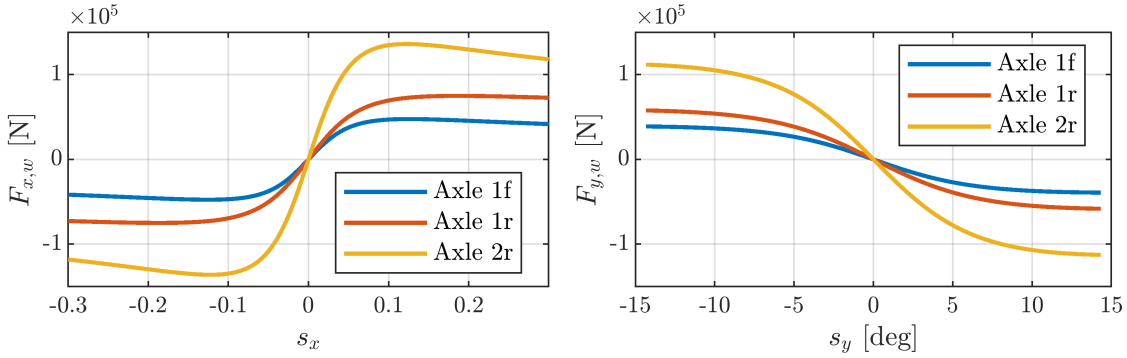

Figure 2.2: Longitudinal Force vs Longitudinal Slip (left) and Lateral Force vs Slip Angle (right).

Figure 2.2 displays the non-linear force generation characteristics of the tires for each axle of the truck-semitrailer model. The plots for longitudinal force $F_{x,w}$ versus slip s_x and lateral force $F_{y,w}$ versus slip angle s_y confirm that the tire's force capacity is highly dependent on its vertical load F_z and road friction μ. The different axles, each supporting a different static load and thus exhibit unique force curves.

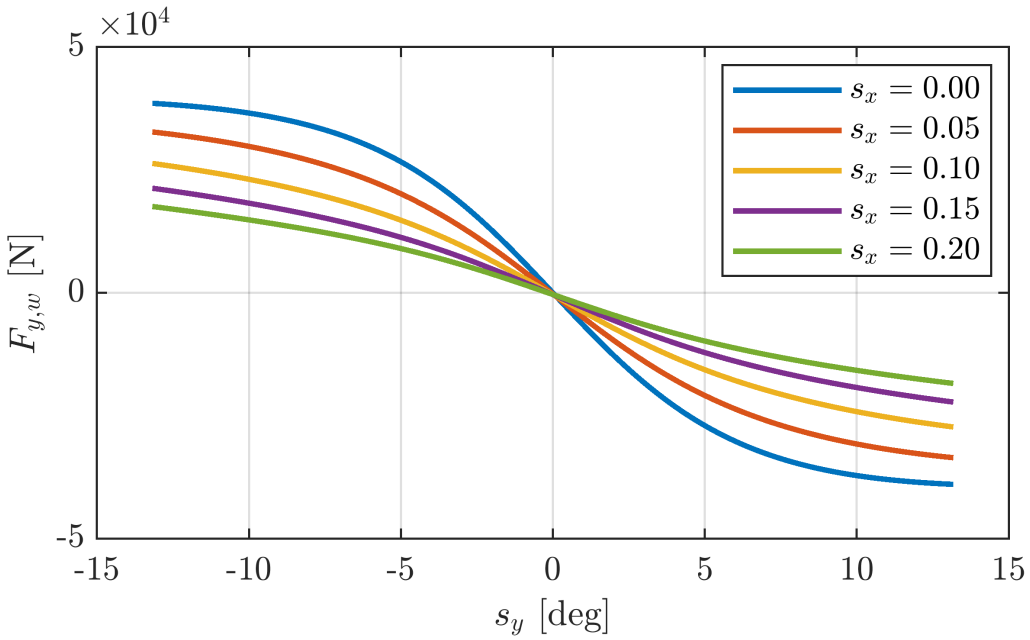

Figure 2.3: Lateral Force vs Combined Slip.

Figure 2.3 showcases the tire's lateral force response as a function of slip angle for various fixed longitudinal slip values. The reduction of lateral force with increasing longitudinal slip illustrates the combined-slip effect captured by the tire model.

2.2 Implementation using Explicit Solver

The set of equations presented (Equation (2.1)-(2.38)) defines the complete dynamics of the truck-semitrailer model. However, these equations form a system of Differential Algebraic Equations (DAEs), not a standard system of Ordinary Differential Equations (ODEs) in the form $\dot{x} = f(x, u)$. This is because the system includes not only differential equations for the state derivative but also algebraic constraint equations (Equation (2.18)-(2.19)) that link the states and internal forces without involving their derivatives.

DAEs can be solved directly by specialized implicit solvers, such as those found in MathWorks Simscape. However, this approach is computationally intensive. For generating phase portraits, which require tens of thousands of individual simulations, an implicit solver would be prohibitively slow. To achieve the necessary performance, the DAE system must be converted into an explicit ODE system where the state derivatives can be calculated directly from the current states and inputs.

2.2.1 Symbolic Derivation of Explicit Equations

To convert the DAE system to an ODE system, the algebraic constraints must be resolved to express the state derivatives explicitly [15]. This complex analytical task was automated using the MATLAB Symbolic Math Toolbox.

The process began by defining all vehicle parameters, states, state derivatives, inputs and internal forces as symbolic variables. The main challenge in this conversion lies in resolving the algebraic constraints, particularly the kinematic relationships at the coupling point defined in Equation (2.18) and (2.19). Substituting the value of $v_{x,CF,2}$, $v_{x,CR,1}$, $v_{y,CF,2}$, and $v_{y,CR,1}$ from Equation (2.11), (2.12), (2.13), and (2.14), the following equation is obtained.

$$v_{x,2} = \cos(\theta) \cdot \ v_{x,1} - \sin(\theta) \cdot \ \Big(v_{y,1} - (\omega_{z,1} \cdot \ l_{c,1})\Big) \tag{2.39}$$

$$v_{y,2} + (\omega_{z,2} \cdot \ l_{c,2}) = \sin(\theta) \cdot \ v_{x,1} + \cos(\theta) \cdot \ \Big(v_{y,1} - (\omega_{z,1} \cdot \ l_{c,1})\Big) \tag{2.40}$$

The velocity constraints in the Equation (2.39) and (2.40) were differentiated with respect to time.

$$\begin{aligned} \dot{v}_{x,2} = &-(\sin(\theta) \cdot \ \dot{\theta} \cdot \ v_{x,1}) + (\cos(\theta) \cdot \ \dot{v}_{x,1}) \\ &- \Big(\cos(\theta) \cdot \ \dot{\theta} \cdot \ (v_{y,1} - \omega_{z,1} \cdot \ l_{c,1})\Big) - \sin(\theta) \cdot \ \Big(\dot{v}_{y,1} - \dot{\omega}_{z,1} \cdot \ l_{c,1}\Big) \end{aligned} \tag{2.41}$$

$$\begin{aligned} \dot{v}_{y,2} + \dot{\omega}_{z,2} \cdot \ l_{c,2} = &(\cos(\theta) \cdot \ \dot{\theta} \cdot \ v_{x,1}) + (\sin(\theta) \cdot \ \dot{v}_{x,1}) \\ &+ \Big((-\sin(\theta) \cdot \ \dot{\theta}) \cdot \ (v_{y,1} - \omega_{z,1} \cdot \ l_{c,1})\Big) + \cos(\theta) \cdot \ \Big(\dot{v}_{y,1} - \dot{\omega}_{z,1} \cdot \ l_{c,1}\Big) \end{aligned} \tag{2.42}$$

This differentiation transformed the algebraic velocity constraints into new equations relating to the accelerations of the truck and semi-trailer, thereby making them compatible with the dynamic equations of motion.

With all equations defined, a complete system of 13 simultaneous equations was constructed, comprising the dynamic equations of motion, the differentiated kinematic constraints, and the longitudinal load transfer equations. The MATLAB `solve` function was then employed to symbolically solve this large system for 13 unknowns, which included the state derivatives ($v_{x,1}$, $v_{y,1}$, $\omega_{z,1}$, $v_{x,2}$, $v_{y,2}$, $\omega_{z,2}$, θ) and the internal unknown forces (coupling and vertical forces $F_{x,CR,1}$, $F_{x,CF,2}$, $F_{y,CR,1}$, $F_{y,CF,2}$, $F_{z,CR,1}$ and $F_{z,CF,2}$). This step analytically eliminated the algebraic dependencies and internal forces, yielding explicit expressions for each state derivative purely as a function of known states, inputs, and vehicle parameters.

The final step was to translate these large symbolic expressions into computationally efficient code using the `matlabFunction` command with its optimization feature enabled. This function automatically performs common sub-expression elimination, identifying and replacing repeated calculations with 592 temporary variables. The result was a highly optimized MATLAB function that computes the derivatives using just 76 final expressions.

2.3 Validation against VTM

A mathematical model, especially a simplified one, is only useful for analysis if its predictive capabilities are verified against a high-fidelity reference. This step is crucial to ensure that the simplified model, despite its inherent assumptions and lower complexity, captures the essential lateral and yaw dynamics of a real-world AHV. The goal is to confirm that the model accurately reproduces key vehicle states such as sideslip angle β_1, β_2, yaw rates $\omega_{z,1}$, $\omega_{z,2}$, and articulation angle θ under a range of driving conditions. A successful validation confirms that the model is a reliable tool for the computationally intensive task of generating the SOEs that form the core of this thesis.

To serve as the benchmark for validation, VTM was selected as the high-fidelity reference. VTM is a multi-body dynamics simulation environment developed and used extensively within the Volvo Group for vehicle development, research, and the design of active safety systems. Unlike the simplified single-track model, VTM incorporates a high level of detail, including suspension characteristics, detailed chassis, and advanced tire-road interaction models. Its validation against real-world test data makes it the reference for evaluating the performance of lower-order models.

2.3.1 Validation Methodology

To assess the model's accuracy, a validation methodology was employed based on a series of open-loop manoeuvres. The test suite was designed to excite the vehicle's lateral and yaw dynamics, allowing for a comparison across a range of behaviors. The core of the methodology involved a direct comparison against the VTM reference. A set of eight distinct open-loop steering scenarios was executed. These scenarios included:

- **Sine Steer:** With varying frequencies to evaluate the model's frequency response and its ability to capture oscillatory behavior.
- **Ramp Steer:** To assess the model's response to gradually increasing lateral acceleration and its quasi steady-state cornering characteristics.
- **Step Steer:** To test the model's transient response to sudden changes in driver input, which is critical for simulating evasive manoeuvres.

Figure 2.4 shows the different steering inputs selected for validating the model against the VTM model. Eight steering inputs, including step steer, ramp steer, and sine steer at varying frequencies and amplitudes, were selected to check the vehicle states versus time.

During the manoeuvres, the other vehicle inputs of throttle and brake were kept at a constant value of 0.

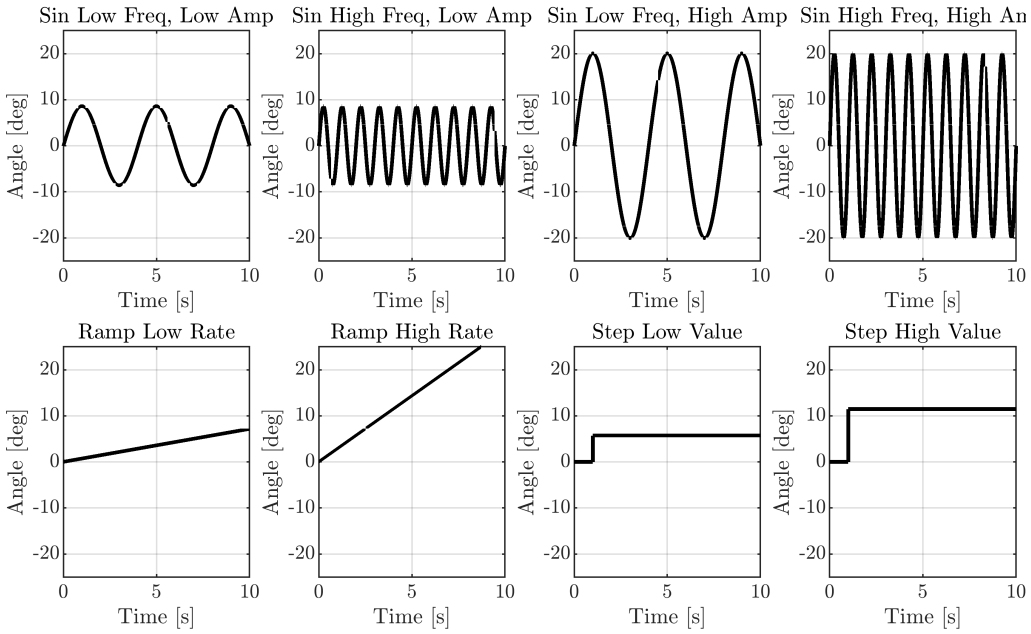

Figure 2.4: Eight steering inputs δ_{1f} selected for validation of the developed model vs VTM.

For each of the eight scenarios, the identical open-loop steering profile was supplied as a driver input to both the developed explicit single-track model and the high-fidelity VTM. All validation tests were conducted at a constant longitudinal velocity on a medium-friction surface ($\mu = 0.6$) at three longitudinal velocities $v_{x,1}$ at 5,10, and 15 m/s to provide a clear baseline for comparison.

The time-series data for the vehicle states such as sideslip angle β_1, β_2, yaw rates $\omega_{z,1}$, $\omega_{z,2}$, and articulation angle θ were recorded from both simulations. The resulting data sets were then plotted against each other to provide a direct visual and quantitative comparison of the models' performance along with the Root Mean Square (RMS) error and maximum error, forming the basis for the results presented in the next section.

2.3.2 Validation Results

Figure 2.5 presents the model's response to a step steer input at a velocity of 5 m/s. Visually, the model (blue line) demonstrates a strong correlation with the VTM data (red dashed line), accurately capturing the steady-state values for all states. A noticeable difference is the transient overshoot present in the VTM response, particularly for the truck yaw rate $\omega_{z,1}$, which is absent in the single-track model. This is an expected outcome, as the simplified model does not include the suspension dynamics or tire relaxation effects that contribute to this transient behavior in the high-fidelity VTM.

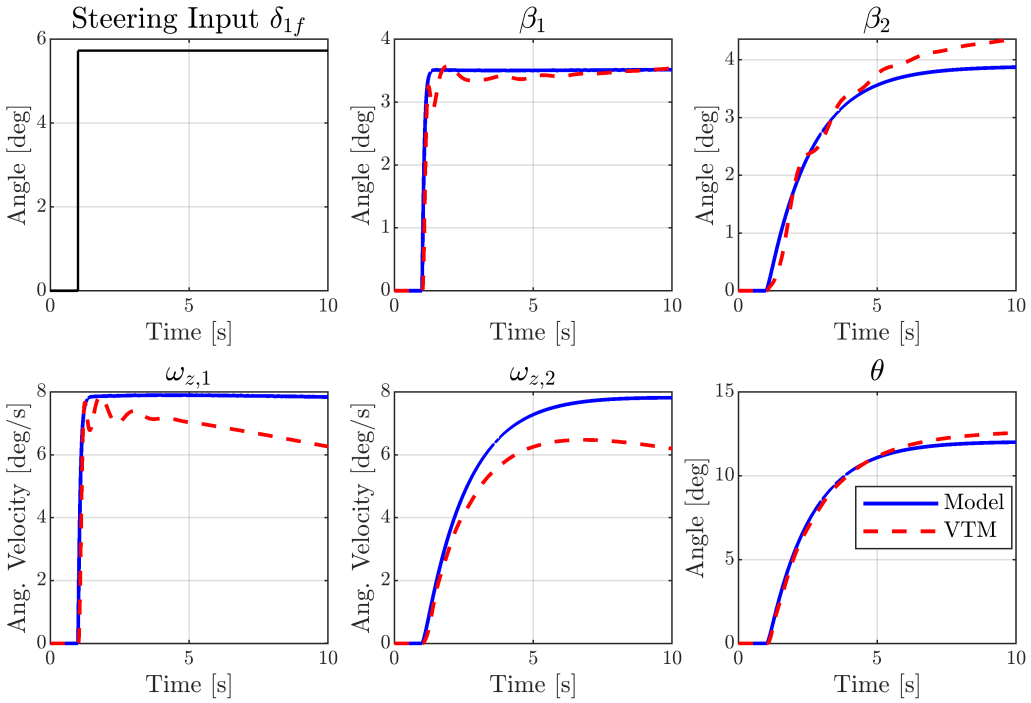

Figure 2.5: Comparing Vehicle States [Model (in blue) vs VTM (in red)] at $v_{x,1} = 5\ m/s$ for step steer manoeuvre.

The quantitative agreement is summarized in Table 2.1, which shows a low mean RMS error of just 1.26% across all states, confirming an excellent overall fit for this manoeuvre.

State	RMS Error	RMS Error [%]	Max Error	Max Error [%]
β_1	0.39°	0.72	3.57°	6.62
β_2	0.33°	0.58	6.18°	10.95
$\omega_{z,1}$	1.12 °/s	2.10	5.09 °/s	9.56
$\omega_{z,2}$	0.77 °/s	1.48	9.08 °/s	17.47
θ	0.79°	1.40	5.50°	9.77
Mean		**1.26**		**10.87**

Table 2.1: RMS Error and Max Error for different vehicle states corresponding to Figure 2.5 [$v_{x,1} = 5\ m/s$ for step steer manoeuvre].

The model's performance in other manoeuvres at the same low velocity is shown in Figure 2.6 (ramp steer) and Figure 2.7 (sine steer). The ramp steer comparison reveals nearly perfect tracking, which is expected as this slow, steady manoeuvre aligns well with the quasi-static nature of the single-track model. For the sine steer, the model accurately follows the VTM output in both phase and frequency, though it slightly underestimates the peak amplitudes, a common characteristic of simplified models.

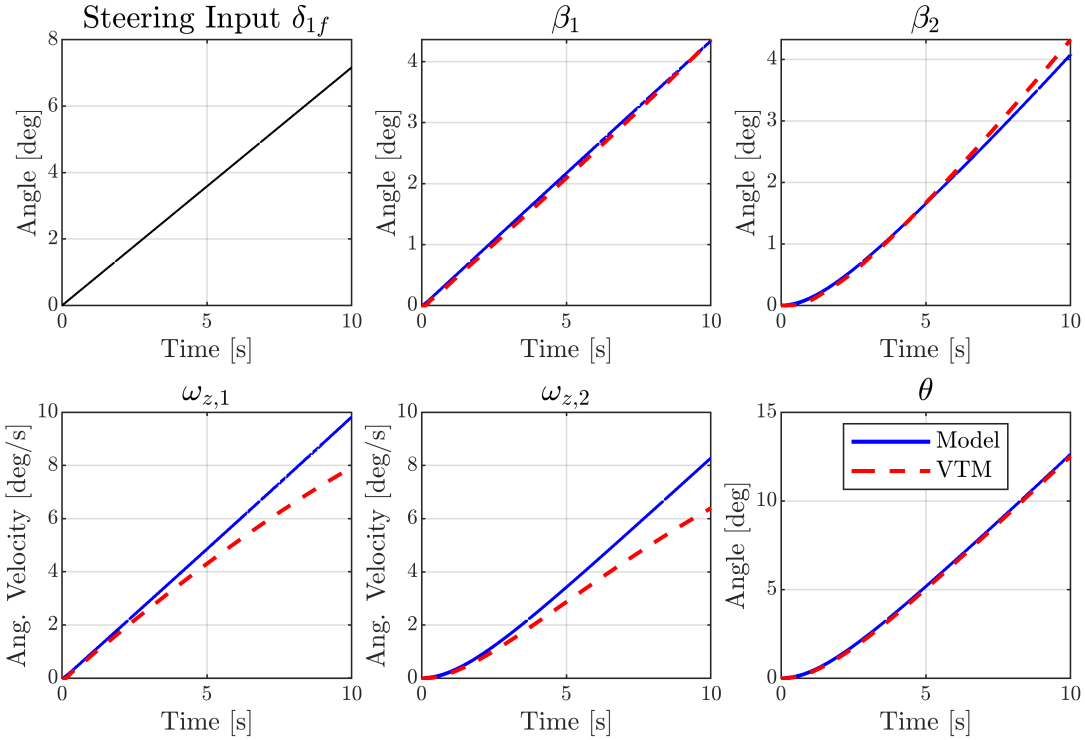

Figure 2.6: Comparing Vehicle States [Model (in blue) vs VTM (in red)] at $v_{x,1} = 5\ m/s$ for ramp steer manoeuvre.

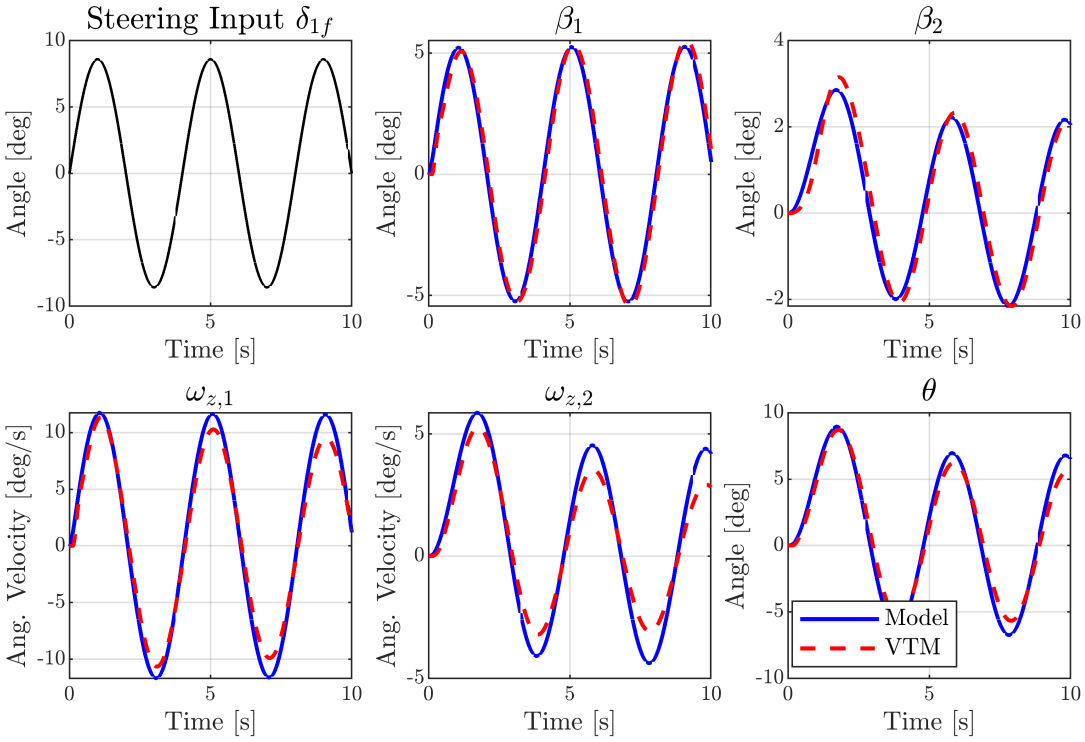

Figure 2.7: Comparing Vehicle States [Model (in blue) vs VTM (in red)] at $v_{x,1} = 5\ m/s$ for sine steer manoeuvre.

2.3.3 Validation Conclusion

An overview of the model's performance across the full suite of 24 validation scenarios is presented in Table 2.2. This table summarizes the mean RMS error across the five states (β_1, β_2, $\omega_{z,1}$, $\omega_{z,2}$, θ) and maximum error percentages for manoeuvres at varying velocities and steering input characteristics.

In most manoeuvres, the vehicle would exhibit a lateral instability mode at a similar point in the simulation. An outlier was observed in the "Sine Low Frequency, High Amplitude" manoeuvres at 10 m/s, where the vehicle jackknifes in VTM, but does not jackknife in the developed model, leading to a high error percentage for that specific scenario in Table 2.2.

Velocity ($v_{x,1}$)	**5 m/s**		**10 m/s**		**15 m/s**	
Steering Input (δ_{1f})	**RMS Error** [%]	**Max Error** [%]	**RMS Error** [%]	**Max Error** [%]	**RMS Error** [%]	**Max Error** [%]
Sine - Low Frequency, Low Amplitude	1.26	10.87	1.93	13.66	9.84	27.98
Sine - High Frequency, Low Amplitude	2.04	39.25	2.01	38.46	1.92	25.06
Sine - Low Frequency, High Amplitude	3.09	11.57	63.35[1]	123.90	13.07	29.01
Sine - High Frequency, High Amplitude	3.50	35.09	2.88	33.89	2.68	23.07
Ramp, Low Rate	0.85	12.35	1.39	17.79	36.11	108.04
Ramp, High Rate	7.86	30.01	13.64	22.06	17.63	49.88
Step, Low Value	1.38	23.02	1.35	18.49	11.02	35.59
Step, High Value	2.51	20.21	12.76	22.45	8.13	22.91
Mean	**2.81**	**22.80**	**12.41**	**36.34**	**12.55**	**40.19**

Table 2.2: Mean RMS Error % and Max Error % in vehicle states across varying velocities and steering inputs.

[1] Jackknifing observed in VTM but not in the developed model.

A clear and important trend that emerges from this data is that the model's accuracy is highest at lower velocities and for manoeuvres that induce lower lateral accelerations. For instance, the mean RMS error across all tests at 5 m/s is a low 2.81%. This error increases significantly to 12.41% at 10 m/s and 12.55% at 15 m/s. In these cases, the dynamic effects which were not captured by the single-track model, such as body roll and lateral load transfers, become dominant, leading to larger deviations from the VTM reference.

Another significant distinction between the models lies in their treatment of roll dynamics. The developed single-track model assumes no roll dynamics, effectively neglecting any difference in the roll motion between the two units. In contrast, VTM incorporates a detailed roll coupling between the two units, which contributes to the deviations observed in unit 2 states (β_2, $\omega_{z,2}$ and θ) during validation.

In conclusion, the validation process confirms that the developed explicit model is fit for its intended purpose. It demonstrates high accuracy in the low-to-moderate lateral acceleration range. Hence, the subsequent chapter will focus on analysis at low friction levels of ($\mu = 0.3$ to 0.6) where lateral instability modes of jackknifing and trailer swing occur at low values of lateral acceleration.

3

Phase Portrait Analysis

The complex dynamics of an AHV under varying road and loading conditions can be analytically visualized with the phase portrait approach. By plotting the key state variables against one another, these phase portraits visually reveal the hidden structure of the system's motion, its attractors, unstable manifolds, and safe regions. The main ingredients of the approach are introduced in the following sections: three-dimensional portraits, their two-dimensional reductions, quantitative stability measures, and the resulting SOEs.

3.1 Introduction to Phase Portraits

Phase portrait analysis is a powerful graphical method used to study the behavior of non-linear dynamical systems [4]. While time-domain plots can show a system's response from a single starting point, a phase portrait provides a comprehensive, global view of the system's stability and evolution from any initial condition within a given plane. The idea is to select the key state variables and plot them in a 2D or a 3D phase plane to visualize the system's behavior. This makes it an ideal tool for understanding complex, non-linear phenomena like vehicle instability, which are difficult to characterize.

In the context of lateral vehicle dynamics, phase portraits are typically generated for state pairs such as sideslip β vs yaw rate ω_z, sideslip β vs its time derivative $\dot{\beta}$, and, for articulated vehicles, even articulation angle θ vs its rate $\dot{\theta}$. In this work we adopt the β vs ω_z plane because it directly captures the coupling that governs yaw stability and avoids differentiating the noisy β. The sideslip angle measures the angle between the vehicle's heading and its actual direction of travel, indicating how much it is "sliding" sideways. The yaw rate is the angular speed at which the vehicle is rotating around its vertical axis. Together, these two states provide a snapshot of the vehicle's cornering behavior.

Figure 3.1 shows the phase portrait of a bicycle car model with linear tires subject to saturation, for a steering input $\delta_f = 5°$ and zero longitudinal force on each tire. This phase portrait is composed of several key elements:

- **Vector Field:** The faint grey arrows represent the vector field. At each point on the grid, the arrow indicates the direction and magnitude of the system's instantaneous rate of change (the state derivatives $[d\beta/dt,\, d\omega_z/dt]$). It shows

where the system will "flow" from that specific point.

- **Streamlines:** The solid blue lines are the streamlines. These are paths that trace the evolution of the vehicle's state over time, following the directions of the vector field, which serve as a visual aid to understand the system dynamics.

- **Equilibrium Points (E.P.):** These are points where the system's state is stationary (all derivatives are zero). They are critical for understanding stability. As shown in the legend, there are two primary types:
  1. **Stable Equilibrium Point:** This is a point where all nearby streamlines converge. It represents a desirable, stable operating condition, such as a balanced, steady-state turn. If the vehicle is slightly perturbed from this point, it will naturally return.
  2. **Unstable Equilibrium Point:** In this context, these are saddle points where streamlines are attracted along one direction but repelled along another. They represent critical thresholds or "tipping points" in the system's dynamics.

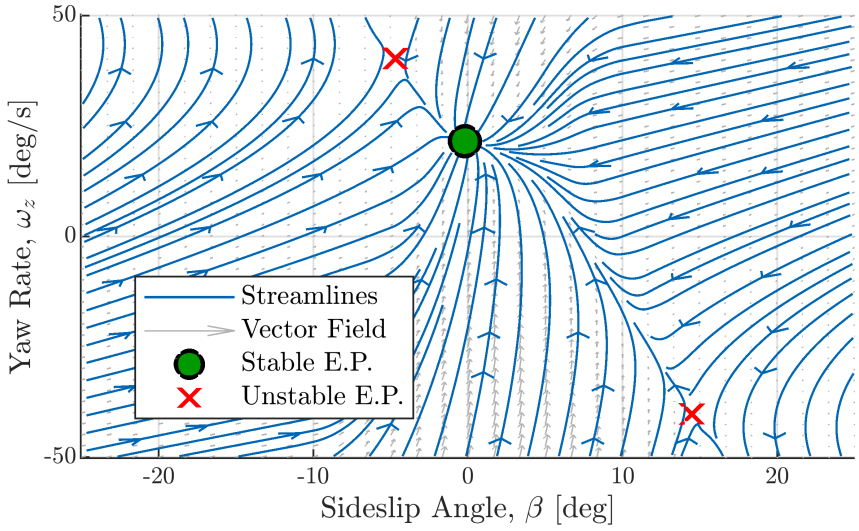

Figure 3.1: Phase portrait of a bicycle model of a car at $v_x = 10\ m/s$ and $\delta_{1f} = 5°$.

Interpreting the flow of the streamlines in Figure 3.1 provides us an insight into the vehicle's stability limits. The stable equilibrium point represents the target state for the manoeuvre. However, if a disturbance pushes the vehicle's state across the boundary defined by the unstable equilibrium points, the trajectory will diverge, leading to a loss of control, such as a spin. The region from which all trajectories converge to the stable point is known as the basin of attraction. The boundary of this basin forms the foundation for what this thesis will define as an SOE, a concept that will be systematically developed in the following sections for the more complex case of an AHV.

3.2 Challenges in Applying Phase Portrait to AHVs

While phase portraits are a powerful tool for visualizing two-dimensional systems, their direct application to complex, multi-body systems like AHVs presents significant challenges. Unlike a simple passenger car, which can often be described with three or fewer states (typically v_x, β, ω_z), the truck-semitrailer model developed in this thesis is defined by a five-dimensional state vector: $x = [v_{x,1}\ v_{y,1}\ \omega_{z,1}\ \omega_{z,2}\ \theta]^T$. This high dimensionality inhibits direct visualization, as the system's complete behavior cannot be captured in a single 2D phase plane.

This challenge is compounded by the system's sensitivity to numerous parameters that dynamically alter the vector field, including vehicle velocity $v_{x,1}$, road friction μ, steering angle δ_{1f}, and longitudinal axle slips s_x. A brute-force approach that simulates every combination of states and parameters would lead to a combinatorial explosion, rendering the problem computationally intractable. Furthermore, the existing body of literature on phase portrait analysis for vehicle dynamics is largely focused on simpler passenger cars, with limited literature for articulated configurations.

3.3 3D Phase Portraits

The stability investigation began by visualizing the system's dynamics in a three-dimensional phase space. This approach helps in understanding the interactions between the most critical lateral states of the truck and trailer. The selected phase space for this initial analysis is defined by the truck sideslip angle β_1, the truck yaw rate $\omega_{z,1}$, and the trailer yaw rate $\omega_{z,2}$.

For any given phase portrait, the system's inputs and key parameters are held constant to observe the evolution of the states from various initial conditions. For the following analysis, unless otherwise specified, the longitudinal axle slips s_x are set to zero, and the road friction coefficient μ is held at a constant value of 0.6.

The fundamental principle of this analysis is that a stable equilibrium point (E.P.) represents a steady-state condition where the vehicle is stable. Streamlines that converge to this point represent safe initial states. Conversely, initial states from which the streamlines diverge are considered unsafe, as they lead to unstable vehicle motion. This is particularly relevant for an articulated vehicle; when the yaw rates $\omega_{z,1}$ and $\omega_{z,2}$ reach a steady state, the articulation angle θ also converges to a constant value, indicating a stable turn as per Equation (2.15). The specific method for identifying and classifying these equilibrium points will be detailed in Section 3.5.1.

Figure 3.2 illustrates the system's behavior during straight-line driving. As expected, a single stable equilibrium is found at the origin (0, 0, 0), indicating that any small disturbance will result in the vehicle returning to a stable, straight-line path.

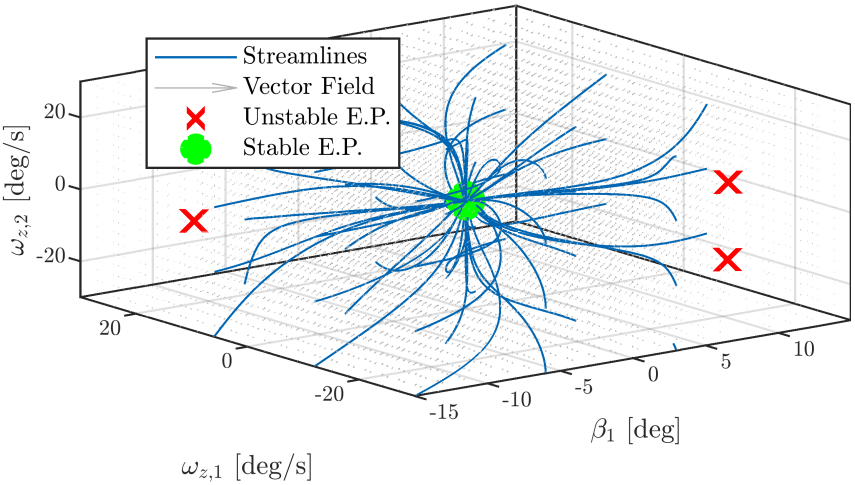

Figure 3.2: 3D Phase portrait (β_1, $\omega_{z,1}$, $\omega_{z,2}$) at vehicle state ($v_{x,1} = 10\ m/s$ and $\theta = 0°$) with input $\delta_{1f} = 0°$.

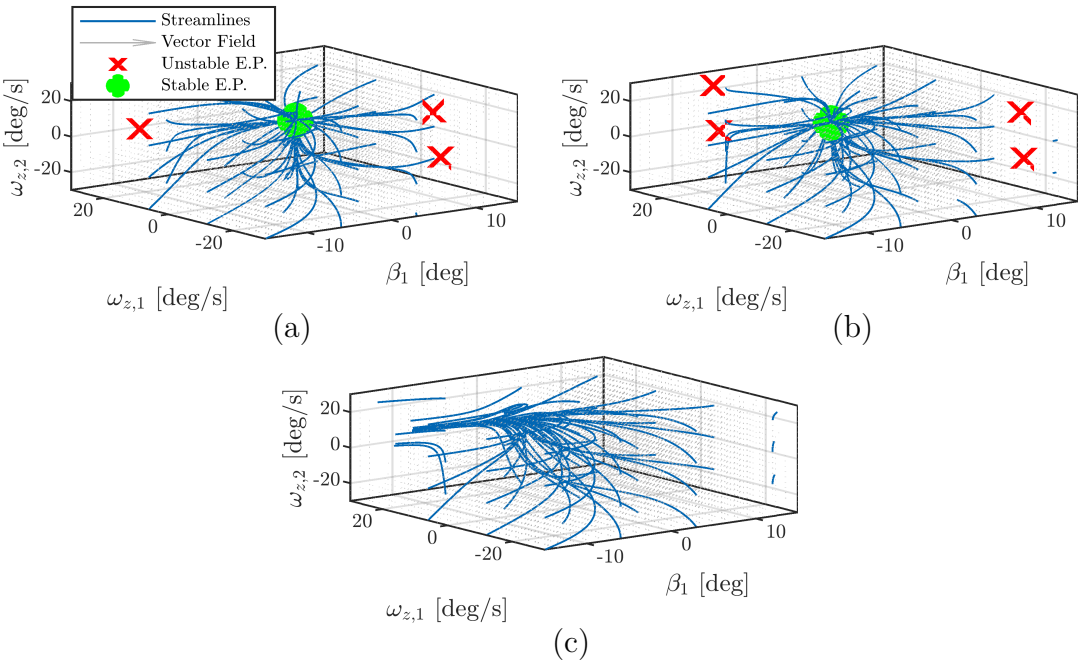

Figure 3.3: 3D Phase portrait (β_1, $\omega_{z,1}$, $\omega_{z,2}$) at vehicle state ($v_{x,1} = 10\ m/s$) (a) $\theta = 10°$, $\delta_{1f} = 0°$ (b) $\theta = 5°$, $\delta_{1f} = 3°$ (c) $\theta = 5°$, $\delta_{1f} = 8°$.

Figure 3.3 demonstrates how the system's stability landscape changes under different conditions.

- In Figure 3.3(a), the vehicle has a non-zero articulation angle but no steering input. While such a state does not correspond to a steady-state turn, it may still occur transiently in practice. For instance, when the driver exits a turn and straightens the steering wheel while the articulation angle has not yet

decayed to zero. This state leads to the presence of a stable equilibrium, which is not located at the origin unlike Figure 3.2.

- Figure 3.3(b) represents a mild turn with a steering angle of 3°. Here, a stable equilibrium exists, but it has shifted away from the origin, corresponding to the new steady-state turning values.
- In Figure 3.3(c), the steering angle is increased to an aggressive 8°. The streamlines show that no stable equilibrium is found, indicating that this manoeuvre is beyond the vehicle's stability limit under these conditions.

While these 3D portraits offer a holistic view, their primary drawback is the difficulty of visual interpretation. Identifying clear patterns and quantitatively defining stability boundaries directly from a 3D plot is challenging. To address this difficulty, the 3D space from Figure 3.3(b) was deconstructed into its three constituent 2D projections, as shown in Figure 3.4.

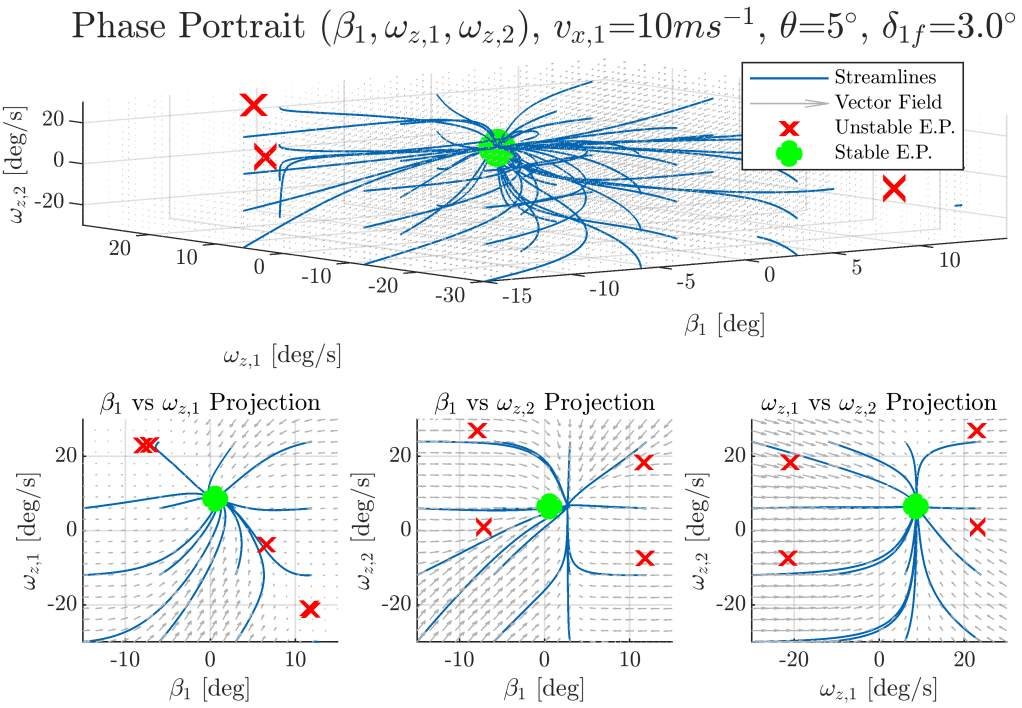

Figure 3.4: 3D Phase portrait (β_1, $\omega_{z,1}$, $\omega_{z,2}$) at vehicle state ($v_{x,1} = 10\ m/s$ and $\theta = 5°$) with input $\delta_{1f} = 3°$ with its three 2D projections.

While an interactive "slider" could be used to sweep through the third axis, in this report, it is represented by plotting several 2D "slices" at fixed values of the third state as shown in Figure 3.5.

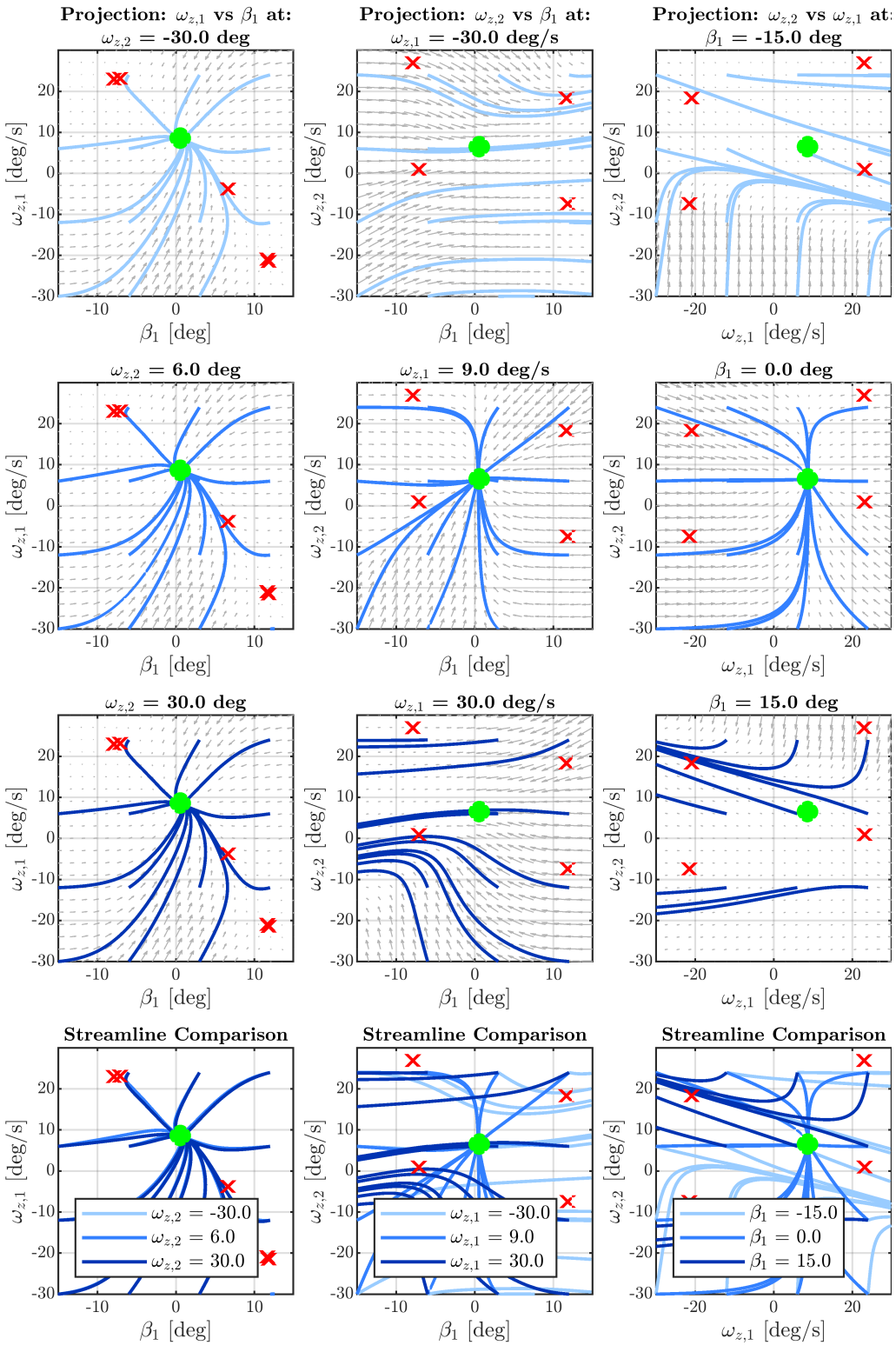

Figure 3.5: 2D projections of the 3D phase space at different fixed values of the third state.

Figure 3.5 provides a detailed comparative analysis of the 2D projections shown in Figure 3.4:

- **Column 1: Truck Stability Plane** ($\omega_{z,1}$ vs β_1)
  This column shows the projection onto the $\omega_{z,1}$ vs β_1 plane, with slices taken at different values of the trailer yaw rate ($\omega_{z,2} = -30, 0, 30\ deg/s$). The main observation is the robustness and consistency of the stability structure. The overall topology of the vector field is preserved as the streamlines, regardless of the trailer's yaw rate $\omega_{z,2}$, consistently guide the system towards the same stable equilibrium point. The streamline comparison in the bottom-left plot confirms this, showing that the paths are nearly identical. This indicates that the stability dynamics in the $\omega_{z,1}$ vs β_1 phase plane are dominant and relatively insensitive to the instantaneous state of the trailer's yaw rate $\omega_{z,2}$.

- **Columns 2 & 3: Coupled and Trailer-Centric Planes**
  In contrast, the other two projections exhibit extreme sensitivity to the slicing variable.

  1. The second column projects the dynamics onto the $\omega_{z,2}$ vs β_1 phase plane, sliced at different values of $\omega_{z,1}$. The vector field changes dramatically from one slice to the next. The streamlines show a completely different flow pattern when the truck's yaw rate is positive versus negative.
  2. Similarly, the third column, representing the $\omega_{z,2}$ vs $\omega_{z,1}$ projection sliced by β_1, also shows a highly variable structure.

The streamline comparison plots in the bottom-middle and bottom-right panels of Figure 3.5 make this instability clear. The overlaid streamlines from different slices do not align and instead show chaotic, intersecting paths. This makes it impossible to define a single, consistent SOE from these projections alone.

This visual analysis leads to the conclusion that justifies the methodology used in the remainder of this thesis: the stability of the system can be effectively and robustly analyzed by decoupling it into its constituent units. The truck's stability is best captured in the $\omega_{z,1}$ vs β_1 plane, which has been shown to be dominant and consistent. Consequently, instead of pursuing the visually complex and highly sensitive 3D analysis, this research proceeds with an automated analysis of the decoupled 2D phase planes for the truck and the trailer, independently.

3.4 Dimensionality Reduction via Decoupled Phase Plane Analysis

As established in the previous section, analyzing the vehicle's stability directly in a three-dimensional (or higher) phase space is complex and visually ambiguous. To make the problem tractable and enable a systematic, automated analysis, a dimensionality reduction strategy was developed. This approach does not simply ignore the influence of the other vehicle unit. Instead, it decouples the analysis into two distinct sub-problems while maintaining the physical link between the units through kinematic relationships.

The stability analysis is therefore split into two primary modes:

- **Truck stability** (jackknifing): Analyzed in the 2D phase plane $\omega_{z,1}$ vs β_1
- **Trailer stability** (trailer swing): Analyzed in the 2D phase plane $\omega_{z,2}$ vs β_2

For each case, the analysis assumes that the vehicle is in a zero-slip, steady-state kinematic turn. This allows the state of the "other" unit to be calculated based on the fixed parameters of the unit being analyzed, such as its velocity and the desired radius of curvature of the turn.

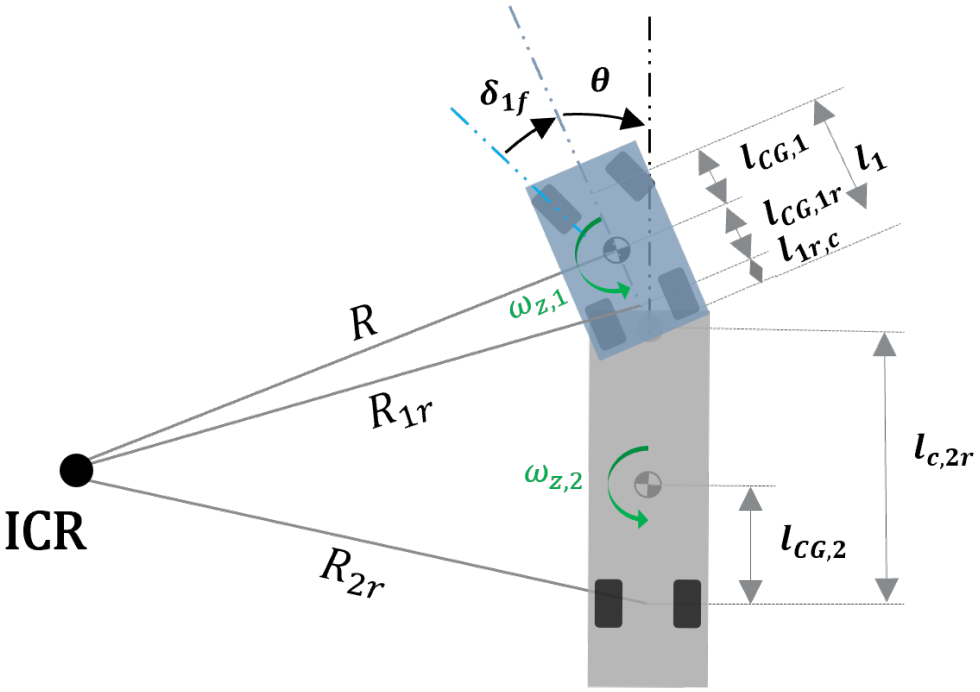

Figure 3.6: Kinematic relationship between the tractor and the trailer.

3.4.1 Kinematic Calculations for Unit 1 Stability Analysis

When generating a phase portrait for the tractor in the $\omega_{z,1}$ vs β_1 plane, it is essential to define the corresponding states of the trailer ($\omega_{z,2}$, θ) and the required steering input δ_{1f}. These are calculated by fixing the truck's velocity $v_{x,1}$ and the radius of curvature R about its CoG.

The kinematic calculations for Unit 1 can be summarized as:

$$[\delta_{1f},\ \omega_{z,2},\ \theta] = f(v_{x,1},\ R) \tag{3.1}$$

Assuming that the truck's rear axle $1r$, the coupling point c, and the trailer's rear axle $2r$ are all aligned tangentially to their respective circular paths around a common Instantaneous Centre of Rotation (ICR), their turning radii can be calculated geometrically as shown in Figure 3.6.

First, the turning radius of the truck's rear axle R_{1r} is found using the Pythagorean theorem:

$$R_{1r} = \sqrt{R^2 - l_{CG,1r}^2} \tag{3.2}$$

where R is the turning radius of the truck's CoG and $l_{CG,1r}$ is the longitudinal distance from the truck's CoG to its rear axle. Next, the turning radius of the trailer's rear axle R_{2r} is calculated based on the fixed geometry between the tractor's rear axle, the coupling point, and the trailer's rear axle:

$$R_{2r} = \sqrt{R_{1r}^2 + l_{1r,c}^2 - l_{c,2r}^2} \tag{3.3}$$

where $l_{1r,c}$ is the distance from the truck's rear axle to the coupling and $l_{c,2r}$ is the distance from the coupling to the trailer's rear axle. With these radii, and assuming that the yaw rates of both units are equal in a steady-state turn ($\omega_{z,1} = \omega_{z,2}$), the required steering angle δ_{1f} and the resulting articulation angle θ are given by:

$$\delta_{1f} = \tan^{-1}\left(\frac{l_1}{R_{1r}}\right) \tag{3.4}$$

$$\theta = \tan^{-1}\left(\frac{l_{c,2r}}{R_{2r}}\right) - \tan^{-1}\left(\frac{l_{1r,c}}{R_{1r}}\right) \tag{3.5}$$

These calculated values are then held constant while the $\omega_{z,1}$ vs β_1 phase portrait is generated.

3.4.2 Kinematic Calculations for Unit 2 Stability Analysis

The kinematic calculations for Unit 2 can be summarized as:

$$[\delta_{1f},\ \omega_{z,1},\ \theta] = f(v_{x,2},\ R) \tag{3.6}$$

Conversely, when analyzing trailer stability in the $\omega_{z,2}$ vs β_2 plane, the process is reversed. The trailer's velocity $v_{x,2}$ and its CoG turning radius R are fixed. The same geometric principles are used to solve for the truck's states.

The turning radius of the trailer's rear axle R_{2r} is calculated first:

$$R_{2r} = \sqrt{R^2 - l_{CG,2}^2} \tag{3.7}$$

where $l_{CG,2}$ is the distance from the trailer's CoG to its rear axle.

Then, the turning radius of the truck's rear axle R_{1r} is found using the same geometric constraint as before in Equation (3.3), but solved for R_{1r}:

$$R_{1r} = \sqrt{R_{2r}^2 - l_{1r,c}^2 + l_{c,2r}^2} \tag{3.8}$$

Finally, the required steering angle and the resulting articulation angle are calculated using the same formulas as in the Equations (3.4) and (3.5), which allows the $\omega_{z,2}$ vs β_2 phase portrait to be generated properly while accounting for the truck's influence.

This decoupled yet kinematically-linked approach provides the foundation for the automated stability analysis detailed in the following sections.

3.5 Stability Analysis and Classification

To move beyond subjective visual interpretation and enable a scalable analysis, a robust and automated methodology for classifying the stability of the system is required. This process involves two complementary techniques. First, the equilibrium points of the system are located and their local stability is classified using the Jacobian matrix. Second, a global stability assessment is performed across the entire phase plane grid using both finite-time Largest Lyapunov Exponents (LLE) and direct forward integration to determine the basin of attraction for stable equilibria.

3.5.1 Equilibrium Point Identification & Local Classification

The 'anchors' of any phase portrait are its equilibrium points, which represent the steady-state conditions where all state derivatives are zero. For the 2D decoupled systems, an equilibrium point $x_{eq} = [\beta_{eq} \quad \omega_{z,eq}]^T$ is a solution to the non-linear algebraic system:

$$F(x) = \begin{bmatrix} \dot{\beta}(x) \\ \dot{\omega}_z(x) \end{bmatrix} = 0 \tag{3.9}$$

These points are found using a numerical root-finding algorithm (`fsolve` in MATLAB), which iteratively searches for the state x_{eq} that minimizes the norm of the state derivative vector $F(x)$.

Once an equilibrium point is located, its local stability is determined by linearizing the system around that point using the Jacobian matrix, J. The Jacobian describes how a small perturbation away from the equilibrium point will evolve.

$$J = \left.\frac{\partial F}{\partial x}\right|_{x=x_{\text{eq}}} = \left[\begin{array}{cc} \frac{\partial \dot{\beta}}{\partial \beta} & \frac{\partial \dot{\beta}}{\partial \omega_z} \\ \frac{\partial \dot{\omega}_z}{\partial \beta} & \frac{\partial \dot{\omega}_z}{\partial \omega_z} \end{array} \right]_{x=x_{\text{eq}}} \tag{3.10}$$

The stability is then classified based on the eigenvalues λ of the Jacobian matrix:

- **Asymptotically Stable:** If all eigenvalues have negative real parts ($Re(\lambda) < 0$), any small perturbation will decay, and the system will return to the equilibrium. These points (stable nodes or foci) are the desired steady-state operating conditions.
- If at least one eigenvalue has a positive real part ($Re(\lambda) > 0$), perturbations will grow exponentially in at least one direction. These points (saddle points, unstable nodes, or foci) act as "dividers" in the phase space, separating different basins of attraction.

3.5.2 Imposition of Physical Tire Limits

While the system dynamics define the flow field, the physical limitations of the tires impose practical boundaries on efficient vehicle operation. Thus, the analysis incorporates the tire slip limits, which are defined by the peak sideslip angle $s_{y,peak}$ that a tire can sustain before its lateral force generation saturates and significantly decreases as suggested by Beal et al. [17]. $s_{y,peak}$ is obtained from the tire model for the static axle loading conditions at different friction levels.

Based on the vehicle's kinematic relationships, the vehicle side-slip angle β that corresponds to the front and rear tires reaching their peak slip angle can be calculated. These limit lines are a function of the yaw rate ω_z and are overlaid on the phase portrait to distinguish between safe and unsafe regions of operation.

The slip angles at peak lateral force are not a stability boundary. For example, exceeding the front-axle peak often causes understeer, but the vehicle can still be stable. These lines indicate when the tires are near saturation, and cornering stiffness is reduced. In this region, control authority and responsiveness decrease, while the energy consumption and thermal loads increase. The risk of instability under transients (e.g., brake or drive inputs and load transfer) also increases. Therefore, these lines are treated as performance limits (handling-quality markers) rather than strict stability limits.

The limit for the truck's front axle $1f$ is given by:

$$\pm\, \beta_{1f,\text{limit}} = \tan^{-1}\left(\tan(\delta_{1f} \pm s_{y,1f,\text{peak}}) - \frac{\omega_{z,1} \cdot l_{CG,1}}{v_{x,1}}\right) \tag{3.11}$$

And for the truck's rear axle $1r$:

$$\pm\, \beta_{1r,\text{limit}} = \tan^{-1}\left(\tan(\pm s_{y,1r,\text{peak}}) + \frac{\omega_{z,1} \cdot (l_1 - l_{CG,1})}{v_{x,1}}\right) \tag{3.12}$$

And for the trailer's rear axle $2r$:

$$\pm\, \beta_{2r,\text{limit}} = \tan^{-1}\left(\tan(\pm s_{y,2r,\text{peak}}) + \frac{\omega_{z,2} \cdot l_{CG,2}}{v_{x,2}}\right) \tag{3.13}$$

3.5.3 Stability Classification

To classify the stability of every point in the phase plane, not just the equilibria, two global methods are employed.

3.5.3.1 Classification via Largest Lyapunov Exponents (LLE)

The LLE provides a powerful quantitative measure of stability by measuring the average exponential rate of divergence or convergence of infinitesimally close trajectories [9]. The formal definition of the LLE (λ) is:

$$\lambda = \lim_{t\to\infty} \lim_{\|\Delta x_0\|\to 0} \frac{1}{t} \ln \frac{\|\Delta x(t)\|}{\|\Delta x_0\|} \tag{3.14}$$

where Δx_0 is the initial separation vector and $\Delta x(t)$ is the separation vector at time t. Here, the separation vector represents the difference between two trajectories that start from nearby initial states and are driven by the same inputs. If $x(t)$ and $x'(t)$ are the trajectories, then $\Delta x(t) = x'(t) - x(t)$ and $\Delta x_0 = x'(0) - x(0)$.

A finite-time LLE is evaluated at each point of the phase portrait grid. This is achieved by:

- Integrating an unperturbed trajectory from an initial state x_0.
- Integrating a second trajectory from a perturbed state $(x_0 + \Delta x_0)$, where Δx_0 is a very small initial separation.
- Calculating the LLE using the final separation $\Delta x(t)$ after a fixed integration time T_{lyap}.

$$\text{LLE} \approx \frac{1}{T_{lyap}} \ln \frac{\|\Delta x(T_{lyap})\|}{\|\Delta x_0\|} \tag{3.15}$$

In our case, Δx_0 was chosen to be 10^{-6} (smaller initial perturbation) so that we remain in the linear neighborhood of the trajectory. The integration time T_{lyap} was chosen to be 20 s. This duration represents a compromise between computational time and the need to observe meaningful changes in the trajectories. The sign of the LLE determines the stability of the initial point:

- **LLE $<$ 0:** Trajectories converge, indicating a stable point.
- **LLE $\geq$ 0:** Trajectories diverge, indicating an unstable point (instability).

This method allows for the entire phase space to be colored by its stability characteristic, clearly revealing the basin of attraction around stable equilibria.

3.5.3.2 Classification via Forward Integration

As a complementary and intuitive method, the stability of any given point can also be assessed by direct forward integration of the system's equations of motion. This process involves:

- Selecting an initial state $x_0 = [\beta_0 \;\; \omega_{z,0}]^T$ in the phase plane.
- Numerically solving the ODE $\dot{x} = F(x)$ forward in time, starting from x_0.
- Observing the final state $x(T)$ of the resulting trajectory after a sufficient simulation time T, which was chosen to be 5 s. This duration was chosen as a balance between ensuring sufficient time for trajectories originating near the boundary of the stability region to converge to the stable equilibrium point and reducing the computation time.

The stability is then determined by comparing the final state to the known stable equilibrium points $x_{eq,stable}$. If the distance $||x(T) - x_{eq,stable}||$ is below a small

convergence tolerance, the initial state x_0 is considered stable. In our case, the convergence tolerance was set to 5×10^{-3}. This value was determined by considering the grid density used to generate the phase portrait and accounting for any minor inaccuracies in the calculated position of the stable equilibrium points. This ensured that a trajectory was considered stable if its final state was within a suitably small proximity to the equilibrium.

This method confirms the LLE results and provides the actual path that the vehicle would follow on the phase plane, which is useful for visualizing the system's dynamic response.

3.6 Synthesis of SOE

3.6.1 Summary of the Analysis Pipeline

The methodologies detailed in the preceding sections: dimensionality reduction, equilibrium analysis, and global stability classification culminate in the generation of SOE for a given set of vehicle states, inputs, and parameters.

Figure 3.7 provides a comprehensive visual summary of this entire process, stepping through each stage of the analysis for both the tractor (Unit 1) and the trailer (Unit 2).

The analysis shown is for a specific scenario: a steady-state turn at a velocity $v_x = 10\ m/s$ and a radius of curvature $R = 100\ m$ with zero longitudinal slip on all axles ($s_{x,1f} = s_{x,1r} = s_{x,2r} = 0$). The kinematic calculator (Section 3.4.1 and 3.4.2) determines the required fixed states and inputs for this manoeuvre: a steering angle $\delta_{1f} = 2.1°$, a trailer yaw rate $\omega_{z,2} = 5.7\ deg/s$ for the Unit 1 analysis, and a corresponding tractor yaw rate $\omega_{z,1} = 5.7\ deg/s$ for the Unit 2 analysis, with a resulting articulation angle of $\theta = 5.7°$.

The step-by-step process illustrated in Figure 3.7 is as follows:

- **Phase Portrait (Row 1):** The analysis begins by plotting the raw phase portrait for each unit. The vector field and representative streamlines show the fundamental structure of the system's dynamics in the $\omega_{z,1}$ vs β_1 and $\omega_{z,2}$ vs β_2 planes, respectively.
- **Equilibrium Analysis (Row 2):** Using the Jacobian method as explained in Section 3.5.1, the equilibrium points are found and classified. For both units, a single Stable E.P. (green circle) is identified, representing the desired steady-state turning condition. Critically, unstable Saddle Points (Unstable E.P.) are also located (red crosses). These points are the gateways to instability, as trajectories passing near them are repelled away from the stable equilibrium point.

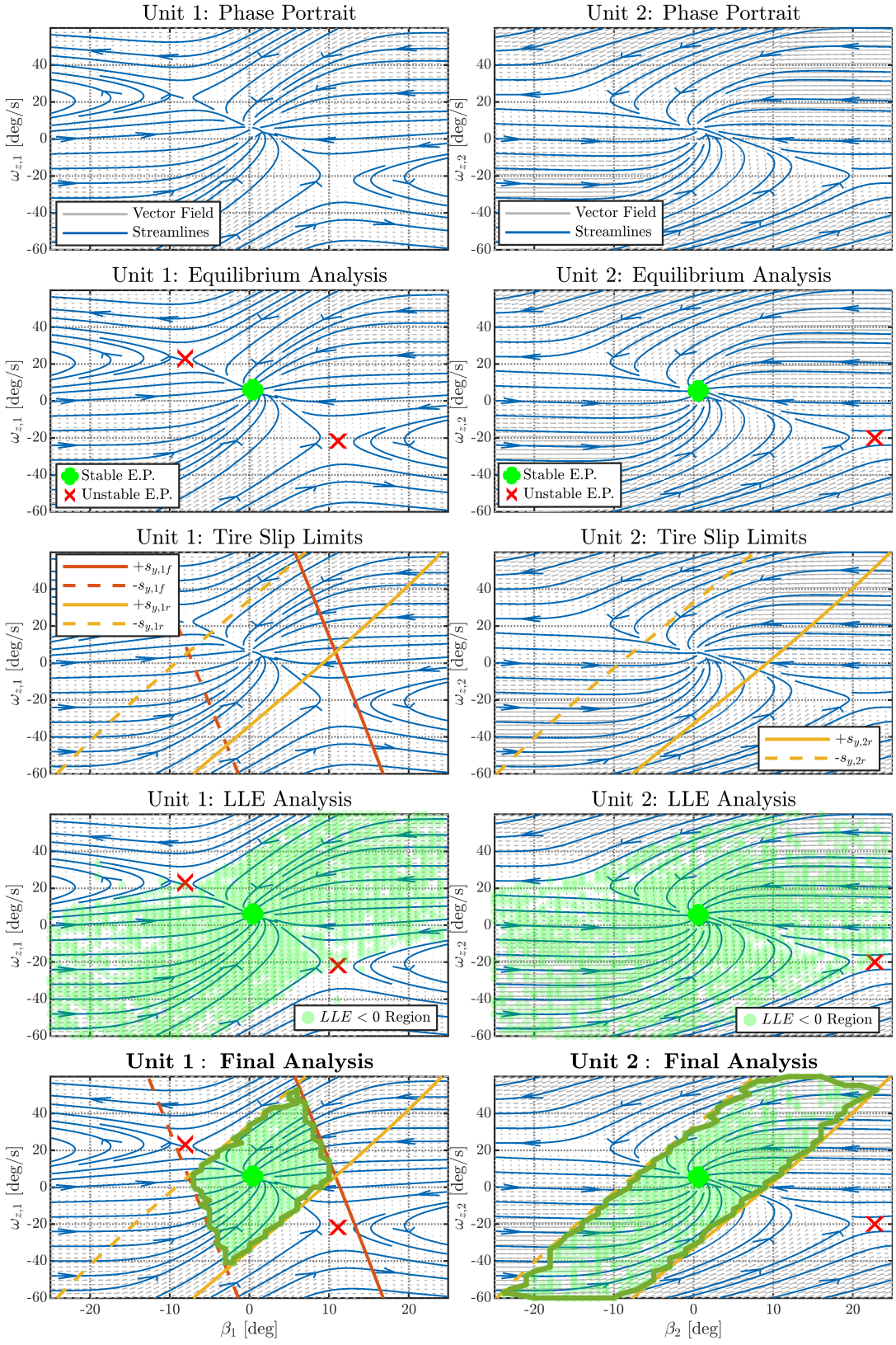

Figure 3.7: Step-by-step synthesis of the Safe Operating Envelope (SOE) for the truck (Unit 1, left column) and the trailer (Unit 2, right column). Each row illustrates a sequential stage of the analysis.

- **Tire Slip Limits (Row 3):** As explained in Section 3.5.2, the physical limits of the tires are overlaid on the phase plane. The solid and dashed lines represent the boundaries where the truck's front $s_{y,1f}$, truck's rear $s_{y,1r}$, and trailer rear $s_{y,2r}$ tire reach the slip angle at which they generate the maximum side force, as given by the tire model. Any state beyond these lines is considered unsafe.
- **LLE Analysis (Row 4):** The LLE is computed for every point on the grid. The resulting LLE < 0 region is shaded in green, representing the "basin of attraction." Any state starting within this green region is guaranteed to be stable and will eventually converge to the stable equilibrium point. This provides a global, quantitative measure of stability across the entire state space.
- **Final Analysis and SOE (Row 5):** The final step combines all previous analysis. The SOE, shown by the thick dark green line, is defined as the boundary of the stable LLE region that is also contained within the physical tire slip limits. This envelope represents the set of all states from which the vehicle is not only stable but also operating efficiently without saturating the tires. For a control system, any state outside this boundary is considered unsafe and requires intervention.

This synthesized SOE is the main result of the methodology, providing a precise, state-dependent representation of the vehicle's true stability limits.

3.6.2 Interpreting Stability Limits and Failure Modes

The true power of this methodology lies in its ability to predict how these SOEs change with varying inputs and to pinpoint the onset of specific failure modes. The following case studies demonstrate this predictive capability.

3.6.2.1 Case Study 1: Effect of Increasing Steering Severity

Figure 3.8 and Figure 3.9 illustrate the effect of tightening the radius of curvature from 35 m to 30 m while maintaining a constant velocity of 10 m/s.

The SOE borders' stair-stepped appearance in Figure 3.8 and Figure 3.9 is a direct result of the low grid resolution used in the stability analysis, which discretely samples the phase plane rather than plotting a continuous line. This is a trade-off made to manage computational time. At a radius of 35 m (Figure 3.8), the required steering angle δ_{1f} is 6.05°. For Unit 1, the stable and unstable equilibrium points have moved closer together, significantly shrinking the SOE. For Unit 2 (the trailer), a large and robust SOE still exists. This indicates the tractor is approaching its stability limit.

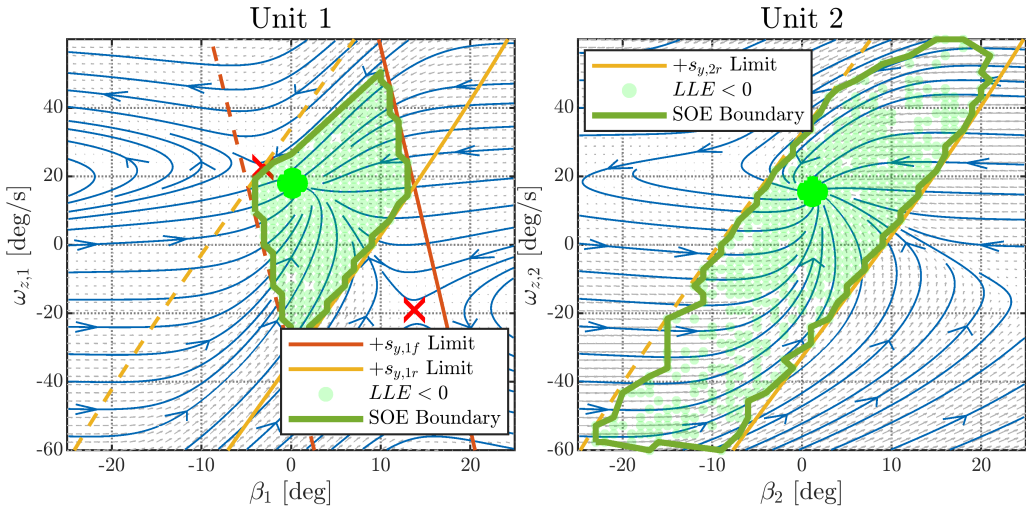

Figure 3.8: Phase Portrait at $v_{x,1} = 10\ m/s$ at $R = 35\ m$.

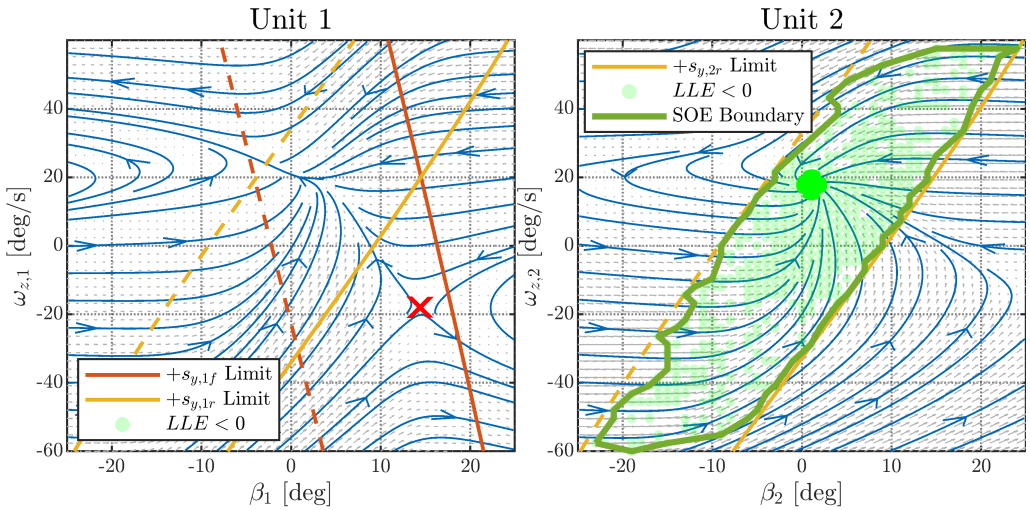

Figure 3.9: Phase Portrait at $v_{x,1} = 10\ m/s$ at $R = 30\ m$.

When the radius is tightened further to 30 m (Figure 3.9), the required steering angle δ_{1f} increases to 7.06°. The phase portrait for Unit 1 undergoes a critical change: the stable equilibrium point disappears entirely. This phenomenon, known as a bifurcation, leaves no region of stability for the truck. The absence of a stable point in the Unit 1 phase portrait suggests the onset of jackknifing behavior. Notably, the trailer (Unit 2) still possesses a stable equilibrium, confirming that the primary failure mode for this aggressive manoeuvre is jackknifing and not trailer swing. This analysis indicates that for this vehicle combination and friction level, the critical steering limit is between 6 and 7 degrees.

3.6.2.2 Case Study 2: Effect of Longitudinal Slip on the Trailer Axle

Figure 3.10 and Figure 3.11 demonstrate the impact of tractive force on the trailer's axle $2r$ during a constant radius turn ($R = 50\ m$) at 10 m/s.

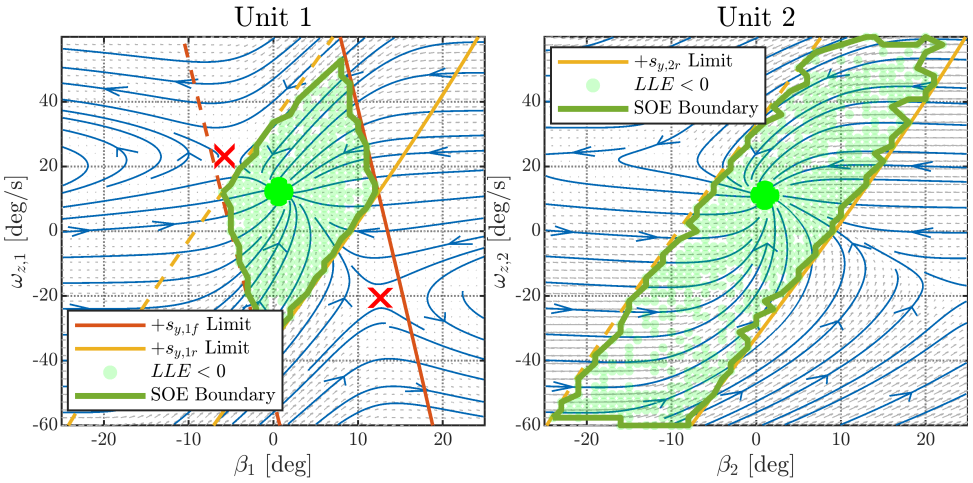

Figure 3.10: Phase Portrait at $v_{x,1} = 10\ m/s$ at $R = 50\ m$ with $s_{x,1r} = 0$.

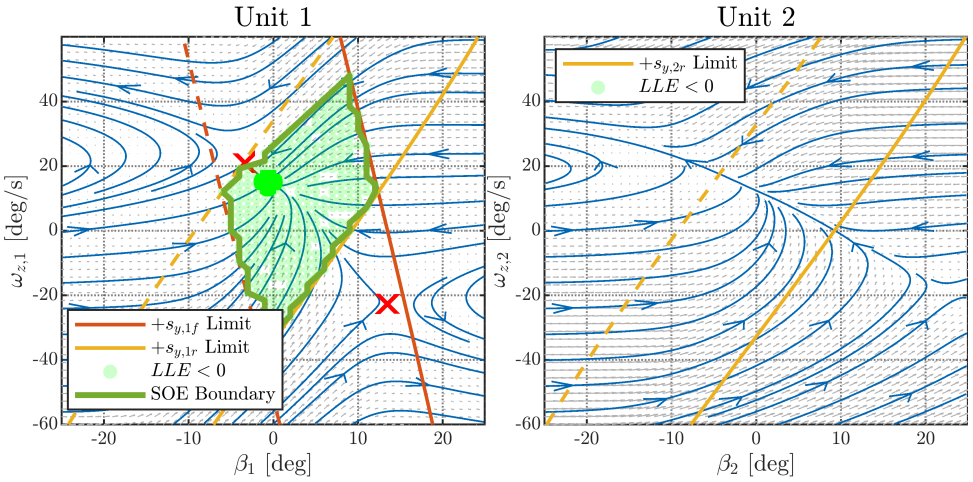

Figure 3.11: Phase Portrait at $v_{x,1} = 10\ m/s$ at $R = 50\ m$ with $s_{x,1r} = 0.1$.

In the baseline case with zero slip (Figure 3.10), both the tractor and trailer exhibit large, well-defined SOEs, indicating a stable manoeuvre.

However, when a tractive longitudinal slip $s_{x,1r}$ of 0.1 is applied to the trailer's axle (Figure 3.11), the stability of the system changes dramatically. Due to the combined longitudinal and lateral forces (the "friction circle" effect and the "combined slip" effect), the lateral grip capacity of the trailer's tires is significantly reduced. This is reflected in the phase portrait for Unit 2, where the stable equilibrium has vanished. The streamlines show a clear divergent pattern, indicating that the trailer can no longer maintain its path and will swing outwards uncontrollably. This is the onset of trailer swing. The truck (Unit 1), which is not directly affected by this slip, retains its stability. This case study highlights the importance of considering the multi-dimensional nature of tire forces and demonstrates how the SOE analysis can predict instabilities caused by combined acceleration and cornering.

While the SOE in the presented examples appears to fill the region bounded by the $s_{y,peak}$ lines, it can be smaller under certain conditions (e.g., at high longitudinal slip). This implies that a vehicle may become unstable before the tires reach their maximum lateral force capacity. Therefore, a dynamic analysis is necessary to determine the actual stability limits; relying solely on static tire slip limits is insufficient.

3.7 Safe Operating Envelopes

This section presents a parametric sensitivity analysis, illustrating the dynamic nature of the SOEs by systematically varying key parameters around a defined base scenario.

The base scenario for this analysis is a steady-state turn at a velocity of 10 m/s, a road friction coefficient μ of 0.3, and a turning radius R of 180 m. All longitudinal axle slips ($s_{x,1f}$, $s_{x,1r}$, $s_{x,2r}$) are assumed to be zero unless specified as the varying parameter. As the chosen vehicle configuration is inherently more susceptible to jackknifing, the stability limit is most often dictated by the disappearance or shrinking of the SOE for Unit 1.

In the following figures, the adaptive nature of the SOEs is visualized in 3D, where the x and y axes represent the phase plane $\omega_{z,1}$ vs β_1 for Unit 1, and $\omega_{z,2}$ vs β_2 for Unit 2, and the z-axis represents the parameter being varied.

3.7.1 Effect of Varying Road Friction μ

Road friction is an environmental factor that directly governs the maximum lateral force that the tires can generate. Figure 3.12 illustrates the SOE's sensitivity to μ as it is varied from 0.15 to 0.5.

As expected, the volume of the SOE for both units increases significantly with higher road friction. This is because a greater available grip allows the vehicle to tolerate larger deviations in sideslip angle and yaw rate, before instability occurs. The top-view plots show that the location of the stable equilibrium point (the black star) remains fixed, as the steady-state turning kinematics are independent of friction. However, the basin of attraction around this point expands considerably. For a low friction value of $\mu = 0.15$, the SOE for Unit 1 completely disappears, while a small SOE remains for Unit 2. This predicts that under these slippery conditions, the vehicle will become unstable via jackknifing.

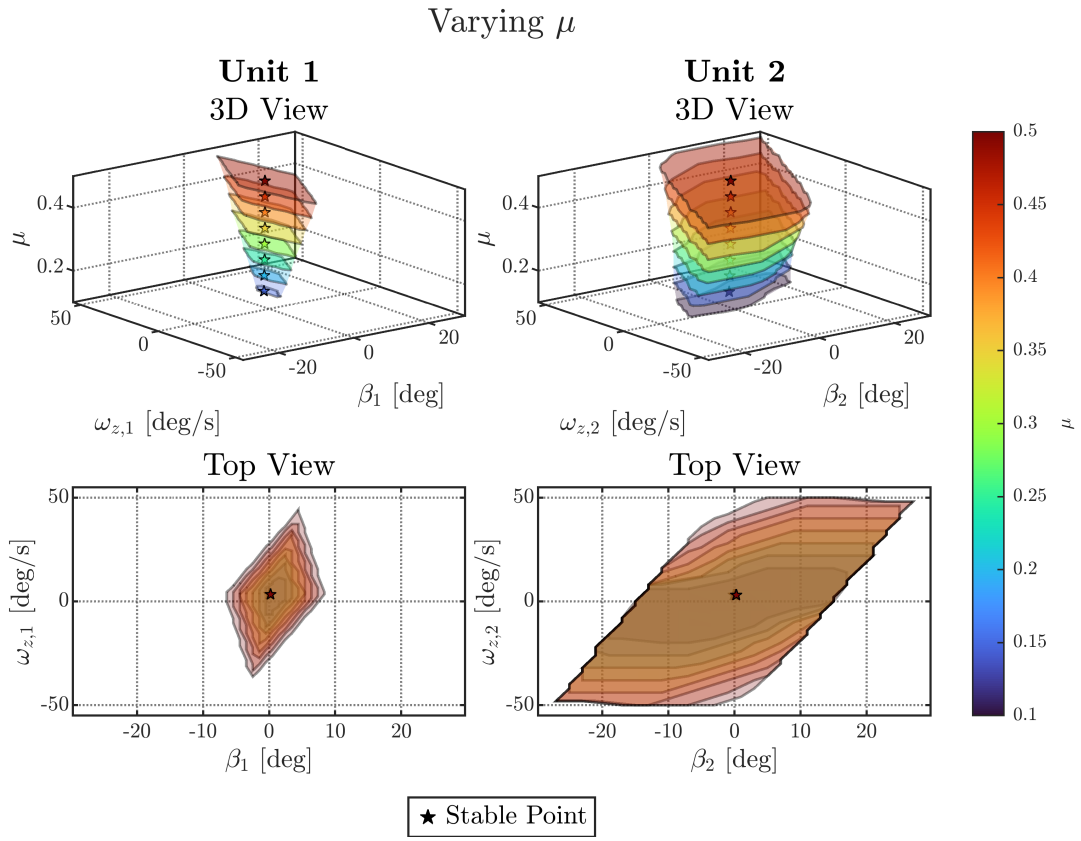

Figure 3.12: SOE for Unit 1 and Unit 2 with varying friction μ.

3.7.2 Effect of Varying Longitudinal Slip on Axle $1r$

Longitudinal forces from acceleration or braking consume a portion of the tire's available grip, reducing its lateral force capability, as explained by the tire friction ellipse. Figure 3.13 demonstrates this effect by varying the longitudinal slip on the truck's rear axle $s_{x,1r}$ from -0.10 (braking) to $+0.10$ (tractive).

The analysis reveals a strong coupling between the truck's longitudinal slip and its lateral stability. As the absolute value of $s_{x,1r}$ increases, the SOE for Unit 1 shrinks, indicating a reduced margin for stability. Since the slip on the trailer axle $s_{x,2r}$ is held at zero, the SOE for Unit 2 remains largely unchanged, isolating the failure mode to the tractor. An interesting observation is the asymmetry of the SOE. The stability boundary is not identical for positive and negative slips of the same magnitude. This can be attributed to the non-linearities of the tire model and the second-order effect where the braking slip ($s_{x,1r} < 0$) slightly reduces the vehicle's speed, which inherently enhances stability. The location of the stable E.P. also shifts with slip for Unit 1, reflecting the change in the steady-state equilibrium.

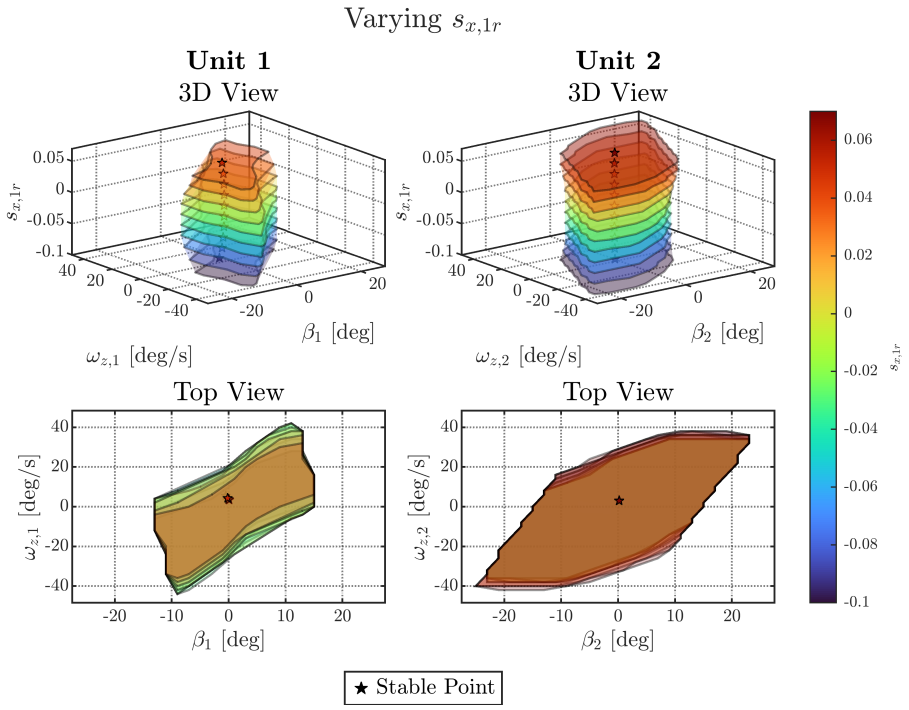

Figure 3.13: SOE for Unit 1 and Unit 2 with varying $s_{x,1r}$.

3.7.3 Effect of Varying Longitudinal Slip on Axle $2r$

Conversely, Figure 3.14 shows the effect of varying the longitudinal slip on the trailer's rear axle $s_{x,2r}$ while keeping all other slips at zero.

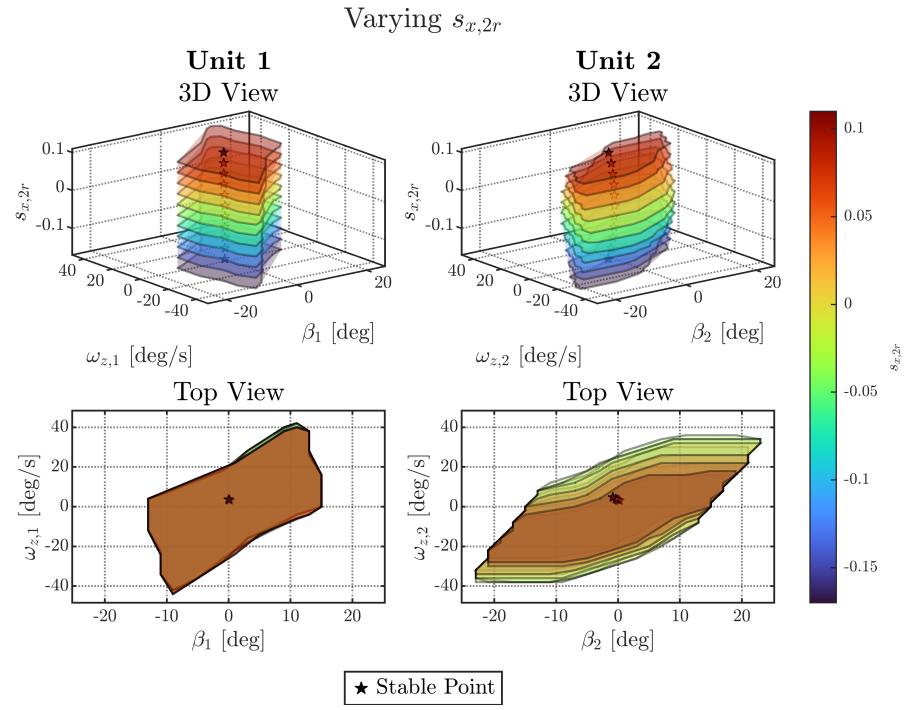

Figure 3.14: SOE for Unit 1 and Unit 2 with varying $s_{x,2r}$.

In this case, the stability of Unit 1 remains almost entirely unaffected, as its tires are operating with full lateral grip capacity. However, the SOE for Unit 2 is highly sensitive to $s_{x,2r}$. As the magnitude of the trailer's slip increases, its SOE shrinks drastically, predicting the onset of trailer swing. This analysis demonstrates the decoupled nature of these two failure modes, highlighting how instability can originate from either unit.

3.7.4 Effect of Varying Steering Angle δ_{1f}

The steering angle is the primary driver input for cornering manoeuvres. Figure 3.15 shows how the SOEs evolve as the steering angle is increased from 0° to 3°.

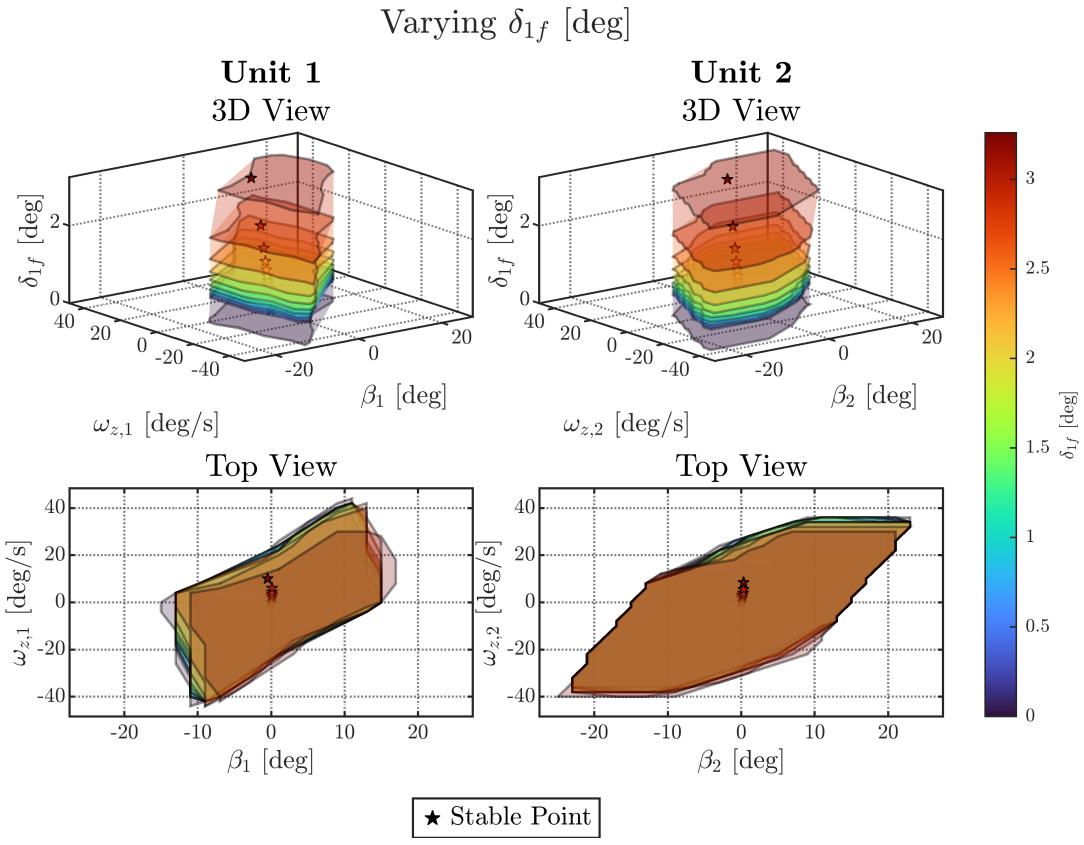

Figure 3.15: SOE for Unit 1 and Unit 2 with varying δ_{1f}.

As the steering input becomes more aggressive, the stable equilibrium point for both units shifts to higher yaw rates and sideslip angles, corresponding to a tighter turn. The size of the SOE around this stable point progressively shrinks. The stable E.P. moves closer to the unstable saddle point, reducing the system's robustness to disturbances. As our configuration is sensitive to jackknifing, the SOE for Unit 1 contracts more rapidly than that of Unit 2. Once the steering angle exceeds a critical value, the stable and unstable equilibria merge, leading to a bifurcation where the SOE disappears entirely.

3.7.5 Effect of Varying Velocity v_x

Vehicle velocity is a critical factor in stability, as lateral forces scale with the square of the velocity ($F_y \propto v_x^2$). Figure 3.16 illustrates this relationship by varying v_x from 5 m/s to 15 m/s.

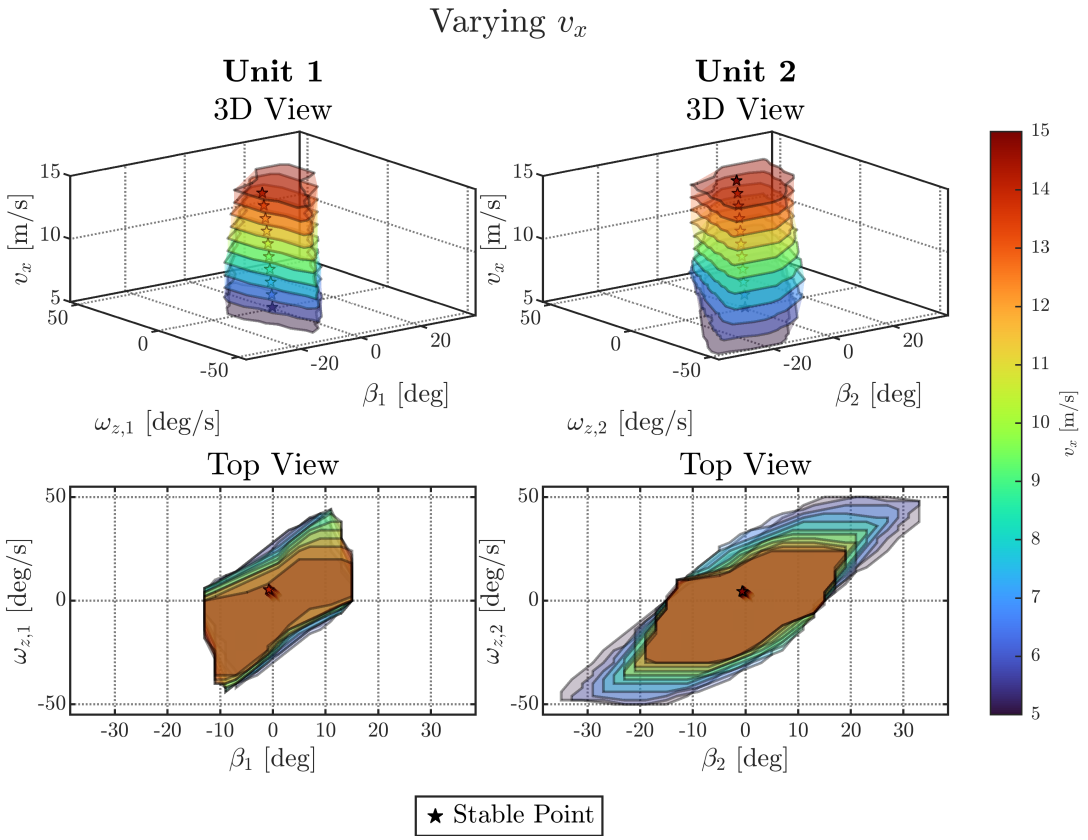

Figure 3.16: SOE for Unit 1 and Unit 2 with varying v_x.

The results clearly show that the SOEs for both units decrease in size as velocity increases. At higher speeds, the same radius turn demands significantly more lateral grip, leaving less margin for error. For this specific configuration, the SOE for Unit 1 disappears at approximately 15 m/s, predicting a high-speed jackknifing instability.

The parametric analysis presented in this section, particularly the demonstrated sensitivity of the SOEs to longitudinal slip (Figure 3.13 and Figure 3.14), provides the foundation for the control system design in the following chapter. They prove that by modulating axle slip, it is possible to actively manage and enlarge the vehicle's stability envelope in real-time.

4

Controller Design

The sensitivity analysis in the preceding chapter established a clear and quantifiable link between the vehicle's longitudinal axle slips s_x and the size of its SOE. It was demonstrated that by modulating longitudinal forces, it is possible to actively manage the vehicle's stability margin. This chapter leverages that fundamental insight to design, implement, and validate two distinct stability control strategies.

The first controller detailed is an offline, lookup-table-based controller that utilizes the precomputed SOEs to enforce real-time stability constraints. The second controller, presented subsequently, advances this concept by performing the stability calculations online, creating a fully adaptive system. Both controllers were implemented and tested with the high-fidelity VTM model-in-loop simulations in Simulink.

4.1 Controller with Pre-computed Longitudinal Slip Limits (Offline Mode)

The driver's inputs (accelerator and brake pedals) represent requests for longitudinal force. These requests are mapped to a commanded longitudinal wheel slip s_x^{req}, which serves as the control input to the vehicle control system. Within this formulation, constraints are applied to s_x^{req} to ensure the vehicle state remains within the safe operating envelope (SOE). The controllers introduced below adaptively bound s_x^{req} by a state-dependent reference s_x^{ref}, preventing instability while preserving the driver's intent as closely as possible.

4.1.1 Offline Database Generation

The foundation of this controller is a comprehensive, multi-dimensional database of SOEs generated offline using the methodology from Chapter 3. The SOEs are defined in the β vs ω_z phase plane for the two primary instability modes:

- **Jackknifing:** Analyzed in the tractor's (β_1 vs $\omega_{z,1}$) phase plane.
- **Trailer swing:** Analyzed in the trailer's (β_2 vs $\omega_{z,2}$) phase plane.

For each point in the multi-dimensional parameter space, defined by the tuple $(\mu,\ \delta_{1f},\ s_{x,1f},\ s_{x,1r},\ s_{x,2r},\ v_{x,i})$, a phase portrait is generated and the stability

of each point on the grid is evaluated. The boundary of the stable region is then stored as a set of valid points and converted into a polygon that approximates the SOE. This process yields two extensive databases of pre-computed stability boundaries: one for jackknifing, indexed by the states of Unit 1, and one for trailer swing, indexed by the states of Unit 2.

The offline generation of the SOE database is a computationally intensive process. Covering a wide range of parameters with fine granularity results in very large lookup tables, which may be challenging to store in automotive-grade memory. Another drawback of this approach is that the database is inherently discrete. If the vehicle's real-time state falls between grid points or outside the pre-computed range, the controller must rely on interpolation or conservative fallbacks, which may lead to suboptimal performance.

4.1.2 Controller Design

The controller operates by taking real-time information from the vehicle and outputting a constrained slip command.

4.1.2.1 Inputs (measured or estimated in realtime)

- **Vehicle States:** Longitudinal velocities ($v_{x,1}$, $v_{x,2}$), sideslip angles (β_1, β_2), and yaw rates ($\omega_{z,1}$, $\omega_{z,2}$) for both the tractor and the trailer.
- **Driver & Actuation States:** The current steering angle (δ_{1f}), and the longitudinal slips on the axles ($s_{x,1f}$, $s_{x,1r}$, $s_{x,2r}$).
- **Environmental Parameter:** The estimated road friction coefficient (μ).
- **Driver Request:** The requested longitudinal slip s_x^{req}.

4.1.2.2 Outputs

- **Safe Slip Limit:** The maximum permissible slip magnitude for axles under the current conditions, s_x^{max}.
- **Saturated Slip Command:** The final slip command sent to the actuator, s_x^{ref}, which is the driver's request saturated by the safe limit.

4.1.3 Control Algorithm

The controller's logic is executed at each time step and follows a systematic process to determine the safe slip limit.

1. **Analysis Mode:** The controller first determines which instability mode to guard against. To prevent jackknifing, it uses the Unit 1 database and the vehicle's current states ($v_{x,1}$, β_1, $\omega_{z,1}$) . To prevent trailer swing, it uses the Unit 2 database and the states ($v_{x,2}$, β_2, $\omega_{z,2}$).

2. **Query the Database:** The algorithm filters the multi-dimensional SOE database to find the entry that most closely matches the current operating condition. It applies tight tolerances to find matching entries for μ, δ_{1f}, and the non-controlled axle slips, and then selects the nearest available velocity slice $v_{x,i}$.
3. **Perform Safety Check:** For a candidate slip value s_x on the controlled axle, the controller retrieves the corresponding SOE polygon from the database. It then performs a point-in-polygon test to determine if the vehicle's current state (β_i, $\omega_{z,i}$) lies inside this SOE.
   (a) If (β_i, $\omega_{z,i}$) is inside the SOE, the candidate slip s_x is deemed `SAFE`.
   (b) If (β_i, $\omega_{z,i}$) is outside the SOE, the candidate slip s_x is `UNSAFE`.
   (c) If the current state falls outside the pre-computed range of the database, the result is `UNKNOWN`, and a conservative fallback is triggered.
4. **Search for Maximum Safe Slip:** To find the optimal limit, the controller sweeps through the pre-tabulated slip grid for the selected database entry, starting from the highest magnitude. The first slip value that returns a `SAFE` result from the safety check is designated as the maximum safe slip limit, s_x^{max}.
5. **Saturate the Driver's Request:** The final command s_x^{ref} is calculated by clipping the magnitude of the driver's request s_x^{req} to the safe limit s_x^{max}, while preserving the original sign (tractive or braking).

$$s_x \;=\; \mathrm{sign}\Big(s_x^{req}\Big) \;\cdot\; \min\big(\,|s_x^{req}|,\; |s_x^{max}|\,\big) \tag{4.1}$$

   Optionally, a small hysteresis band and rate limits can be added to prevent chattering near the boundary.

In some exceptional cases, where both jackknifing and trailer swing must be respected simultaneously, the limits are computed from both the modes and merged conservatively on magnitude.

$$|s_x^{max}| = \min\Big(|s_x^{max,\ jackknifing}|,\; |s_x^{max,\ trailerswing}|\Big) \tag{4.2}$$

4.1.4 Assumptions and Limitations

- **Heavy Offline Computation:** Generating multiple SOEs from the phase portraits over varying parameters is computationally expensive and leads to large databases.
- **Discretization:** If the current state falls between grid nodes or outside range, we get the result as `UNKNOWN`, prompting conservative fallbacks (e.g., zeroing slips). Interpolation across velocity slices and using tight tolerances can help but do not eliminate this issue.

- **Parameter Mismatch:** SOEs reflect offline parameter assumptions (such as load, friction, tire model, temperature, wear). Mismatch can make the controller over-conservative or occasionally over-permissive.
- **Geometric Approximation:** The Point-in-polygon test using `convhull` MATLAB function tends to over-approximate the non-convex safe regions (safer but potentially limits the performance). On the other hand, using `boundary` function in MATLAB overfits the data.

Due to these factors, the offline approach is often impractical in production. For this reason, a more scalable solution that relaxes dependence on these pre-computed dense databases and adapts to changing conditions is presented next in Section 4.3.

4.2 Validation Results

The performance of the offline adaptive slip controller was evaluated with open-loop manoeuvres using the high-fidelity VTM simulation environment. The model was driven by open-loop inputs for steering δ_{1f} and driver slip request $s_{x,1f}^{req}$, $s_{x,1r}^{req}$, $s_{x,2r}^{req}$, rather than by throttle and brake commands. The following test were conducted at a friction of $\mu = 0.3$.

4.2.1 Scenario 1: Step Steer with Braking Force on Axle $1r$

This scenario tests the controller's ability to manage stability during a combined cornering and braking manoeuvre. The vehicle is initialized at 18 m/s, and the driver applies a step steer with a braking slip request $s_{x,1r}^{req}$ of -0.10 on the truck's rear axle as shown in Figure 4.1.

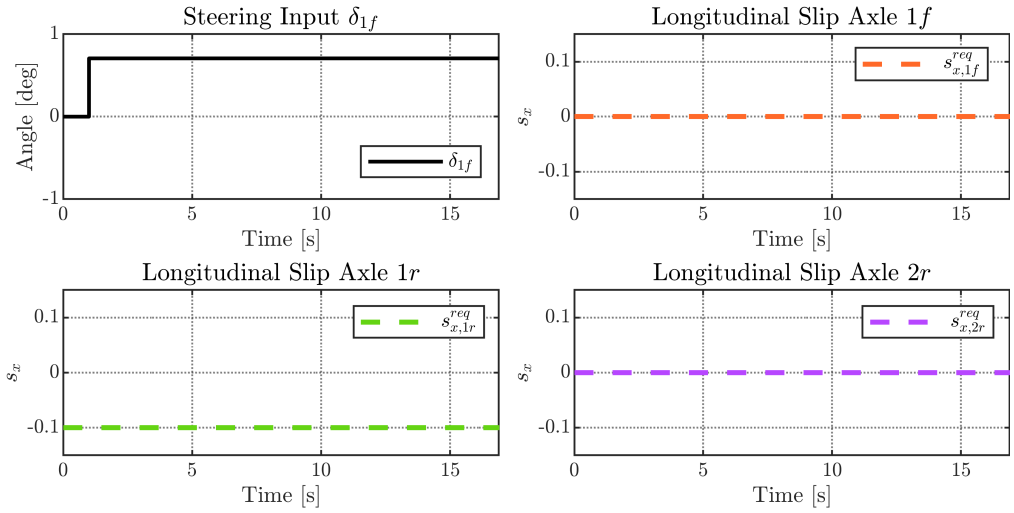

Figure 4.1: Scenario 1 - Open-loop inputs for step steer with driver braking slip request on axle $1r$.

4.2.1.1 Controller Disabled

Without an adaptive slip controller, the high initial speed and combined braking/ cornering forces lead to a loss of tractor stability, resulting in a severe jackknife, as shown in Figure 4.2.

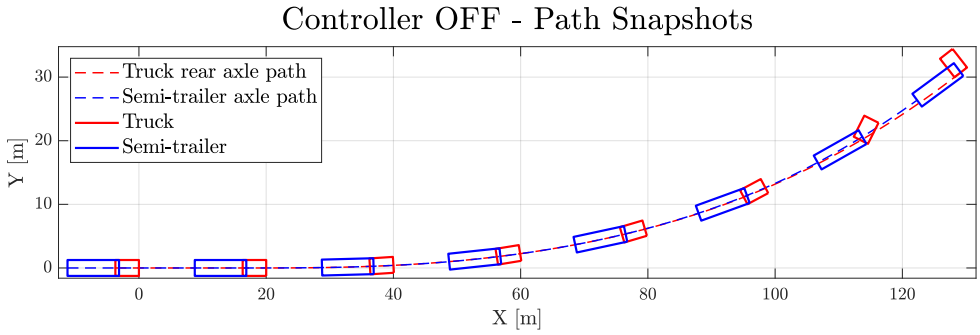

Figure 4.2: Scenario 1 - Path snapshots with controller disabled.

4.2.1.2 Controller Enabled

The controller (Figure 4.4) immediately identifies the driver's braking request as unsafe and calculates the maximum permissible braking slip that maintains stability. It modulates the braking force by increasing the permissible slip as the velocity decreases, which allows the vehicle to decelerate safely through the corner without losing control as shown in Figure 4.3.

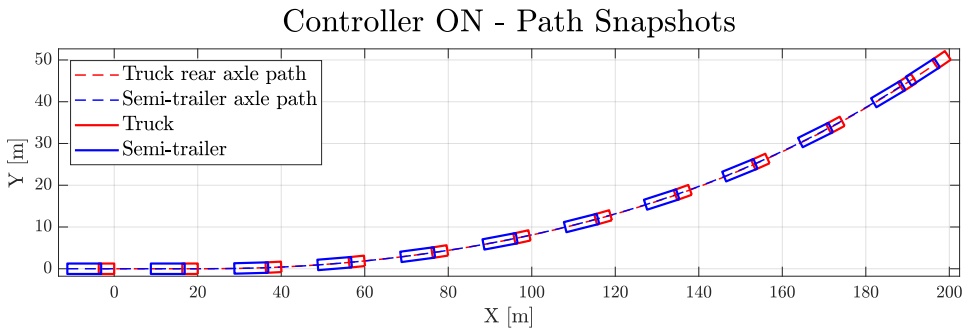

Figure 4.3: Scenario 1 - Path snapshots with controller enabled.

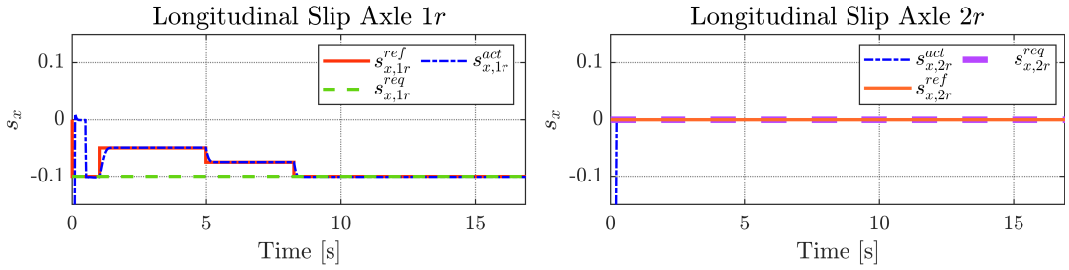

Figure 4.4: Scenario 1 - Adaptive longitudinal slip controller.

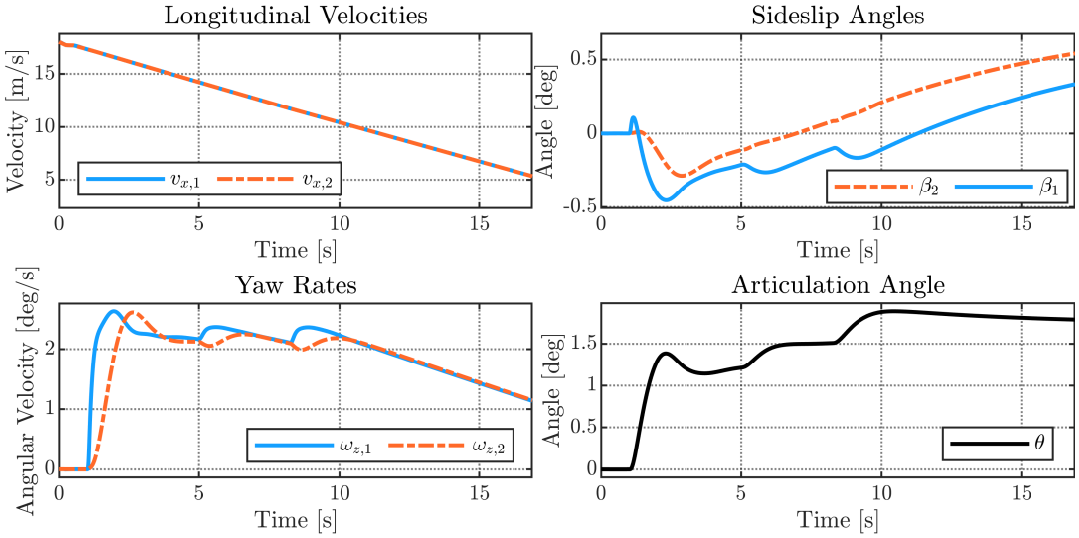

Figure 4.5: Scenario 1 - Vehicle states with controller enabled.

Figure 4.5 shows the evolution of the vehicle states during the manoeuvre. The controller keeps the reference slip within the pre-computed SOE boundary for any given timestep as expected.

4.2.2 Scenario 2: Step Steer with Tractive Force on Axle $1r$

This scenario tests the controller's ability to manage stability during a combined cornering and accelerating manoeuvre. The vehicle is initialized at 10.5 m/s, and the driver applies a step steer with a tractive slip request $s_{x,1r}^{req}$ of 0.25 on the truck's rear axle as shown in Figure 4.6.

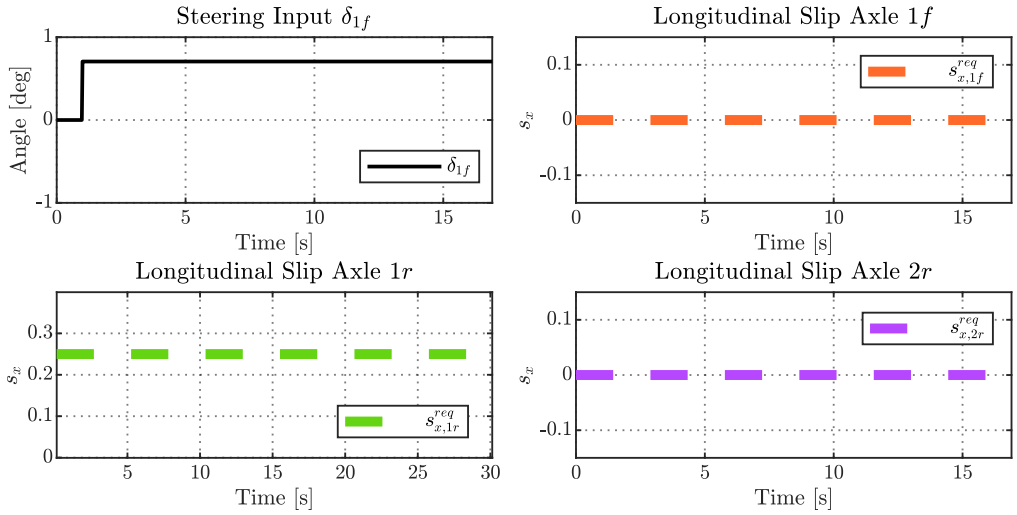

Figure 4.6: Scenario 2 - Open-loop inputs for step steer with driver tractive slip request on axle $1r$.

4.2.2.1 Controller Disabled

Without an adaptive slip controller, the tractor loses stability and progresses towards a jackknife, as shown in Figure 4.7.

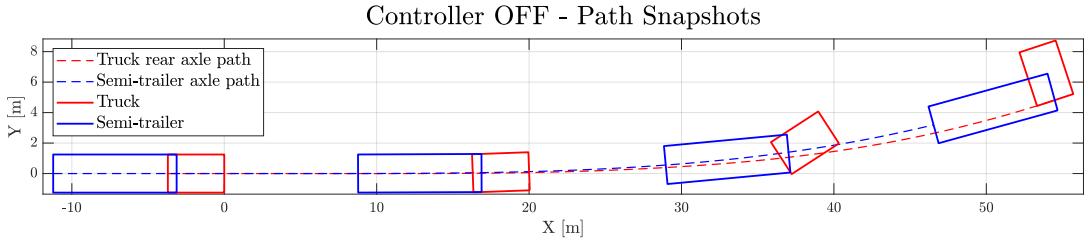

Figure 4.7: Scenario 2 - Path snapshots with controller disabled.

4.2.2.2 Controller Enabled

The controller (Figure 4.9) immediately identifies the driver's positive slip request as unsafe and calculates the maximum permissible tractive slip that maintains stability. It modulates the tractive force by reducing the permissible slip as the velocity increases, which allows the vehicle to accelerate safely through the corner without losing control as shown in Figure 4.8.

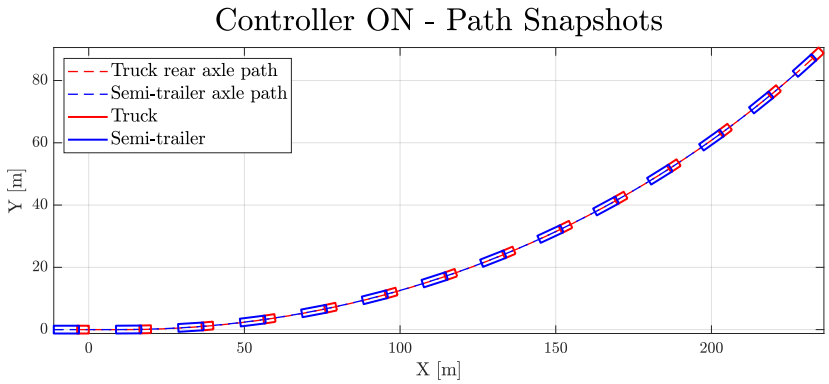

Figure 4.8: Scenario 2 - Path snapshots with controller enabled.

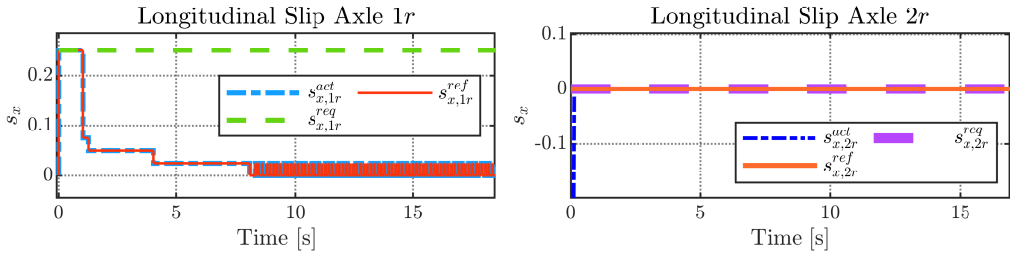

Figure 4.9: Scenario 2 - Adaptive longitudinal slip controller.

The chattering observed toward the end of the manoeuvre in Figure 4.9 originates from the discretization of the safe slip reference, which was computed with a grid resolution of approximately 0.025. This quantization effect causes small oscillations in the slip reference signal when the system operates near a switching boundary. Such chattering can be mitigated through techniques like hysteresis, rate limiting, or introducing a small dead-band, which can smoothen the controller action and yield a more continuous reference.

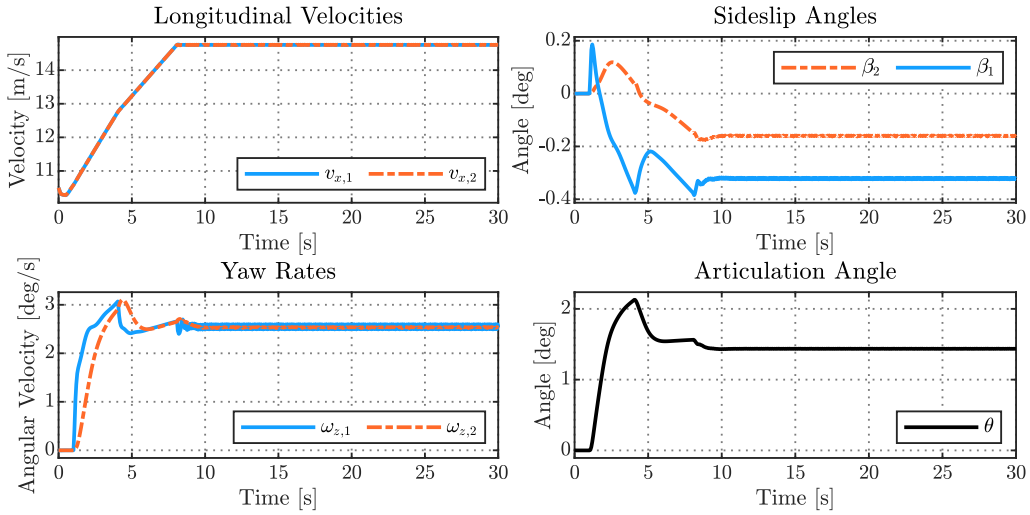

Figure 4.10: Scenario 2 - Vehicle states with controller enabled.

Figure 4.10 shows the evolution of the vehicle states during the manoeuvre. The controller keeps the reference slip within the pre-computed SOE boundary for any given timestep as expected.

The controller was also evaluated in open-loop step steering tests with tractive force applied on axle $2r$ (refer to Appendix A.5), and braking force applied on axle $2r$, where it successfully prevented instability.

4.3 Controller with Real-time Longitudinal Slip Limits (Online Mode)

Building upon the phase-plane analysis framework from Chapter 3, this chapter introduces a novel, online, adaptive longitudinal slip controller which was implemented in VTM (model-in-the-loop (MIL)) on Simulink. The fundamental departure from traditional methods is the move away from pre-computed SOEs. Instead of relying on offline analysis, this controller leverages the methodologies of Section 3.5 to determine the vehicle's stability limits in real-time at every simulation time step.

This online approach assumes the availability of accurate vehicle state and parameter estimations. Its objective is to maximize traction and braking performance by providing the highest possible longitudinal slip commands to the VTM's pre-built slip controllers without compromising vehicle stability. A key simplifying heuristic of the current implementation is its prioritization logic: if both vehicle units are unstable, the controller actively modulates the slip on one axle while commanding the other to a safe, zero slip state as stated in Section 1.4. While this approach is effective for maintaining stability, especially during propulsion by reducing the total propulsive force, it is a significant simplification. For braking, this single-axle modulation can be detrimental, as it reduces the total braking force and may lead to a slower reduction in velocity. Ideally, a more sophisticated control allocation strategy would simultaneously optimize the slips on multiple axles, particularly during braking, to maintain the desired total braking force while redistributing it to ensure stability. This would require an optimization-based approach to perform coordinated control in real-time.

The controller is implemented with a hierarchical architecture, which is detailed in the following sections. It is logically divided into three main components:

1. **The Main Controller:** A high-level state machine that assesses the overall vehicle stability and decides which control strategy to deploy.
2. **The Real-Time Stability Checker:** A function that encapsulates the stability analysis methods from Section 3.5 into a single, callable routine to provide a binary stable/unstable verdict for a given state.
3. **The Optimal Stable Slip Search:** A bisection search algorithm that efficiently finds the maximum permissible longitudinal slip command s_x^{ref} within the stable region of operation.

4.3.1 Main Controller

The main controller is the brain of the control system. At each time step, it follows a Assess-Decide-Act protocol. Its logic is implemented as a finite state machine that transitions between a passive state (passing through driver slip request commands) and several active intervention states based on real-time stability assessments. A complete pseudocode is found in Appendix A.1. The key phases of its operation are outlined as follows:

1. **Assessment Phase:** The controller takes the current vehicle state (velocities, sideslip angles, yaw rates) and the actual measured longitudinal slips at each axle as its inputs. It immediately calls the Real-Time Stability Checker to determine if the truck (Unit 1) and trailer (Unit 2) are stable in their current condition.
2. **Latch Evaluation Phase:** To prevent rapid oscillations between controlled and non-controlled states, the controller employs a latching mechanism. If the controller was active in the previous time step (i.e., a latch is active), it checks if the driver's original, unaltered slip request would now result in a stable condition. If so, all latches are released, and control is returned to the driver. This ensures that the intervention persists until the vehicle has returned to a safe operating region.
3. **Decision Phase:** Based on the current stability and the state of the latches, the orchestrator transitions to the appropriate control state.
   (a) If both units are stable and no latches are active, it remains in a `PASS_THROUGH` state.
   (b) If only one unit is unstable, it enters a `CONTROL_U1` or `CONTROL_U2` state.
   (c) If both units are unstable, it performs an emergency check for stability at zero axle slip for both Unit 1 and Unit 2. If even this condition is unstable, it enters a `FAULT_UNRECOVERABLE` state. In this scenario, the stability cannot be maintained solely by modulating slips. Intervention steps must be taken by the driver or another control system, such as in cases of extremely high steering input.
   (d) Otherwise, it prioritizes intervention based on the unit with the higher absolute slip magnitude, entering a `CONTROL_BOTH_PRIO_U1` or `CONTROL_BOTH_PRIO_U2` state. This heuristic is designed to address the more critical instability first.
4. **Action Phase:** The orchestrator executes the actions associated with its decided state. This typically involves calling the Optimal Stable Slip Search algorithm to calculate the new reference slip for the unstable unit(s). In prioritized cases, the non-priority unit's reference slip is commanded to be zero which is the highest probable safe value, while the search is performed for the prioritized unit.

4.3.2 The Real-Time Stability Checker

The stability checker is a direct, online implementation of the analysis techniques developed in Section 3.5. It answers the question: "For a given set of inputs and the current vehicle state, is this unit stable?" Stability is confirmed only if the following three criteria are met.

Function: `CHECK_STABILITY(unit_to_check, current_vehicle_state, current_slips)`

Returns: `TRUE` or `FALSE`
The algorithm's logic is as follows:

1. **Existence of a Stable Equilibrium:** As described in Section 3.5.1, the function first solves the nonlinear system to find all equilibrium points for the specified unit. The system only passes this criterion if at least one stable equilibrium point is found. If no such point exists, the system has no stable steady-state condition to converge to, and the function immediately returns `FALSE`.
2. **State within Physical Tire Slip Limits:** The controller then verifies that the vehicle's current state resides within the practical operating limits of the tires, as detailed in Section 3.5.2. Using Equations (3.11), (3.12) and (3.13), it calculates the boundaries on the phase plane that correspond to peak tire sideslip. If the vehicle's current state lies outside this region, the tires are considered saturated and unable to provide effective control. The function returns `FALSE`.
3. **Trajectory Convergence:** Finally, instead of using the computationally intensive LLE method (Section 3.5.3.1) as in the offline analysis, the online controller uses the direct forward integration method from Section 3.5.3.2. Starting from the vehicle's current state, the system's ODEs are integrated forward for a short, finite time period. The final state of this simulated trajectory is compared to the location of the stable equilibrium point found in the first criterion. If the Euclidean distance is below a predefined convergence tolerance, the trajectory is confirmed to be in the basin of attraction. Only if this final criterion is met does the function return `TRUE`.

4.3.3 The Optimal Stable Slip Search Algorithm

Once the controller determines that intervention is required, it must calculate a new, safe reference slip. To find the optimal command, the controller employs a bisection search algorithm which efficiently locates the slip magnitude that is closest to the driver's request while remaining within the stability boundary.

Function: `FIND_STABLE_SLIP(unit_to_search, driver_request, check_other_unit)`

Returns: `stable_sx` s_x^{ref}

The algorithm's logic is as follows:

1. **Initialization:** The search interval is defined with a lower bound of zero and an upper bound of the absolute value of the driver's requested slip, $|s_x^{req}|$.
2. **Sanity Check:** The algorithm first calls the `CHECK_STABILITY` function for the condition where the slip of the searched axle is zero. If this is not stable, no solution is possible, and the search terminates, returning zero slip.
3. **Iterative Search:** The algorithm iteratively bisects the search interval. At each step, it tests the stability of the midpoint slip value, s_x^{mid}.
   (a) If the midpoint is stable, it becomes the new best-known stable slip, and the search interval is narrowed to $[s_x^{mid},\ s_x^{req}]$ to search for a solution with a higher magnitude.
   (b) If the midpoint is unstable, the solution must lie closer to zero, and the search interval is narrowed to $[0,\ s_x^{mid}]$.
4. **Coupled Stability Check:** In scenarios where both units are unstable (e.g., `CONTROL_BOTH_PRIO_U1`), the `check_other_unit` flag is set to `TRUE`. In this mode, every stability check performed during the search for the priority unit also verifies the stability of the non-priority unit (which has its slip commanded to zero). This ensures that the chosen slip command is stable for the entire vehicle system, not just one part of it.
5. **Termination:** After a small, fixed number of iterations (5 iterations with a search resolution of 0.02), the search converges on the highest magnitude slip that was found to be stable, providing a command that maximizes traction performance while maintaining stability.

4.3.4 Controller Design and Implementation Limitations

While the online controller demonstrates a significant advancement in adaptive stability control, its current implementation is subject to several key assumptions and limitations that frame the scope of this work.

The most significant assumption is the availability of perfect state and parameter information. The controller's real-time stability calculations rely on accurate measurement or estimate of all vehicle states, driver inputs, and critical parameters such as the road friction coefficient.

Furthermore, while the controller logic has been proven to operate effectively in an MIL simulation, its real-time feasibility on production automotive hardware has not yet been validated. The current implementation runs successfully on a modern high-performance laptop at a $20Hz$ control frequency, but this is alongside the computationally intensive VTM simulation. Future work must include profiling the execution time of all logical paths within the controller to ensure that it meets the real-time constraints of an automotive Electronic Control Unit (ECU).

4.4 Validation Results

The performance of the online adaptive slip controller was evaluated in a series of challenging open-loop manoeuvres using the high-fidelity VTM simulation environment (MIL). The model was driven by open-loop inputs for steering δ_{1f} and driver slip request $s^{req}_{x,1f}$, $s^{req}_{x,1r}$, $s^{req}_{x,2r}$ instead of throttle and brake commands. The following tests were conducted at a friction of $\mu = 0.3$.

4.4.1 Scenario 1 – Step Steer with Tractive Force on axle $1r$

This scenario is designed to induce jackknifing. The vehicle is initialized at 8 m/s, and at $t = 0.1$ s, the driver applies a sharp step steering input while simultaneously requesting a constant tractive slip of 0.1 on the truck's rear axle $s^{req}_{x,1r}$ as seen in Figure 4.11.

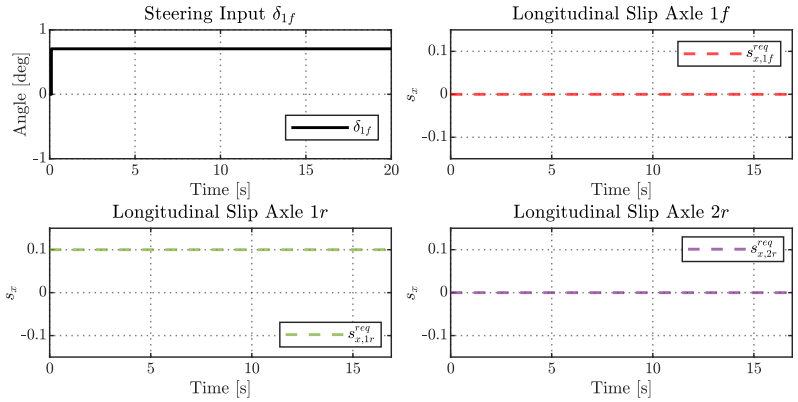

Figure 4.11: Scenario 1 - Open-loop inputs for step steer with driver tractive slip request on axle $1r$.

4.4.1.1 Controller Disabled

Without intervention, the combination of aggressive steering and high tractive demand on the tractor's rear axle quickly overwhelms the available tire grip. As shown in Figure 4.12, the tractor loses lateral stability and spins out, resulting in a jackknifing failure.

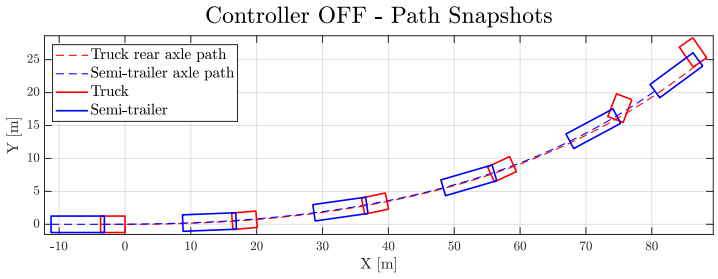

Figure 4.12: Scenario 1 - Path snapshots with controller disabled, showing a jackknifing instability.

4.4.1.2 Controller Enabled

With the adaptive controller enabled, the vehicle remains stable throughout the manoeuvre. As seen in Figure 4.13, the controller successfully guides the vehicle through the turn without any loss of control.

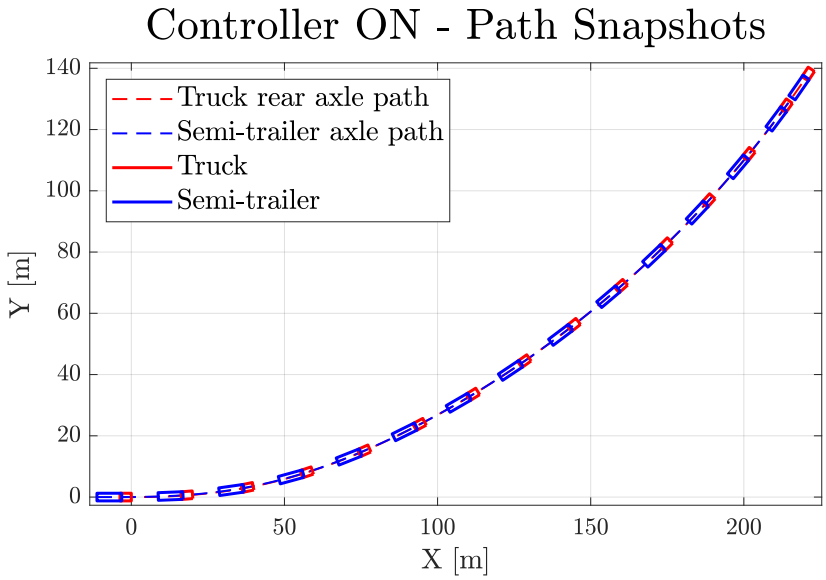

Figure 4.13: Scenario 1 - Path snapshots with controller enabled.

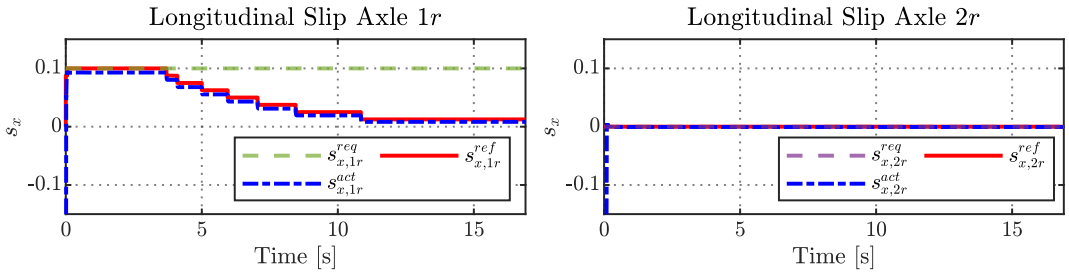

Figure 4.14: Scenario 1 - Adaptive longitudinal slip controller.

The controller's intervention is detailed in Figure 4.14. The driver's requested slip $s_{x,1r}^{req}$ of 0.1 is immediately identified as unstable. The controller calculates and applies a safer reference slip $s_{x,1r}^{ref}$, which the low-level actuator tracks $s_{x,1r}^{act}$. As the vehicle accelerates as shown in Figure 4.15, the lateral forces increase, and the stability margin shrinks. The controller adapts by progressively reducing the slip limit, effectively trading longitudinal force for the required lateral grip to maintain stability. The reference-slip signal is updated at 20 Hz (as noted previously). The vehicle states in Figure 4.15 confirm a stable outcome, with the yaw rates and articulation angle converging to a steady state as the reference slip $s_{x,1r}^{ref}$ becomes 0.

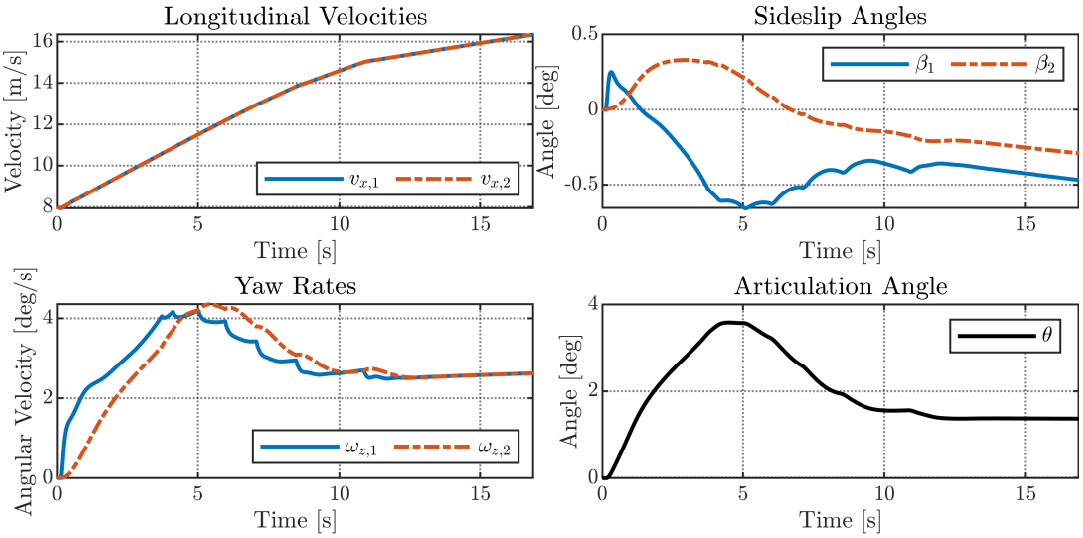

Figure 4.15: Scenario 1 - Vehicle states with controller enabled.

4.4.2 Scenario 2 – Step Steer with Tractive Force on axle $2r$

This test is designed to create a trailer swing instability. The vehicle starts at a higher initial speed of 12 m/s, and the driver applies a step steer while requesting a tractive slip of 0.1 on the trailer's rear axle $s_{x,2r}^{req}$ as shown in Figure 4.16.

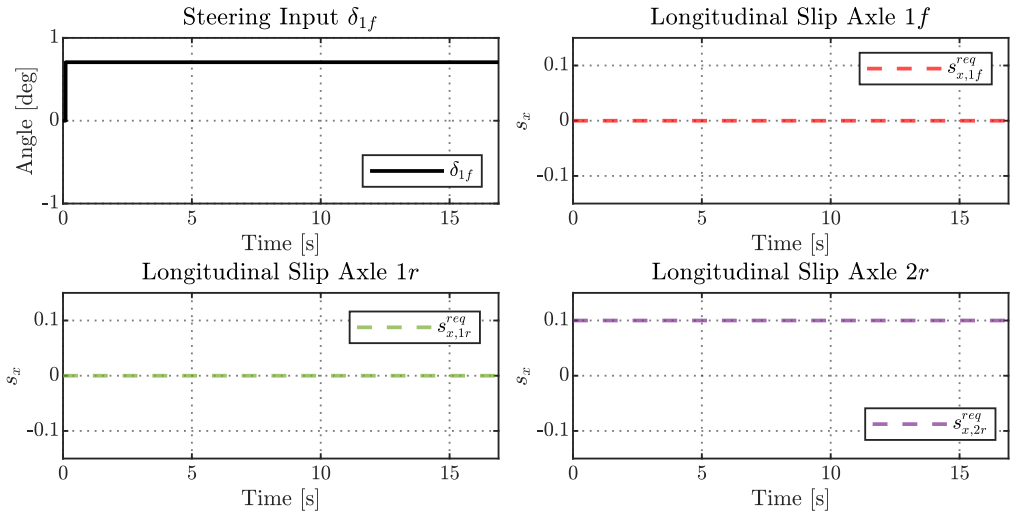

Figure 4.16: Scenario 2 - Open-loop inputs for step steer with driver tractive slip request on axle $2r$.

4.4.2.1 Controller Disabled

The high traction demand on the trailer's axle saturates its lateral grip, causing it to lose traction. Figure 4.17 shows the result: a combination spin-out where the trailer swings wide, destabilizing the entire vehicle and leading to a loss of control.

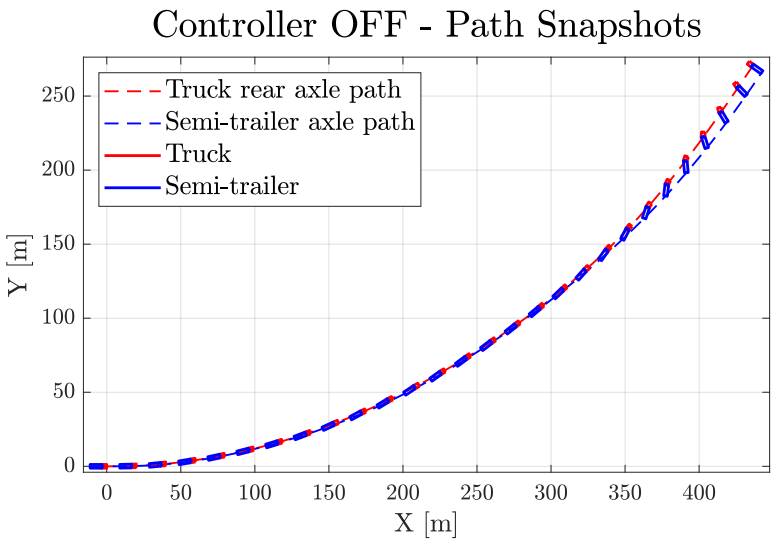

Figure 4.17: Scenario 2 - Path snapshots with controller disabled.

4.4.2.2 Controller Enabled

The controller again successfully prevents the instability as shown in the path snapshots in Figure 4.18. The intervention plot in Figure 4.19 shows that at $t = 6.5\ s$, the controller detects that the requested slip of 0.1 on the trailer axle would cause instability. It immediately intervenes, commanding the trailer axle slip to zero, which leads to a safe state. This action preserves the trailer's lateral stability, allowing the vehicle to complete the turn safely.

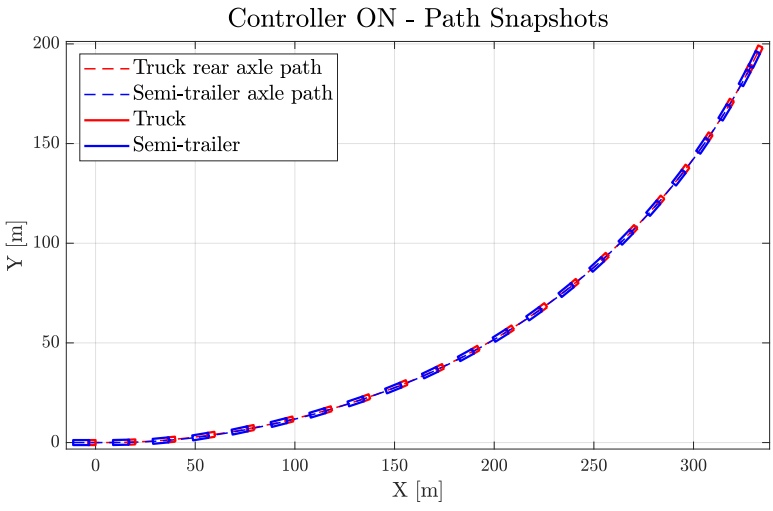

Figure 4.18: Scenario 2 - Path snapshots with controller enabled.

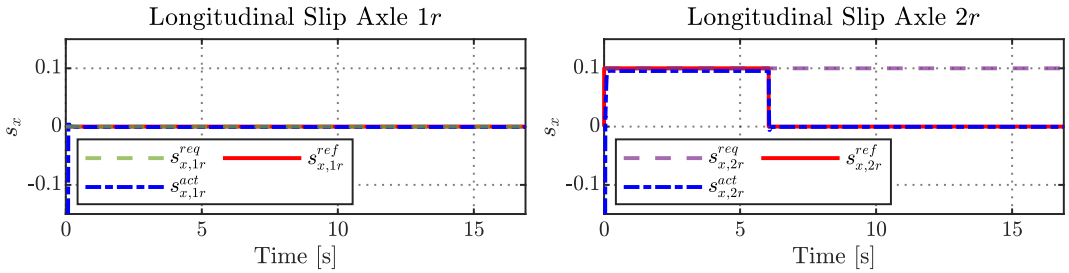

Figure 4.19: Scenario 2 - Adaptive longitudinal slip controller.

4.4.3 Scenario 3 – Step Steer with Braking Force on axle $1r$

This scenario tests the controller's ability to manage stability during a combined cornering and braking manoeuvre. The vehicle is initialized at 18 m/s, and the driver applies a step steer with a braking slip request $s^{req}_{x,1r}$ of -0.12 on the truck's rear axle as shown in Figure 4.20.

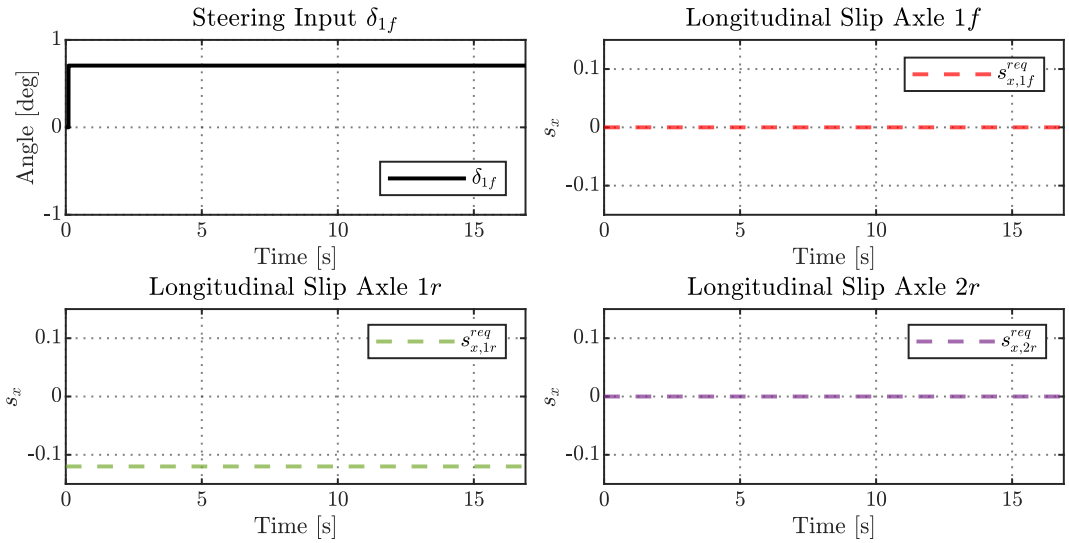

Figure 4.20: Scenario 3 - Open-loop inputs for step steer with driver braking slip request on axle $1r$.

4.4.3.1 Controller Disabled

The high initial speed and combined braking/cornering forces lead to a loss of tractor stability, resulting in a severe jackknife, as shown in Figure 4.21.

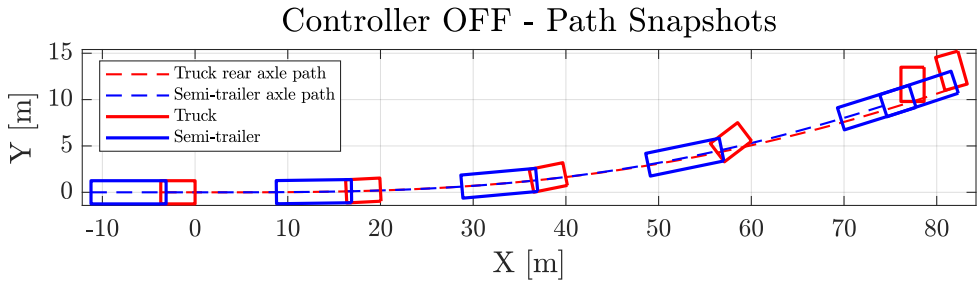

Figure 4.21: Scenario 3 - Path snapshots with controller disabled.

4.4.3.2 Controller Enabled

The controller (Figure 4.23) immediately identifies the driver's braking request as unsafe and calculates the maximum permissible braking slip that maintains stability. It modulates the braking force, allowing the vehicle to decelerate safely through the corner without losing control, as shown in Figure 4.22.

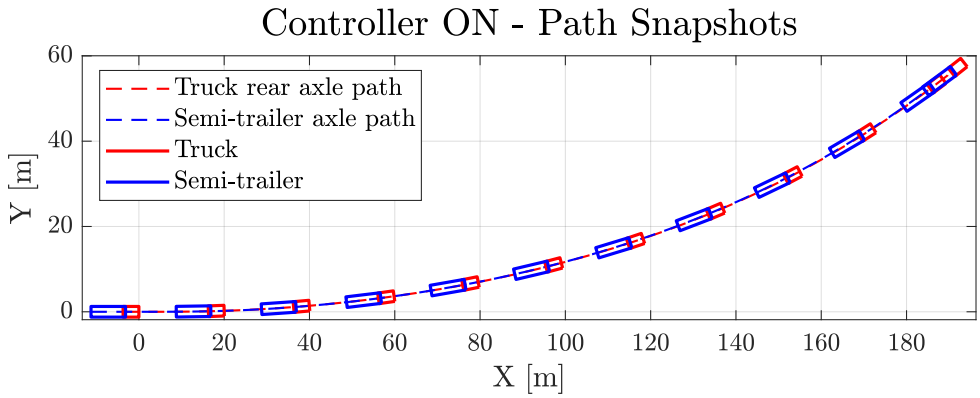

Figure 4.22: Scenario 3 - Path snapshots with controller enabled.

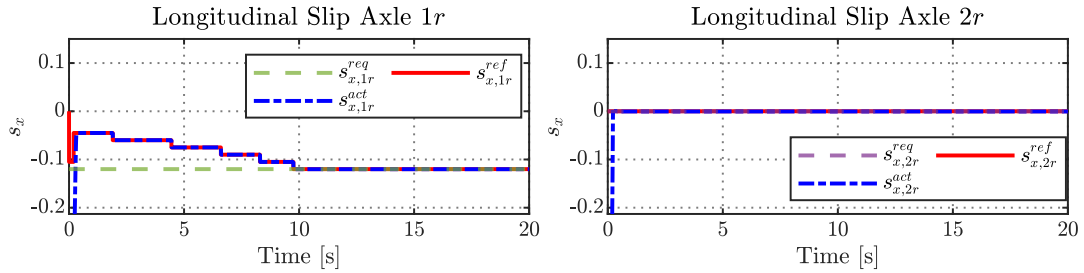

Figure 4.23: Scenario 3 - Adaptive longitudinal slip controller.

4.4.4 Scenario 4 – Sine Steer with Tractive Force on axle $1r$

This scenario evaluates the controller's performance during a dynamic, transient manoeuvre. The vehicle accelerates from 2 m/s with a constant tractive slip request of 0.1 on the tractor's rear axle, while the driver applies a continuous sine wave steering input as shown in Figure 4.24.

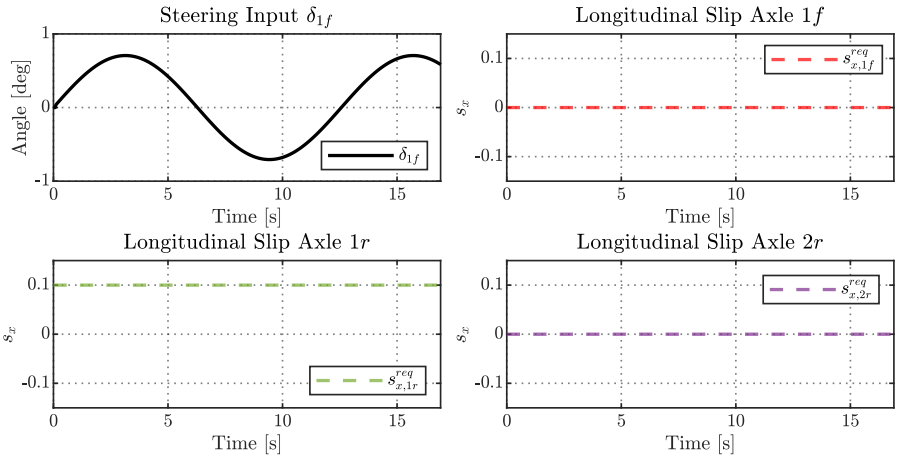

Figure 4.24: Scenario 4 - Open-loop inputs for sine steer with driver tractive slip request on axle $1r$.

4.4.4.1 Controller Disabled

As the vehicle's speed increases, the lateral accelerations induced by the sine steering become too large for the tires to handle, especially with the high tractive demand. The vehicle states in Figure 4.25 show this clearly: at around $t = 15$ s, the tractor sideslip angle β_1 and yaw rate $\omega_{z,1}$ diverge uncontrollably. The path plot in Figure 4.26 confirms a complete loss of control.

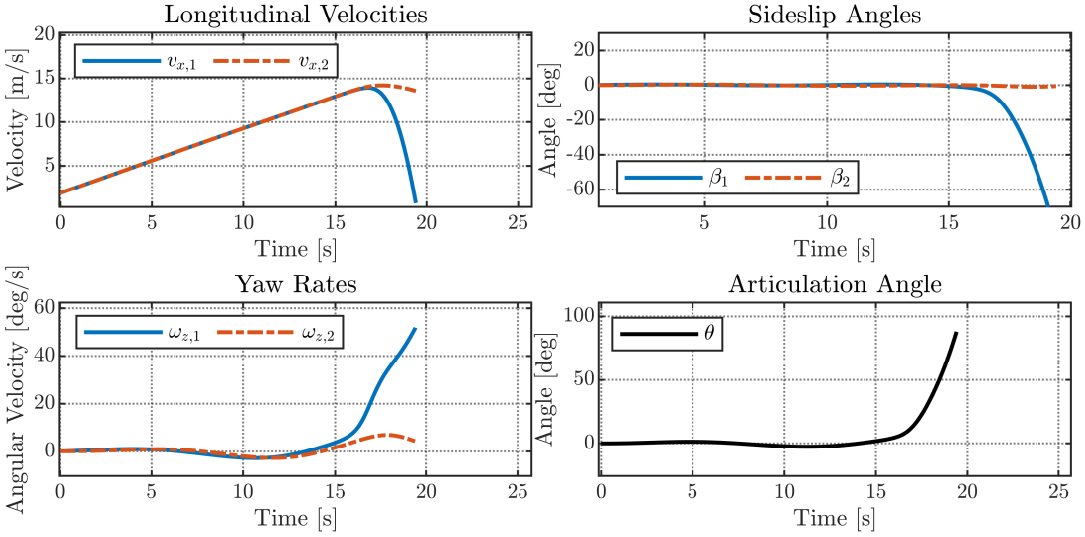

Figure 4.25: Scenario 4 - Vehicle states with controller disabled.

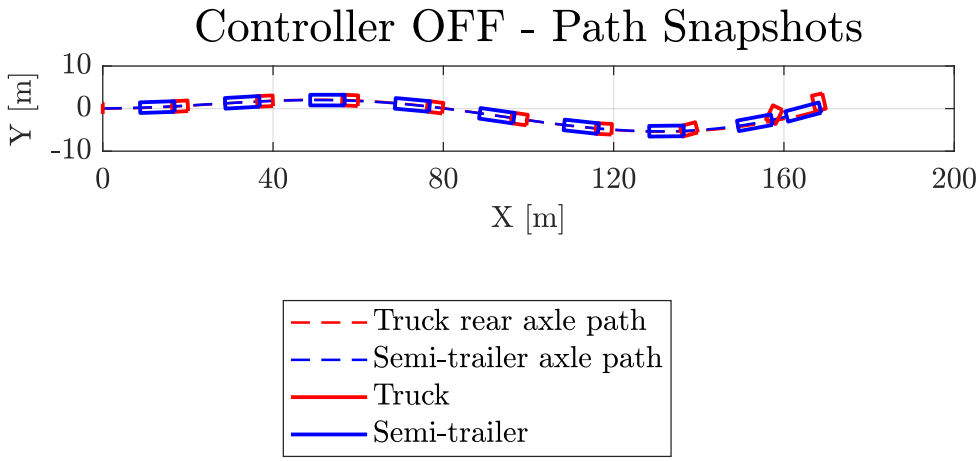

Figure 4.26: Scenario 4 - Path snapshots with controller disabled.

4.4.4.2 Controller Enabled

The controller remains active throughout the manoeuvre, as shown in Figure 4.27. It continuously adjusts the reference slip on the tractor's rear axle, reducing it during the peaks of the sine wave where lateral demand is highest and allowing more slip during the straight sections. This modulation always keeps the vehicle within its stability envelope. The vehicle states in Figure 4.29 remain bounded and oscillatory, following the steering input, and the vehicle successfully tracks the desired path as shown in Figure 4.28.

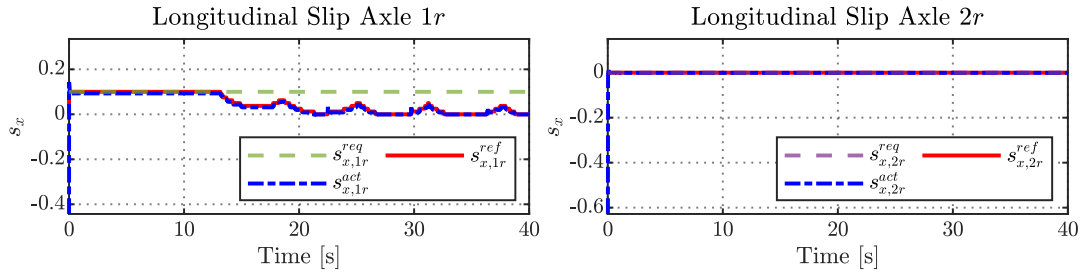

Figure 4.27: Scenario 4 - Adaptive longitudinal slip controller.

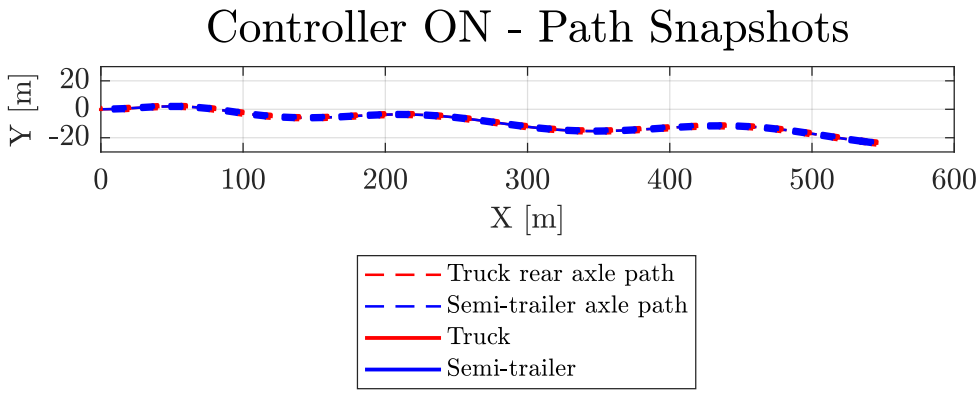

Figure 4.28: Scenario 4 - Path snapshots with controller enabled.

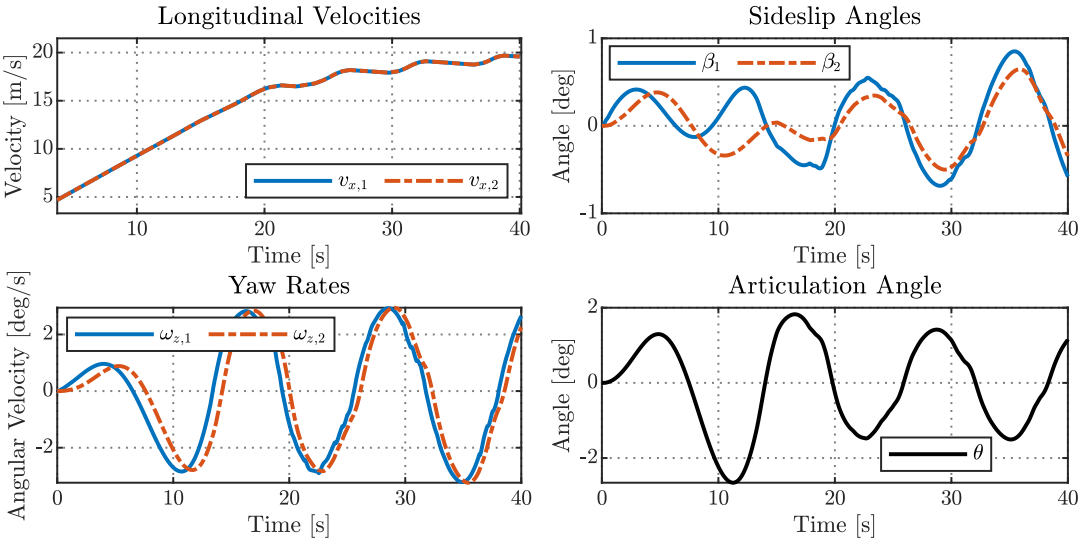

Figure 4.29: Scenario 4 - Vehicle states with controller enabled.

5
Conclusion

This thesis set out to address a critical challenge in heavy vehicle safety: the inherent lateral instability of AHVs. Conventional stability control systems often rely on fixed-slip thresholds, which may utilize higher slip limits than the proven safe limits under certain conditions, such as dynamic maneuvers involving high lateral accelerations. The primary aim of this work was, therefore, to develop a framework for generating and utilizing adaptive, state-dependent SOEs to enhance lateral stability, moving beyond the limitations of traditional approaches. This was achieved by systematically addressing three core research questions regarding the application of phase portrait analysis to the AHV dynamics, the automated determination of stability boundaries, and the practical implementation of these principles in an advanced control system.

5.1 Summary of Contributions

The research presented has made several key contributions to the field of vehicle dynamics and control.

First, a computationally efficient, non-linear single-track model of a truck-semitrailer combination was developed. Its accuracy was validated against the high-fidelity VTM simulation environment, confirming its suitability for the required analysis. This model served as the foundation for the entire stability analysis, balancing physical fidelity with the computational speed necessary for thousands of simulation runs.

The main contribution of this work is the successful application of phase portrait analysis to the complex, high-dimensional dynamics of an AHV. We demonstrated that by decoupling the system into two-dimensional phase planes for the tractor ($\omega_{z,1}$ vs β_1) and the trailer ($\omega_{z,2}$ vs β_2), the stability analysis becomes tractable and visually intuitive. A robust and automated pipeline was created to synthesize the SOEs by combining equilibrium point analysis, the imposition of physical tire slip limits, and global stability classification using LLEs. This methodology provides a clear, quantitative, and physics-based visualization of the vehicle's true stability boundaries. The subsequent parametric analysis revealed the high sensitivity of these SOEs to key variables such as road friction, velocity, steering angle, and most importantly, longitudinal axle slip, confirming that slip modulation is a viable mechanism for stability control.

Finally, the practical utility of this framework was demonstrated through the design and implementation of a controller with pre-computed SOE data and a novel online adaptive slip controller. Unlike offline approaches that would rely on pre-computed lookup tables, this controller leverages the core stability analysis methods to determine the safe operating limits in real-time at each simulation step. The controller's hierarchical architecture, featuring a real-time stability checker and an optimal stable slip search algorithm, proved to be highly effective. When tested in a series of challenging maneuvers within the VTM environment, the controller successfully prevented both jackknifing and trailer swing instabilities, validating the core hypothesis of this thesis. It consistently maintained vehicle control while maximizing longitudinal force, allowing the vehicle to operate safely at the very edge of its dynamic limits.

5.2 Discussion

The findings of this thesis represent a significant step forward from static, worst-case safety systems to dynamic, state-aware control. By defining stability not as a fixed threshold but as an adaptive envelope, the proposed framework allows for a more intelligent allocation of tire forces. This enables the maximization of vehicle performance without compromising safety. The ability to calculate these limits in real-time bridges the gap between theoretical stability analysis and practical, on-vehicle implementation, presenting a clear pathway for the next generation of active safety systems. This approach provides a deeper, more fundamental understanding of the vehicle's stability landscape, which can inform the development of more robust and less intrusive advanced driver-assistance systems (ADAS) and autonomous driving (AD) control strategies for heavy vehicles.

5.3 Future Work

While this thesis successfully establishes and validates the proposed framework, several promising avenues for future research remain.

- **Real-Time Implementation and Validation:** The most critical next step is to evaluate the computational performance of the online controller on an automotive-grade Electronic Control Unit (ECU) in a Hardware-in-the-Loop (HIL) setup, followed by validation in a physical test vehicle. This would confirm its real-world feasibility and robustness.
- **Integration with State and Parameter Estimation:** The current controller assumes the availability of accurate state and parameter information. Future work should focus on integrating the control logic with robust estimation algorithms to handle the uncertainties and sensor noise inherent in real-world driving, particularly for critical parameters like the road friction coefficient.

- **Expansion of Scope:** The methodology could be extended to analyze more complex vehicle configurations, such as B-doubles, and to address other critical instability modes that were outside the scope of this thesis, including rollover and oscillatory trailer sway.
- **Coordinated Multi-Axle Control:** The current controller prioritizes control on a single axle when both units are unstable. A more advanced implementation could utilize optimization-based control allocation strategies to simultaneously coordinate the slip on all axles, potentially yielding superior performance.
- **Predictive Control Strategies:** The controller is currently reactive to the vehicle's present state. Integrating the SOE framework with predictive control techniques, such as Model Predictive Control (MPC), would enable the system to anticipate future instabilities and take proactive measures, further enhancing safety.

Bibliography

[1] E. Commission, "European Road Safety Observatory, Facts and Figures Buses/coaches/heavy goods vehicles - 2020" [Online]. Available at: https://road-safety.transport.ec.europa.eu/system/files/2021-07/facts_figures_buses_and_hgv_final_20210323.pdf

[2] Erdinc, U., Jonasson, M., Sadeghi Kati, M., Jacobson, B., Fredriksson, J., & Laine, L. (2023). Safe operating envelope based on a single-track model for yaw instability avoidance of articulated heavy vehicles. *Vehicle System Dynamics, 62*(8), 2138–2161. Available at: https://doi.org/10.1080/00423114.2023.2276767.

[3] Laine, L. (2007). Reconfigurable motion control systems for over-actuated road vehicles. *Chalmers Tekniska Hogskola (Sweden)*. Available at: http://dx.doi.org/10.13140/RG.2.2.23751.32166

[4] Bobier-Tiu, C. G., Beal, C. E., Kegelman, J. C., Hindiyeh, R. Y., & Gerdes, J. C. (2018). Vehicle control synthesis using phase portraits of planar dynamics. *Vehicle System Dynamics, 57*(9), 1318–1337. Available at: https://doi.org/10.1080/00423114.2018.1502456.

[5] Farroni, F., Russo, M., Russo, R., Terzo, M., & Timpone, F. (2013). A combined use of phase plane and handling diagram method to study the influence of tyre and vehicle characteristics on stability. *Vehicle System Dynamics, 51*(8), 1265–1285. Available at: https://doi.org/10.1080/00423114.2013.797590

[6] Kumar, A., Verma, S., & Dheer, D. (2024). Bifurcation Analysis of a Non-Linear Vehicle Model Under Wet Surface Road Condition. *International Journal of Robotics and Control Systems, 4*(2), 727-745. Available at: https://pubs2.ascee.org/index.php/IJRCS/article/view/1346

[7] Sun, T., & He, Y. (2015). Phase-Plane Analysis for Evaluating the Lateral Stability of Articulated Vehicles. *SAE Technical Paper* 2015-01-1574. Available at: https://doi.org/10.4271/2015-01-1574.

[8] Mantaras, D.A., Luque, P., & Alonso, M. (2022). Phase plane analysis applied to non-explicit multibody vehicle models. *Multibody Syst Dyn 56*, 173–188.

Available at: https://doi.org/10.1007/s11044-022-09846-9

[9] Sadri, S., & Wu, C. (2013). Stability analysis of a nonlinear vehicle model in plane motion using the concept of Lyapunov exponents. *Vehicle System Dynamics, 51*(6), 906–924. Available at: https://doi.org/10.1080/00423114.2013.771785

[10] Meng, F., Shi, S., Zhang, B., Bai, M., & Lin, N. (2022). Analysis for global characteristics of Lyapunov exponents in vehicle plane motion system. *Sci Rep 12*, 9300. Available at: https://doi.org/10.1038/s41598-022-13411-x

[11] Vignati, M., & Sabbioni, E. (2021). A cooperative control strategy for yaw rate and sideslip angle control combining torque vectoring with rear wheel steering. *Vehicle System Dynamics, 60*(5), 1668–1701. Available at: https://doi.org/10.1080/00423114.2020.1869273

[12] Erdinc, U. (2024). Safe distributed control allocation for articulated heavy vehicles. *Chalmers Tekniska Hogskola (Sweden)*. Available at: https://research.chalmers.se/publication/540674/file/540674_Fulltext.pdf

[13] Erdinc, U., Jonasson, M., Kati, M.S., Laine, L., Jacobson, B., & Fredriksson, J. (2024). Yaw Stability Control of Vehicles Using a Slip Polytope Validated with Real Tests. (eds) *16th International Symposium on Advanced Vehicle Control*. AVEC 2024. Available at: https://doi.org/10.1007/978-3-031-70392-8_19.

[14] Fröjd, N. (2021). Handling analysis and control development of commercial trucks with Volvo Transport Models. Presented at: *MATLAB EXPO 2021*. Available at: https://se.mathworks.com/videos/handling-analysis-and-control-development-of-commercial-trucks-with-volvo-transport-models-1622035211192.html.

[15] Jacobson, B.J.H. (2020). Vehicle Dynamics Compendium. *Chalmers University of Technology, Gothenburg (Sweden)*. Available at: https://research.chalmers.se/publication/520229/file/520229_Fulltext.pdf.

[16] Pacejka, H. B. (2005). Tire and vehicle dynamics. Elsevier. Available at: https://books.google.com/books?hl=en&lr=&id=JCHDuED3WIkC&oi=fnd&pg=PP1&ots=cHe-81osMl&sig=Z1EkWAZEAs7-paclmzsJO4MP0sk.

[17] Beal, C. E., Bobier, C. G., & Gerdes, J.C. (2011). Controlling Vehicle Instability Through Stable Handling Envelopes. *ASME 2011 Dynamic Systems and Control Conference, Volume 2*, pp. 861-868. Available at: https://doi.org/10.1115/DSCC2011-6124.

A

Appendix

A.1 Algorithm - Main Controller

This algorithm serves as the primary entry point and state machine for the controller. It assesses the vehicle's stability at each time step, determines the appropriate control mode, and commands the reference slips for the longitudinal slip controllers.

Algorithm – Main Controller

Inputs:

Vehicle parameters estimate
Tire model parameter estimates
Driver steering input (δ_{1f})
Driver requested longitudinal slips ($s_{x,1f}^{req}$, $s_{x,1r}^{req}$, $s_{x,2r}^{req}$)
Vehicle state variables ($v_{x,1}$, β_1, $\omega_{z,1}$, $v_{x,2}$, β_2, $\omega_{z,2}$, θ)

Outputs:

currentState
Calculated reference slips for the longitudinal slip controllers ($s_{x,1r}^{ref}$, $s_{x,2r}^{ref}$)
warning_flag → Boolean for critical fault conditions when longitudinal slip control cannot prevent instability - mostly due to high steering input.

Persistent Variables:

Booleans that hold the control state of the controller for Unit 1 and 2 between cycle (latch_U1_active, latch_U2_active)

Begin
Phase 1: Initialization
Set default outputs and assume no intervention is needed.
The controller will override these defaults if instability is detected.
Define Control States:
No intervention [pass_through ← 0]
Control Unit 1 only [control_U1 ← 1]
Control Unit 2 only [control_U2 ← 2]

Algorithm – Main Controller (continued)

```
    Control both prioritize Unit 1 [control_both_prio_U1 ← 3.1]
    Control both prioritize Unit 2 [control_both_prio_U2 ← 3.2]
    Unstable even at s^ref_x,1f, s^ref_x,1r, s^ref_x,2r = 0 [unrecoverable ← -1]
    Set Default Outputs:
    Initially, pass the driver's request through for axle 1r [s^ref_x,1r ← s^req_x,1r]
    Initially, pass the driver's request through for axle 2r [s^ref_x,2r ← s^req_x,2r]
    currentState ← pass_through

Phase 2: Stability Assessment
Evaluate the vehicle's current condition to see if control
is necessary or if a previously engaged control can be released.
    Check stability at current state:
    Is Unit 1 stable at current actual longitudinal slip?
        is_stable_U1_act ← check_stability (Unit1, s^act_x,1f, s^act_x,1r, s^act_x,2r)
    Is Unit 2 stable at actual longitudinal slip ?
        is_stable_U2_act ← check_stability(Unit2, s^act_x,1f, s^act_x,1r, s^act_x,2r)
    Evaluate Latch Release Condition:
    If the controller is already active (latched),
    check if it is safe to return control to the driver.
        if latch_U1_active or latch_U2_active Then
            Is vehicle stable with drivers requested slip
            (s^req_x,1f, s^req_x,1r, s^req_x,2r)?
            is_driver_req_stable ← check_stability(Unit=1 and Unit=2,
            s^req_x,1f, s^req_x,1r, s^req_x,2r)
            if is_driver_req_stable is true for both units Then
                The driver's request is now deemed safe, allowing for
                the release of the controller.
                    latch_U1_active ← false
                    latch_U2_active ← false
            End If
        End If

Phase 3: State Determination (Decision Logic)
Based on the assessment, decide on the appropriate control state for
this time step. This is the core decision-making part of the state
machine.
    Identify Which Units Need Control:
        U1_needs_control ← Not is_stable_U1_act or latch_U1_active
        U2_needs_control ← Not is_stable_U2_act or latch_U2_active
    Select the Control State:
        if U1_needs_control and Not U2_needs_control Then
            currentState ← control_U1
        Else if U2_needs_control and Not U1_needs_control Then
            currentState ← control_U2
```

Algorithm – Main Controller (continued)

```
        Else if U1_needs_control and U2_needs_control Then
        Both units are unstable. An unrecoverable condition must be
        checked before prioritizing.
            is_zero_slip_stable ← CHECK_STABILITY (Unit=1 and Unit=2
            with zero slips)
            if is_zero_slip_stable is false Then
                currentState ← unrecoverable
            else
            It is recoverable. Prioritise based on which axle has a
            higher slip magnitude.
                if |s^act_{x,1r}| ≥ |s^act_{x,2r}| Then
                    currentState ← control_both_prio_U1
                else
                    currentState ← control_both_prio_U2
                End If
            End If
        End If
```

Phase 4: Action Execution $s^{ref}_{x,1f}$ $s^{ref}_{x,1r}$ $s^{ref}_{x,2r}$

```
Execute the control action corresponding to the chosen state.
    Switch on currentState:
        Case pass_through:
        Do nothing. The default pass-through values are used.
        Case control_U1:
            stable_sx, success ← FIND_STABLE_SLIP (Unit=1,
            check_other_unit=false)
            if success Then s^ref_{x,1r} ← stable_sx else s^ref_{x,1r} ← 0
        Case control_U2:
            stable_sx, success ← FIND_STABLE_SLIP (Unit=2,
            check_other_unit=false)
            if success Then s^ref_{x,2r} ← stable_sx else s^ref_{x,2r} ← 0
        Case control_both_prior_U1:
        Strategy: Stabilise the tractor while forcing the trailer
        to a safe zero-slip state.
            s^ref_{x,2r} ← 0
            stable_sx, success ← FIND_STABLE_SLIP (Unit=1,
            check_other_unit=true)
            if success Then s^ref_{x,1r} ← stable_sx else s^ref_{x,1r} ← 0
        Case control_both_prior_U2:
        Strategy: Stabilise the trailer while forcing the tractor
        to a safe zero-slip state.
            s^ref_{x,1r} ← 0
            stable_sx, success ← FIND_STABLE_SLIP (Unit=2,
            check_other_unit=true)
```

Algorithm – Main Controller (continued)

```
            if success Then s^ref_{x,2r} ← stable_sx else s^ref_{x,2r} ← 0
        Case unrecoverable:
        Strategy: Maximum intervention. Command zero slip to
        both axles and alert the system.
            s^ref_{x,1r} ← 0
            s^ref_{x,2r} ← 0
            warning_flag ← 0
```

Phase 5: State Update for Next Cycle

```
Set the latches for the next iteration based on whether control was
active in this cycle.
    latch_U1_active ← true if any control state involving Unit 1 was
    active
    latch_U2_active ← true if any control state involving Unit 2 was
    active
```

Return: $s^{ref}_{x,1r}$, $s^{ref}_{x,2r}$, **warning_flag, currentState**

A.2 Algorithm - Check Unit Stability

This function determines if a given vehicle unit (truck or trailer) is stable for a given set of inputs and its current state. Stability is evaluated using a three criteria phase-plane analysis.

Input:
Unit to check $i \in \{1, 2\}$;
Vehicle parameters and tire model estimates;
Vehicle states ($v_{x,1}$, β_1, $\omega_{z,1}$, $v_{x,2}$, β_2, $\omega_{z,2}$, θ);
Inputs to check (δ_{1f}, $s_{x,1f}^{check}$, $s_{x,1r}^{check}$, $s_{x,2r}^{check}$);
Friction (μ)

Output: `is_stable` $\in \{$`false`, `true`$\}$

Step 1: Find Stable Equilibria (as explained in 3.5.1)
if *there is no stable equilibrium* **then**
 ∟ **return** `false`

Step 2: Verify Tire Slip Limits (as explained in 3.5.2);
if *current vehicle state* (β_i, $\omega_{z,i}$) *lies outside the tire slip limit bounds* **then**
 ∟ **return** `false`

Step 3: Verify Trajectory Convergence (as explained in 3.5.3.2);
if *current vehicle state* (β_i, $\omega_{z,i}$) *converges to stable equilibrium* **then**
 ∟ **return** `true`
else
 ∟ **return** `false`

A.3 Algorithm - Tractor Slip Control

Input: Driver requests: $s_{x,1r}$, $s_{x,2r}$
Output: Adjusted commands: $\hat{s}_{x,1r}$, $\hat{s}_{x,2r}$

Initialize:

$\hat{s}_{x,1r} \leftarrow s_{x,1r}$
$\hat{s}_{x,2r} \leftarrow s_{x,2r}$

Stability Check:

$unstable_{(truck)} \leftarrow \neg$`CheckStability(`*truck*`)`
▷ Check if any stable equilibrium exists for the current vehicle state and input set

Controller Logic:

if $unstable_{(truck)}$ **then**
  $\hat{s}_{x,2r} \leftarrow 0$
  $\hat{s}_{x,1r} \leftarrow$ `FindStableSlip(`*truck*, $\hat{s}_{x,2r}$`)`
    ▷ Find the Stable Slip Limit ($s_{x,1r}$) for the current vehicle state and input set

Return $\hat{s}_{x,1r}$, $\hat{s}_{x,2r}$

A.4 Algorithm - Vehicle Stability Control

Input: Driver requests: $s_{x,1r}$, $s_{x,2r}$
Output: Adjusted commands: $\hat{s}_{x,1r}$, $\hat{s}_{x,2r}$
Initialize:
$\hat{s}_{x,1r} \leftarrow s_{x,1r}$
$\hat{s}_{x,2r} \leftarrow s_{x,2r}$

Stability Check:
$unstable_{(truck)} \leftarrow \neg$`CheckStability(`*truck*`)`
$unstable_{(trailer)} \leftarrow \neg$`CheckStability(`*trailer*`)`

Controller Logic:
if $unstable_{(truck)}$ ***and*** $unstable_{(trailer)}$ **then**
  if $|s_{x,1r}| \geq |s_{x,2r}|$ **then**
    $\hat{s}_{x,2r} \leftarrow 0$
    $\hat{s}_{x,1r} \leftarrow$ `FindStableSlip(`*truck, 0, both=true*`)`
  else
    $\hat{s}_{x,1r} \leftarrow 0$
    $\hat{s}_{x,2r} \leftarrow$ `FindStableSlip(`*trailer, 0, both=true*`)`
else if $unstable_{(truck)}$ **then**
  $\hat{s}_{x,1r} \leftarrow$ `FindStableSlip(`*truck,* $s_{x,2r}$*, both=false*`)`
  if *still unstable* **then**
    $\hat{s}_{x,1r} \leftarrow 0$
    $\hat{s}_{x,2r} \leftarrow$ `FindStableSlip(`*trailer, 0, both=true*`)`
else if $unstable_{(trailer)}$ **then**
  $\hat{s}_{x,2r} \leftarrow$ `FindStableSlip(`*trailer,* $s_{x,1r}$*, both=false*`)`
  if *still unstable* **then**
    $\hat{s}_{x,2r} \leftarrow 0$
    $\hat{s}_{x,1r} \leftarrow$ `FindStableSlip(`*truck, 0, both=true*`)`

Return $\hat{s}_{x,1r}$, $\hat{s}_{x,2r}$

A.5 Additional Results - Offline Mode

A.5.1 Step Steer with Tractive Force on Axle $2r$

A.5.1.1 Controller Disabled

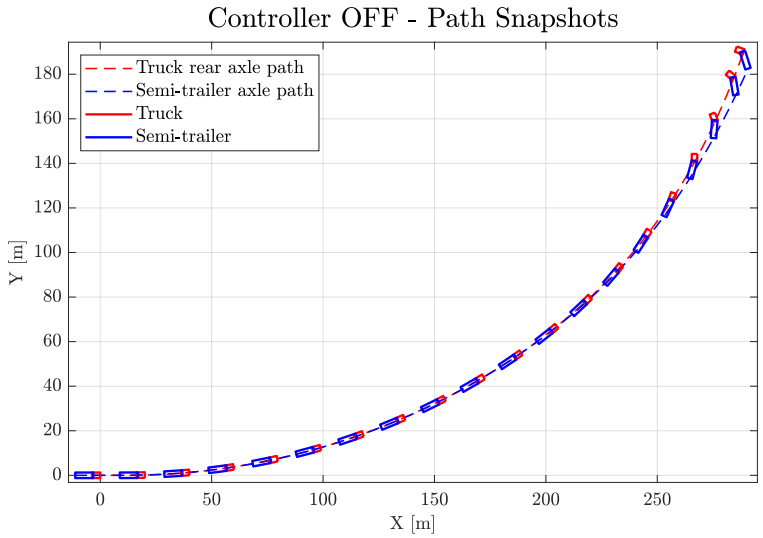

Figure A.1: Path snapshots with controller disabled.

A.5.1.2 Controller Enabled

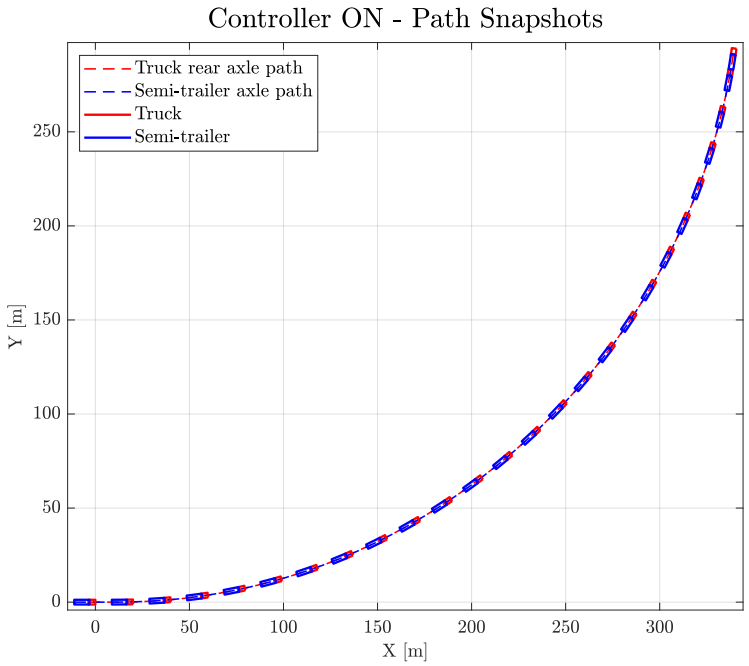

Figure A.2: Path snapshots with controller enabled.

DEPARTMENT OF MECHANICS AND MARITIME SCIENCES
CHALMERS UNIVERSITY OF TECHNOLOGY
Gothenburg, Sweden 2025
www.chalmers.se

CHALMERS
UNIVERSITY OF TECHNOLOGY